JOURNAL OF GEOPHYSICAL RESEARCH: ATMOSPHERES, VOL. 118, 9296–9315, doi:10.1002/jgrd.50712, 2013

Enhanced Deep Blue aerosol retrieval algorithm: The second generation

N. C. Hsu,[1] M.-J. Jeong,[2] C. Bettenhausen,[1,3] A. M. Sayer,[1,4] R. Hansell,[1,5] C. S. Seftor,[1,3] J. Huang,[5,6] and S.-C. Tsay[1]

Received 17 April 2013; revised 3 July 2013; accepted 2 August 2013; published 30 August 2013.

[1] The aerosol products retrieved using the Moderate Resolution Imaging Spectroradiometer (MODIS) collection 5.1 Deep Blue algorithm have provided useful information about aerosol properties over bright-reflecting land surfaces, such as desert, semiarid, and urban regions. However, many components of the C5.1 retrieval algorithm needed to be improved; for example, the use of a static surface database to estimate surface reflectances. This is particularly important over regions of mixed vegetated and nonvegetated surfaces, which may undergo strong seasonal changes in land cover. In order to address this issue, we develop a hybrid approach, which takes advantage of the combination of precalculated surface reflectance database and normalized difference vegetation index in determining the surface reflectance for aerosol retrievals. As a result, the spatial coverage of aerosol data generated by the enhanced Deep Blue algorithm has been extended from the arid and semiarid regions to the entire land areas. In this paper, the changes made in the enhanced Deep Blue algorithm regarding the surface reflectance estimation, aerosol model selection, and cloud screening schemes for producing the MODIS collection 6 aerosol products are discussed. A similar approach has also been applied to the algorithm that generates the Sea-viewing Wide Field-of-view Sensor (SeaWiFS) Deep Blue products. Based upon our preliminary results of comparing the enhanced Deep Blue aerosol products with the Aerosol Robotic Network (AERONET) measurements, the expected error of the Deep Blue aerosol optical thickness (AOT) is estimated to be better than $0.05 + 20\%$. Using 10 AERONET sites with long-term time series, 79% of the best quality Deep Blue AOT values are found to fall within this expected error.

Citation: Hsu, N. C., M.-J. Jeong, C. Bettenhausen, A. M. Sayer, R. Hansell, C. S. Seftor, J. Huang, and S.-C. Tsay (2013), Enhanced Deep Blue aerosol retrieval algorithm: The second generation, *J. Geophys. Res. Atmos.*, *118*, 9296–9315, doi:10.1002/jgrd.50712.

1. Introduction

[2] The impact of natural and anthropogenic sources of air pollution has gained increasing attention from scientific communities in recent years. Indeed, tropospheric aerosols not only perturb the radiative energy balance by interacting with solar and terrestrial radiation but also by changing cloud properties and lifetime. The Intergovernmental Panel on Climate Change (IPCC) estimated that the global-mean direct forcing due to anthropogenic aerosols is -0.5 ± 0.4 Wm^{-2} [*IPCC*, 2007], of smaller magnitude and opposite sign to the forcing exerted by greenhouse gasses. These results suggest that the aerosol cooling effect may have partially counteracted the warming contributed by greenhouse gas increases over the past few decades. Aerosol indirect and semidirect radiative effects are known with significantly larger uncertainty [*Lohmann and Feitcheer*, 2005; *Stevens and Feingold*, 2009], although in recent years, attempts have been made to assess their strengths with model simulations and satellite data [e.g., *Bauer and Menon*, 2012; *Wilcox*, 2012]. In addition to radiative effects on climate, knowledge of the atmospheric aerosol burden is of interest for topics including effects on air quality and human health [*Pope*, 2000], mineral transportation and fertilization of distant ecosystems [*Meskhidze et al.*, 2005], and effects on solar power yield [*Breikreutz et al.*, 2009], among others.

[3] The retrieval of aerosol properties from satellite measurements with sufficient accuracy for use in climate studies is a highly challenging task; it is an ill-posed problem where there are more unknowns about the microphysical and optical properties of aerosols than the information content that can be measured by current satellite sensors [e.g., *Hasekamp*

[1]NASA Goddard Space Flight Center, Greenbelt, Maryland, USA.
[2]Gangneung-Wonju National University, Gangneung City, South Korea.
[3]Science Systems and Applications, Inc, Lanham, Maryland, USA.
[4]Goddard Earth Sciences Technology and Research, Universities Space Research Association, Greenbelt, Maryland, USA.
[5]Earth System Science Interdisciplinary Center, UMD, College Park, Maryland, USA.
[6]NOAA NESDIS Center for Satellite Applications and Research, College Park, Maryland, USA.

Corresponding author: N. C. Hsu, NASA Goddard Space Flight Center, Greenbelt, MD 20771, USA. (Christina.Hsu@nasa.gov)

2169-897X/13/10.1002/jgrd.50712

and Landgraf, 2007; *Knobelspiesse et al*., 2012]. For single-view satellite sensors such as the Advanced Very High Resolution Radiometer (AVHRR), Sea-viewing Wide Field-of-view Sensor (SeaWiFS), Moderate Resolution Imaging Spectrometer (MODIS), and Visible Infrared Imaging Radiometer Suite (VIIRS), the most important factors/components that could substantially impact the performance of aerosol retrievals involve the following: (1) surface reflectance determination, including both their spectral and angular dependencies, (2) aerosol microphysical and optical model selection, (3) cloud screening, and (4) identification of snow/ice-covered surfaces, particularly over seasons where melting occurs. Adequate representation of aerosol microphysical and optical properties becomes an increasingly important factor in determining the accuracy of aerosol retrievals as the aerosol loading increases [*Jeong et al*., 2005], while accurate characterization of surface reflectance becomes comparatively more important as aerosol loading decreases [*Mi et al*., 2007]. Since the midvisible aerosol optical thickness is not high over most of the world (climatologically less than 0.25 [e.g., *Remer et al*., 2008]), surface reflectance determination remains one of the most important inputs to aerosol remote sensing from space, especially over land surfaces.

[4] Due to the brightness of land surfaces, aerosol retrieval over land is a much more intricate task compared to retrieval over ocean. In particular, the top-of-atmosphere (TOA) reflectances acquired by the satellite sensors at red and near-infrared wavelengths, available from most heritage sensors, are overwhelmed by the surface contributions over desert and semidesert regions, making it difficult to separate the contribution of aerosols to the TOA signal from that of the surface. As a result, previous satellite aerosol retrieval algorithms from these single-view sensors, including the operational SeaWiFS, AVHRR, and MODIS ones that rely on the Dark Target approach [*Kaufman et al*., 1997; *Levy et al*., 2007], were unable to provide aerosol properties over such bright-reflecting regions. It is worth noting that multiangular, polarization, or active (lidar) measurements provide extra constraints on the retrieval system and do enable retrieval of aerosol properties over these bright surfaces with reasonable accuracy [e.g., *Deuzé et al*., 2001; *Martonchik et al*., 2009; *Omar et al*., 2009; *Lyapustin et al*., 2011; *Sayer et al*., 2012b]; however, existing sensors and algorithms with these capabilities typically have comparatively narrow swath widths, shorter data records, and/or require temporal compositing of data, thus making them less suitable for some applications.

[5] The development of the Deep Blue algorithm narrowed these gaps in SeaWiFS and MODIS aerosol products by performing retrievals over bright-reflecting surfaces. The Deep Blue algorithm utilizes blue wavelength measurements from instruments such as SeaWiFS and MODIS, where the surface reflectance over land is much lower than for longer wavelength channels, to infer the properties of aerosols [*Hsu et al*., 2004, 2006]. Using MODIS reflectance data, the Deep Blue technique successfully produced a suite of aerosol products, including aerosol optical thickness, Ångström exponent, and dust absorption over desert and semidesert areas and urban regions, that are an integral part of the operational MODIS collection 5.1 (C5) MOD04 and MYD04 aerosol products for Terra and Aqua, respectively.

[6] Although successful, many of the approximations and assumptions utilized in the first generation of the Deep Blue algorithm needed to be refined and improved to yield better retrievals. One of the most important issues is improving the surface reflectance determination scheme in the retrieval. In the MODIS C5 algorithm, the use of static surface databases limited the algorithm's capability to retrieve aerosols over regions with seasonal vegetation changes, such as in the Sahel and many urban sites. Also, the retrievals were only performed over bright-reflecting surfaces, leading to insufficient information content for retrievals over regions with mixed vegetated and nonvegetated surfaces. Therefore, in order to optimize estimates of surface reflectance, extensive efforts have been made to develop the second generation of the Deep Blue algorithm, which adopts a hybrid approach to take advantage of both the surface reflectance database method and a dynamical surface reflectance method.

[7] In this paper, we will describe the improvements made to the surface reflectance determination, aerosol model selection, and cloud screening schemes in the enhanced Deep Blue algorithm used for processing the MODIS data to create collection 6 (C6) of the Deep Blue products, as well as the SeaWiFS Version 3 products. Section 2 illustrates the methodology of this new algorithm and detailed changes made in each key component compared to the previous C5 algorithm. Section 3 summarizes the results of the aerosol products generated from the new algorithm. Finally, we show provisional validation of the new MODIS Deep Blue C6 products in section 4, followed by some conclusions in section 5. It is noted that the primary goal of this paper is to serve as the overall umbrella document for the development of the enhanced Deep Blue algorithm, while a detailed evaluation of the SeaWiFS and MODIS Deep Blue aerosol product performance using Aerosol Robotic Network (AERONET) measurements is provided by *Sayer et al*. [2012a, 2013], respectively.

2. Development of the Enhanced Deep Blue Algorithm

[8] To retrieve aerosol properties over land, we employ a polarized radiative transfer model [*Dave*, 1972] to compute the reflected intensity field, which is defined by

$$R(\mu, \mu_0, \phi) = \frac{\pi I(\mu, \mu_0, \phi)}{\mu_0 \ F_0} \tag{1}$$

where R is the normalized radiance (or apparent reflectance), F_0 is the extraterrestrial solar flux, I is the radiance at the top of the atmosphere, μ is the cosine of the view zenith angle, μ_0 is the cosine of the solar zenith angle, and ϕ is the relative azimuth angle between the direction of propagation of scattered radiation and the incident solar direction. This radiative transfer code includes full multiple scattering and takes into account polarization; in the blue wavelength range of 0.412 to 0.49 μm, which is vital for this study, Rayleigh scattering is relatively important compared to the longer wavelengths and neglect of polarization in the radiative transfer code would lead to significant errors in the calculated reflectances [*Mishchenko et al*., 1994].

[9] Since the retrieval of aerosol properties from spaceborne sensors requires highly accurate and precise radiometric measurements, sensor calibration and characterization are extremely critical before high quality long-term satellite aerosol data can be achieved for climate study. This is particularly important for Terra/MODIS, which has suffered from aging of

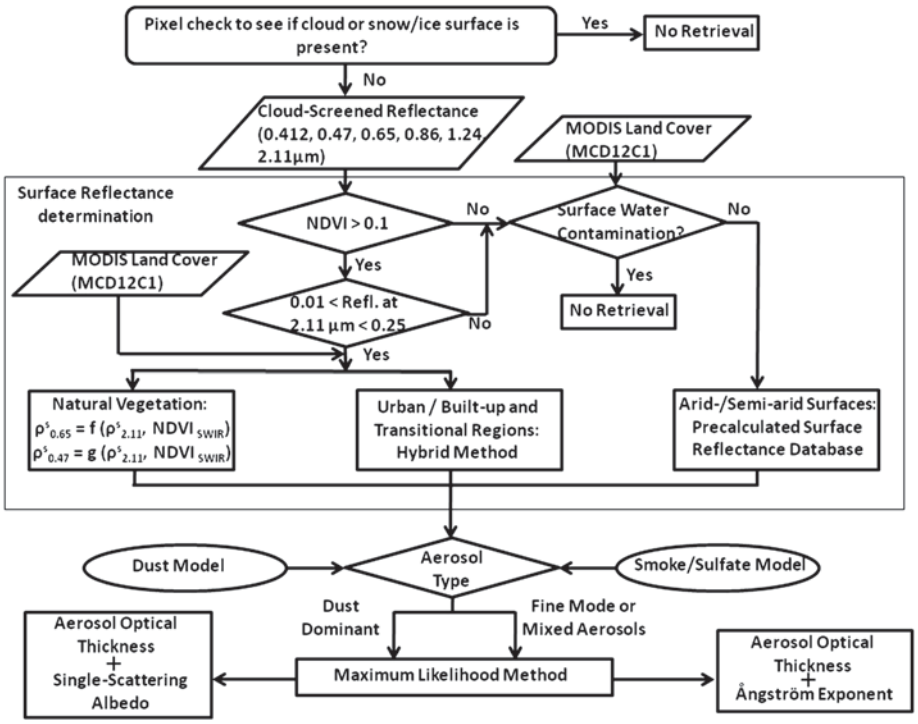

Figure 1. Flowchart of the enhanced MODIS Deep Blue algorithm.

the optics and detectors since its launch in 1999. In fact, the characteristics of the detectors of certain bands, especially band 8 (0.412 μm), have changed significantly over time, leading to increased calibration uncertainty. In order to address this issue, we have utilized a cross-calibration method developed for characterizing the Terra/MODIS detectors by the NASA Ocean Biology Processing Group [*Meister et al*., 2005; *Franz et al*., 2008; *Kwiatkowska et al*., 2008]. Both response versus scan angle and polarization sensitivity corrections have been applied to the MODIS Level 1B reflectances at these blue bands, which are vital to the Deep Blue algorithm. This calibration correction was performed to Terra/MODIS C5 and resulted in substantial improvements in the quality of Deep Blue aerosol retrievals (see *Jeong et al*. [2011] for details). Similar procedures have been also applied to Terra/MODIS C6.

[10] After performing necessary calibration corrections to the Level 1B reflectances, multiple bands (i.e., 0.412, 0.47, 0.65, 0.86, 1.24, 1.38, 2.11, 11, and 12 μm for MODIS) are ingested by the Deep Blue algorithm as inputs for the Level 2 aerosol product retrievals. An overview of the enhanced Deep Blue algorithm over land is provided in the data flow diagram shown in Figure 1. The fundamental steps of the processing stream used to account for different types of land surfaces are described as follows:

[11] 1. Scenes are screened for the presence of clouds by examining the spatial variation of the reflectances from the 0.412 μm channel, the brightness temperatures from 11 and 12 microns, and the 1.38 μm MODIS reflectances. Similar to C5, pixels are first tested for the presence of clouds as well as snow/ice surfaces in the C6 algorithm before the aerosol retrieval processing begins. The retrieval is not performed for cloud- or snow/ice-contaminated pixels.

[12] 2. For a given pixel, the surface reflectances are determined for the 0.412, 0.47, and 0.65 μm channels using one of three different methods: (i) by a dynamic surface reflectance approach, (ii) based upon its geolocation using a precalculated surface reflectance database created from the MODIS or SeaWiFS measurements, or (iii) a combination of the first two approaches. The selection of which method is used depends on the TOA reflectance at shortwave-infrared (SWIR) or near-infrared (NIR) wavelengths (i.e., 2.1 μm for MODIS and 0.865 μm for SeaWiFS) and the normalized difference vegetation index (NDVI), which is defined as

$$\mathrm{NDVI} = (\mathrm{R0.86} - \mathrm{R0.65})/(\mathrm{R0.86} + \mathrm{R0.65})$$

where R0.65 and R0.86 correspond to the TOA reflectance measured at 0.65 and 0.86 μm, respectively.

[13] 3. The 0.412, 0.47, and 0.65 μm TOA reflectances are then compared to reflectances contained in lookup tables with dimensions consisting of the solar zenith, satellite (viewing) zenith, and relative azimuth angles, and the surface reflectance, aerosol optical thickness, and single-scattering albedo. A maximum likelihood method is used to match the appropriate values of aerosol optical thickness and mixing ratio to the measured reflectances. Reflectance data from the 0.65 μm channel is used when the aerosol cloud is thick. For details of the algorithm, see *Hsu et al*. [2004, 2006].

[14] Except for extremely blue-light-absorbing dust, the basic procedures used for aerosol model generation and selection in the enhanced Deep Blue algorithm are similar to the MODIS C5 version. Also, no significant modifications were made in the methodology of deriving Ångström exponent and dust absorption as compared to C5. However, both cloud screening and surface reflectance determination have been substantially changed to improve the accuracy of the retrieved aerosol properties. Details of the cloud screening

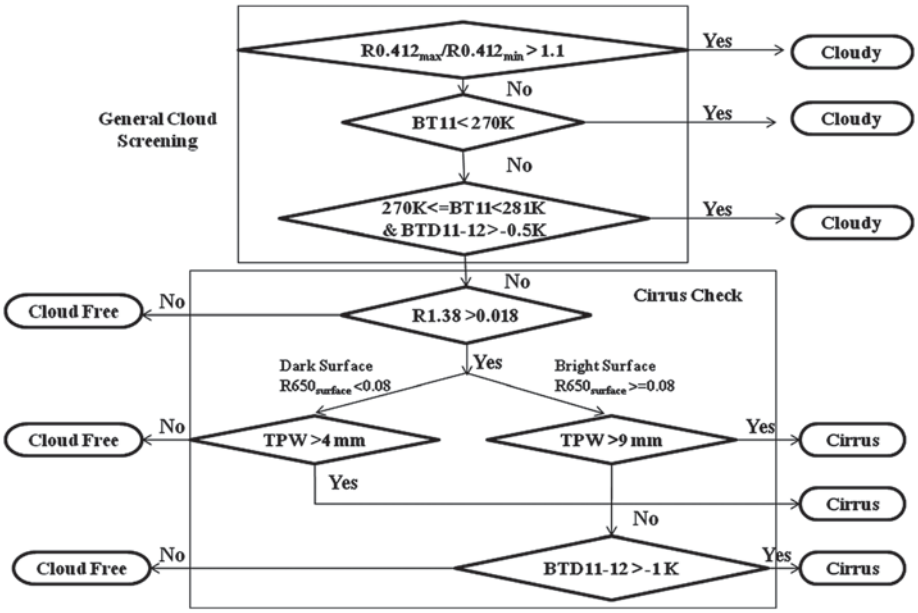

Figure 2. Flowchart of cloud screening used in MODIS C6 Deep Blue algorithm.

scheme (in particular for cirrus) are described below, while the calculation of surface reflectances is discussed in section 2.2.

2.1. Cloud and Snow/Ice Screening

[15] There are several improvements made in the MODIS C6 Deep Blue algorithm regarding flagging procedures in the presence of clouds and snow/ice. The flowchart of detailed steps used in the cloud screening scheme is depicted in Figure 2. Previously, the C5 algorithm used a simple conservative filter based on the variability of TOA reflectance at 0.412 μm (R0.412) within a 3 × 3 pixel area. However, in order to sufficiently filter out cloudy pixels, pixels over areas of highly variable surface reflectance sometimes also got flagged as cloud contaminated. In C6, new checks on brightness temperature (BT) at 11 μm (BT11) and the BT difference (BTD) between 11 μm and 12 μm (BTD11–12) have been implemented in addition to the R0.412 variability filter. By combining the thermal infrared channels with the blue channel, the contrast between clouds and the underlying surface becomes much more discernible, particularly over regions with high surface inhomogeneity. This allows us to relax the criteria for the 0.412 μm variability filter previously used in C5, and more pixels are subsequently retained for aerosol retrievals while still maintaining minimum contamination from clouds.

[16] In addition, significant efforts have been made toward the identification of thin cirrus in C6. In the C5 Deep Blue algorithm, the use of a single threshold method based upon MODIS band 26 (i.e., 1.38 μm), although proven to be robust in general [*Huang et al*., 2011], led to pixels that were sometimes overscreened for cirrus. This was particularly true over moisture-deprived desert regions such as the Sahara; since this MODIS band is strongly sensitive to water vapor absorption, a very low amount of column water vapor in the atmosphere (i.e., less than 5 mm in total precipitable water) could result in elevated values of TOA reflectance at 1.38 μm (R1.38) and thus a false detection of cirrus. Together with the aforementioned spatial variability test, the C6 improvements were found by *Sayer et al*. [2013] to treble the data volume in C6 relative to C5 for some areas.

[17] One such example (for 7 March 2006) is shown in Figure 3. On this day, a significant gap in the C5 Deep Blue retrieved aerosol optical thickness (AOT) (Figure 3b) is seen over the Sahara around 20°N–25°N and 0°–10°E; this gap is triggered by the cirrus flag due to high values of R1.38 over this region. The corresponding MODIS true color image does not seem to indicate the presence of cirrus over this region and the gap in AOT is, therefore, most likely due to the overscreening of cirrus under very dry atmospheric conditions (Figure 3d).

[18] In order to alleviate this problem, we implemented a scheme to jointly use R1.38, BT11, BTD11–12, and the total precipitation water (TPW) obtained from the National Centers for Environmental Prediction (NCEP) as part of the ancillary data input into the C6 algorithm. The use of BTD11–12 has been shown to effectively identify the presence of cirrus cloud [*Hansell et al*., 2007]. As seen in Figure 3e, the regions covered by clouds including cirrus are generally associated with positive BTD11–12 values, consistent with the simulation results of *Hansell et al*. [2007].

[19] In order to account for the coarse resolution (1° latitude × 1° longitude) of the NCEP TPW data and the effects of underlying surfaces on BTD11–12 near the edge of thin cirrus, different steps and thresholds are selected to achieve optimal cirrus screening for different surface types according to the reflectances of underlying surfaces at 0.65 μm based upon the precalculated surface reflectance database. These steps and thresholds are shown in Figure 2. As shown in Figure 3g, this improved scheme results in a substantial increase in the number of aerosol retrievals in C6 from those areas that were previously overscreened in C5.

[20] As shown in Figure 4, we also improved the identification of underlying snow/ice surfaces in C6 by adapting the

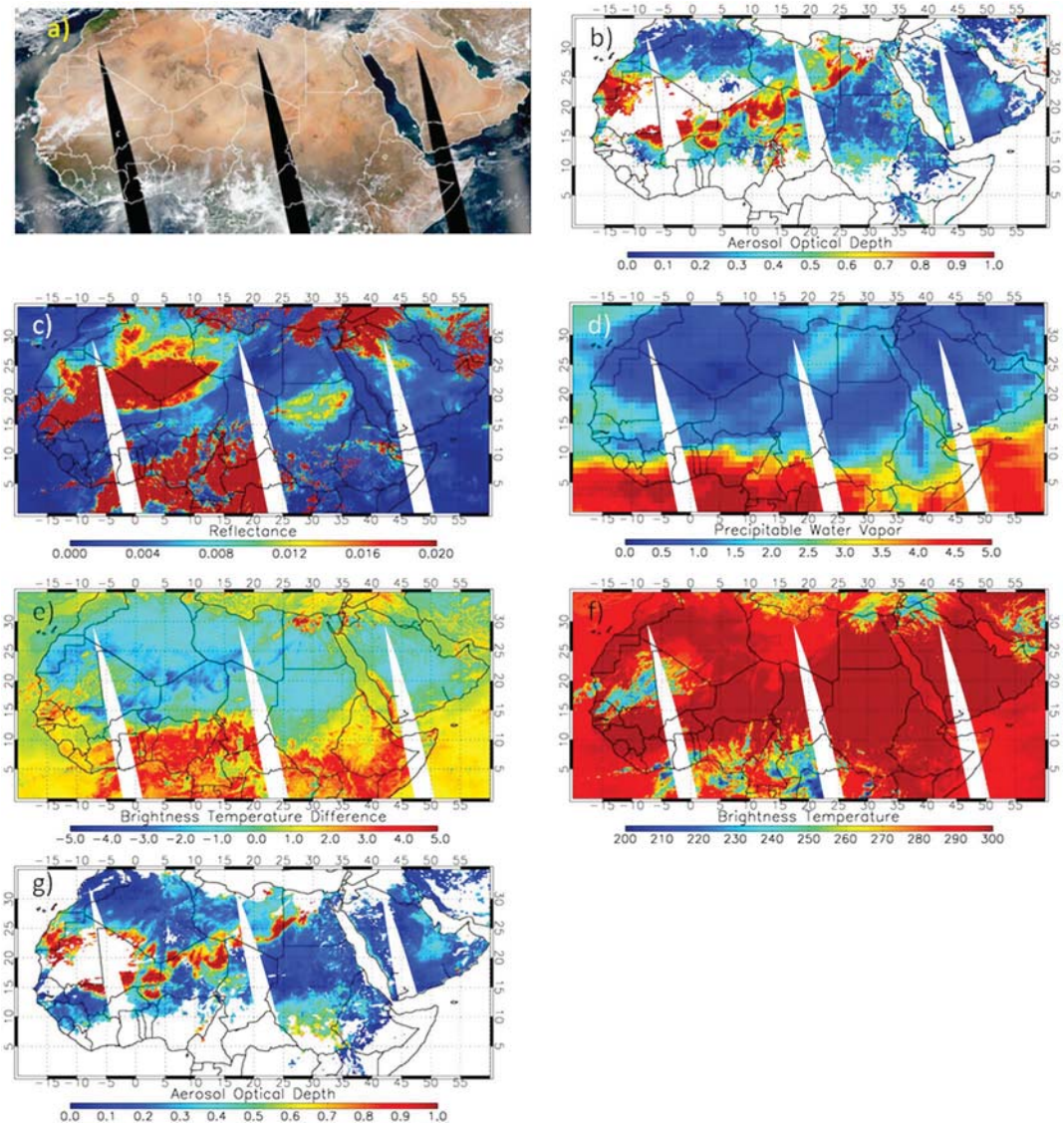

Figure 3. (a–g) A thin cirrus overscreening case over Sahara on 7 March 2006. The impacts of improved cirrus screening on the spatial coverage of AOT retrievals are seen when comparing the C5 AOT map in Figure 3b with the C6 in Figure 3g. The corresponding values of TOA reflectance at 1.38 μm, total precipitable water, brightness temperature difference (BTD11–12), brightness temperature (BT11) used for cirrus screening are depicted in Figure 3c, 3d, 3e, and 3f, respectively. The MODIS true color image is also included in Figure 3a.

method described by *Hall et al.* [1995]. The value of Normalized Difference Snow/Ice Index (NDSI) used in the C6 algorithm is defined as

$$\mathrm{NDSI} = (\mathrm{R0.555–R2.1})/(\mathrm{R0.555} + \mathrm{R2.1})$$

where R0.555 and R2.1 correspond to the TOA reflectance measured by MODIS at 0.555 and 2.1 μm, respectively. We use the reflectance from 2.1 μm instead of the 1.6 μm channel used by Hall because of a detector issue associated with this channel on MODIS/Aqua. Since the snow albedo decreases dramatically from visible wavelengths to near infrared and shortwave infrared, the spectral shape of snow/ice surface is opposite to that of snow-free land surfaces, which allows us to separate snow/ice surfaces from other types of land. To achieve optimal screening of the snow/ice-contaminated

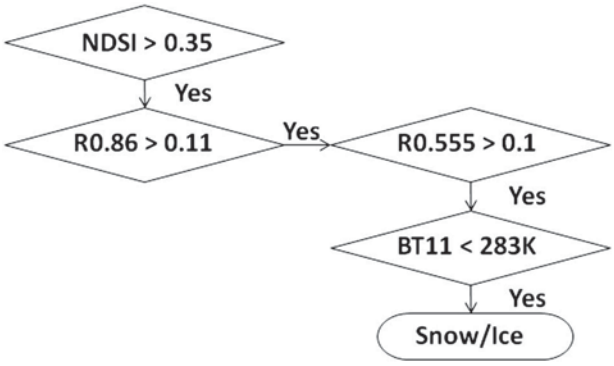

Figure 4. Flowchart of screening for snow/ice surfaces in MODIS C6.

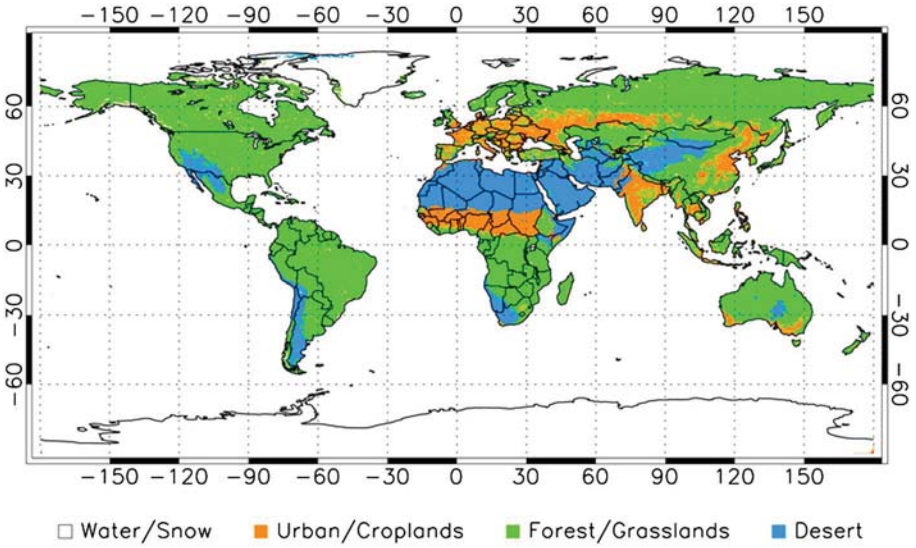

Figure 5. Geographic regions where the three surface reflectance schemes are used in the enhanced Deep Blue algorithm of (1) deserts and semideserts (blue color), (2) general vegetation (green color), and (3) urban/built-up and transitional zones (orange color). The regions with white colors are associated with either water or snow/ice surfaces and thus no overland aerosol retrieval algorithm is applied over these regions.

pixels, the resulting NDSI values are also employed in conjunction with R0.86 and R0.555 as well as BT11 to check their surface temperature and reflectance for potential water and aerosol-laden pixels. In our C6 algorithm testing, this snow/ice identification scheme was found to be particularly important in filtering out erroneous pixels for aerosol retrievals at high latitudes in the Northern Hemisphere during the spring snow/ice melting season.

2.2. Surface Reflectance Determination

[21] To obtain high quality aerosol retrievals, an accurate determination of the underlying surface reflectance is imperative. The surface reflectance used for aerosol retrievals in the previous C5 algorithm was based upon a static precalculated database that was only a function of season. This approach provided reasonable performance over desert and semidesert regions, where the surface reflectances are relatively invariant with time and the effects of the surface bidirectional reflectance distribution function (BRDF) are weaker than those over vegetated areas. However, the surface reflectance database approach was sometimes found to be unsuccessful over vegetated surfaces, especially where seasonal and interannual changes are significant. To improve the estimate of surface reflectance in such cases, it is necessary to instantaneously account for dynamic changes among diverse types of vegetation.

[22] In order to address this issue, extensive efforts have been made in the enhanced Deep Blue algorithm to improve the calculation of surface reflectance. As a result, three different surface reflectance schemes, as depicted in Figure 1, have been adopted in MODIS C6 Deep Blue to optimize retrievals of aerosol properties based upon different surface types. Specifically, we use the MODIS Land Cover and Land Cover Dynamics product (MCD12C1) [*Friedl et al*., 2002] to separate pixels into three categories: (1) arid and semiarid regions, (2) general vegetation, and (3) urban/built-up and transitional regions. The map of regions where these three surface reflectance schemes have been applied is depicted in Figure 5. We also note that, although different wavelength pairs are used for MODIS (0.412, 0.47, 0.65, and 2.1 μm) and for SeaWiFS (0.412, 0.49, 0.67, and 0.87 μm), similar approaches have been applied for calculating surface reflectances to both MODIS C6 and SeaWiFS version 3 (and later) Deep Blue products. The details of surface reflectance calculation for each land category are described below.

2.2.1. Deep Blue Surface Database

[23] For arid and semiarid regions, the surface database method continues to be used in MODIS C6 for determining the surface reflectance. However, several major changes were made in constructing the database. Similar to what was used in C5, the C6 surface database was compiled based upon the minimum reflectivity method at the resolution of 0.1° latitude × 0.1° longitude for each season using MODIS TOA reflectances at 0.412, 0.47, and 0.65 μm (cf. *Hsu et al*. [2004] for details). In C6, better sample statistics have been achieved by increasing MODIS TOA reflectance input data from the 2 years (2005–2006) previously used in C5 to more than 7 years (2002–2009). Additionally, in order to account for potential changes in land cover type within the given season over the same location, the C6 surface database is not only a function of season as in C5 but also of NDVI. The details of construction of the C6 surface database are as follows.

[24] First, to ensure only clear pixels are included in the analysis, the TOA reflectance pixels at the three MODIS bands in the database were tested for clouds, as well as cloud edges and thick aerosol plumes, by employing a conservative screening scheme based upon the standard deviations of 0.412 μm TOA reflectances within a 3 × 3 pixel area centered on the pixel in question. Also, to account for seasonal/transient inland water bodies, water pixels were filtered out if the computed NDVI was negative. Reflectance values that pass these tests are corrected for the contribution from molecular (Rayleigh) scattering and averaged into a daily mean for the given grid.

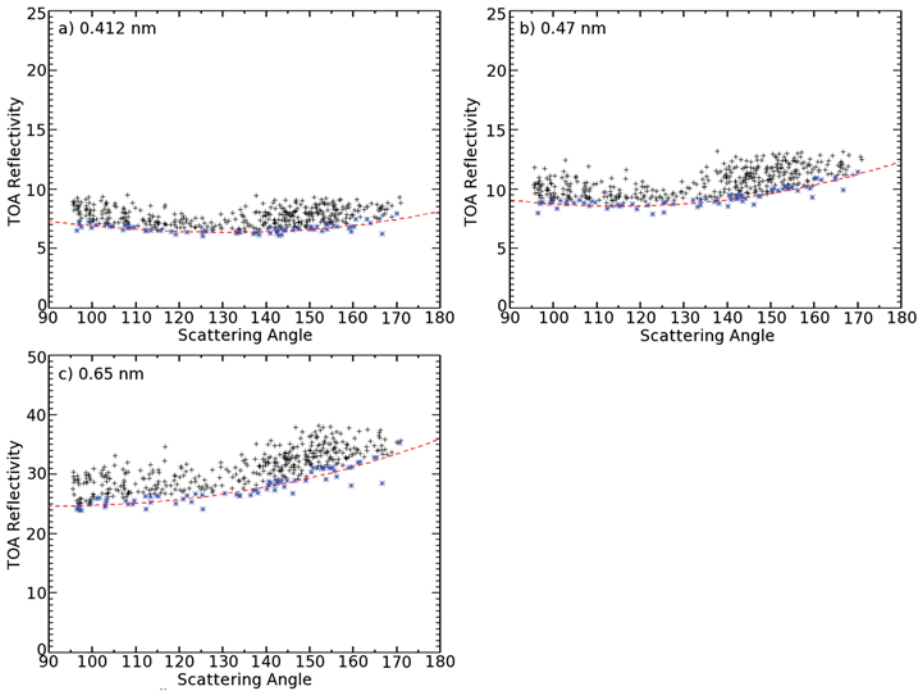

Figure 6. Example of constructing the Deep Blue surface database over Tinga Tingana, Australia for the fall season as a function of scattering angle using MODIS reflectivity (%) at (a) 0.412, (b) 0.47, and (c) 0.65 μm. Blue symbols denote the lowest 15 percentile and the red curve is the polynomial fit through the blue symbols.

[25] Next, these grid cells were divided into four separate groups according to their NDVI: NDVI < 0.18, 0.18 <= NDVI < 0.24, NDVI >= 0.24, and an "all NDVI" group. To further alleviate the problem of outliers due to any remnant presence of cloud shadow or solar eclipse, one additional check was performed to screen out any pixels that lay outside the range of twice the standard deviation from the mean of the samples over every 10° angular bin collected for the given grid cell. Finally, the surface reflectance values in the C6 database are calculated by a second-order polynomial fit through the lowest 15 percentile of grid cell samples against the scattering angles over the given location. The scattering angle (Φ) is defined as

$$\Phi = \cos^{-1}(-\cos\theta_0\cos\theta + \sin\theta_0\sin\theta\,\cos\phi)$$

where θ_0, θ, and ϕ are the solar zenith, sensor view zenith, and relative azimuth angles, respectively. These angular curve fittings of surface reflectance are performed for each NDVI group collected over the given grid cell, provided that a sufficient sample size (50 or more points) is acquired. The derived surface reflectance database therefore depends upon the scattering angle, NDVI, and season. One example of the procedure is provided in Figure 6 using MODIS data over Tinga Tingana, Australia (29°S, 140°E) for the fall season. It is apparent that, for this dry region, the derived surface reflectance at 0.65 μm (Figure 6c) is not only substantially brighter than that at 0.412 μm (Figure 6a) but also its corresponding anisotropy is much larger (shown in the slope of resulting surface reflectance as a function of scattering angle). This is consistent with the expected characteristics of desert surfaces. We note that similar procedures have also been applied to the SeaWiFS data at 0.412, 0.49, and 0.67 μm for constructing the surface reflectance database at these wavelengths.

[26] Figures 7 and 8 show the C6 global maps of surface reflectances at 0.412 and 0.65 μm constructed from our surface database, based upon more than 7 years of MODIS Aqua data, for each season using the above approach for the all NDVI group. In general, the surface reflectance at 0.65 is higher than at 0.412 μm, particularly over dry regions, and exhibits a much more discernible contrast between vegetation and desert areas. We note that there are still gaps in the derived surface reflectance database due to the frequent presence of clouds or snow/ice over certain parts of the world, such as the Amazon and equatorial Africa. As a result, the sample size of data passing our conservative cloud screening scheme was insufficient for computing surface reflectance polynomial fitting with rigorous statistics over such regions. However, these regions are associated with vegetated land areas, which will not require the use of this surface database to determine the surface reflectance in the C6 algorithm.

2.2.2. Vegetated Land Surfaces

[27] Over vegetated land surfaces, we retrieve aerosol properties by taking advantage of the spectral relationship in surface reflectance between visible and longer wavelengths (i.e., 0.87 for SeaWiFS and 2.1 μm for MODIS) to account for the effect of the ever-changing dynamics of vegetation phenology on the surface reflectance. However, in order to better determine the spectral surface reflectance relationship, contributions from the atmosphere need to be removed from the satellite-measured signals. This task was accomplished by collocating satellite measurements from MODIS and SeaWiFS with ground-based Aerosol Robotic Network (AERONET) [*Holben et al.*, 1998] data. The satellite-derived surface reflectances at visible wavelengths (i.e., 0.47 and

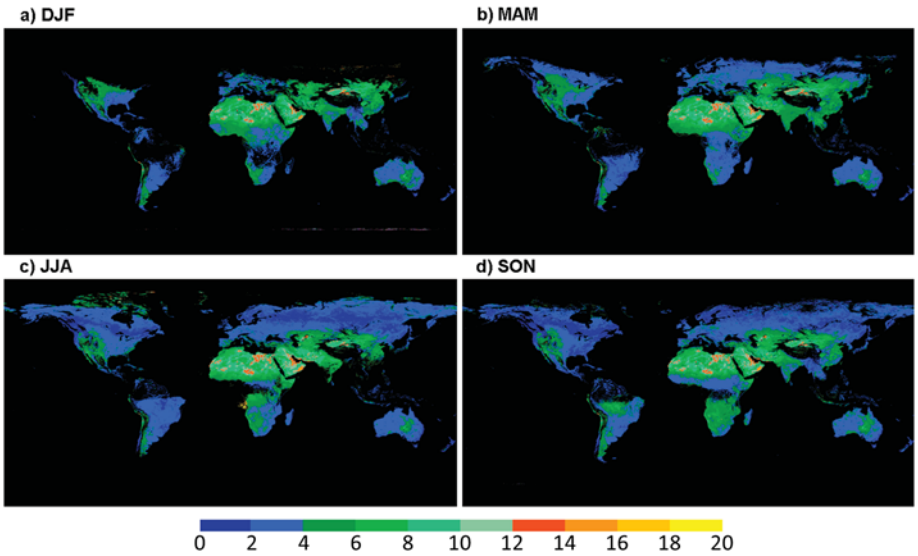

Figure 7. (a–d) Seasonal maps of surface reflectance database at 0.412 µm used in the Deep Blue algorithm. The color scale indicates reflectance, in percent. The black colored regions are associated with water body, snow/ice surface, or the frequent presence of clouds.

0.65 µm for MODIS and 0.49 and 0.67 µm for SeaWiFS) were then obtained using AERONET AOT and single-scattering albedo information to perform an atmospheric correction. Hereinafter, such derived surface reflectances based on the explicit atmospheric corrections performed using collocated satellite measurements and AERONET data will be referred to as "benchmark" surface reflectances. Since the uncertainty of deriving surface reflectance increases significantly as aerosol loading becomes larger, we only include samples for analysis when the AERONET AOT at 0.5 µm < 0.5. The correction procedure is described below.

[28] For MODIS data, our approach estimates the surface reflectances at visible channels based upon the TOA reflectances at 2.1 µm (R2.1) and land cover type using the following formulas:

$$\mathrm{ESR}_{0.65} = \mathrm{a} + \mathrm{b}^{*}\mathrm{R2.1} + \mathrm{c}^{*}(\mathrm{R2.1})^{2} \tag{2}$$

$$\mathrm{ESR}_{0.47} = \mathrm{d} + \mathrm{e}^{*}\mathrm{ESR}_{0.65} \tag{3}$$

where ESR is the estimated surface reflectance and a, b, c, d, and e are coefficients determined by a least squares fitting to the derived benchmark surface reflectance data over the AERONET sites. The spectral surface reflectance relationships given by the above formulas can vary depending upon the land cover type and season.

[29] Figure 9 shows an example of these spectral relationships for different surface types over the United States, based upon 2004 springtime MODIS data. It is apparent that the spectral surface reflectance relationships for most naturally

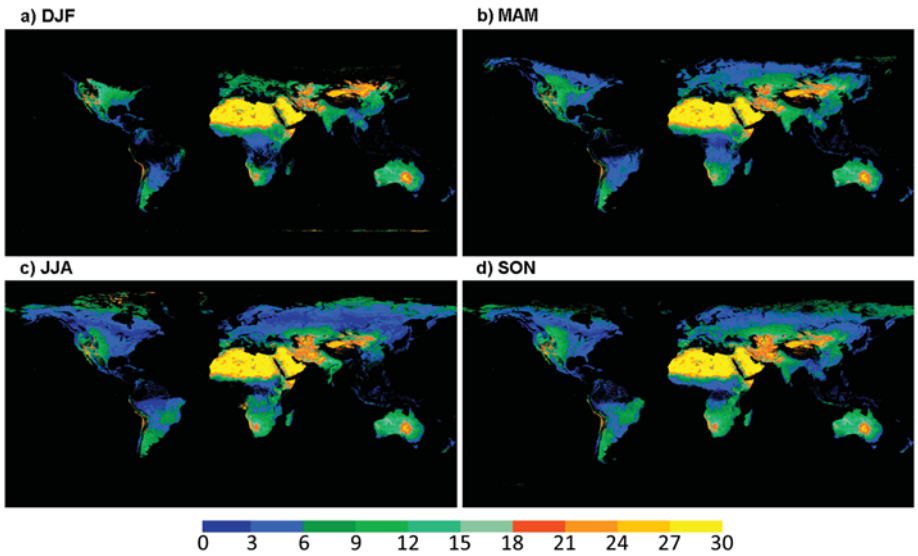

Figure 8. Same as Figure 7, except for 0.65 µm.

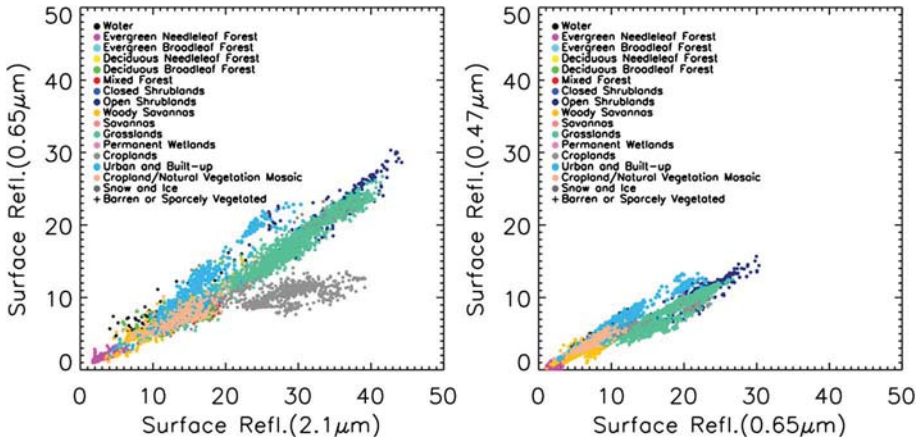

Figure 9. MODIS-derived spectral surface reflectance relationships (left) between 0.65 and 2.11 μm and (right) between 0.47 and 0.65 μm during March-April-May 2004, as a function of land cover type from MODIS (MCD12C1).

vegetated surfaces can be collapsed into a single relationship, while the relationships for cropland (gray color) or for urban and built-up regions (light blue color) deviate distinctively from those for naturally vegetated surfaces. Based on these findings, we derive the surface reflectance relationship separately for each land cover type (i.e., naturally vegetated area and cropland) and seasons, with a consideration of the changes of surface property for cropland by establishing subgroups depending on the values of $NDVI_{SWIR}$, which is defined as

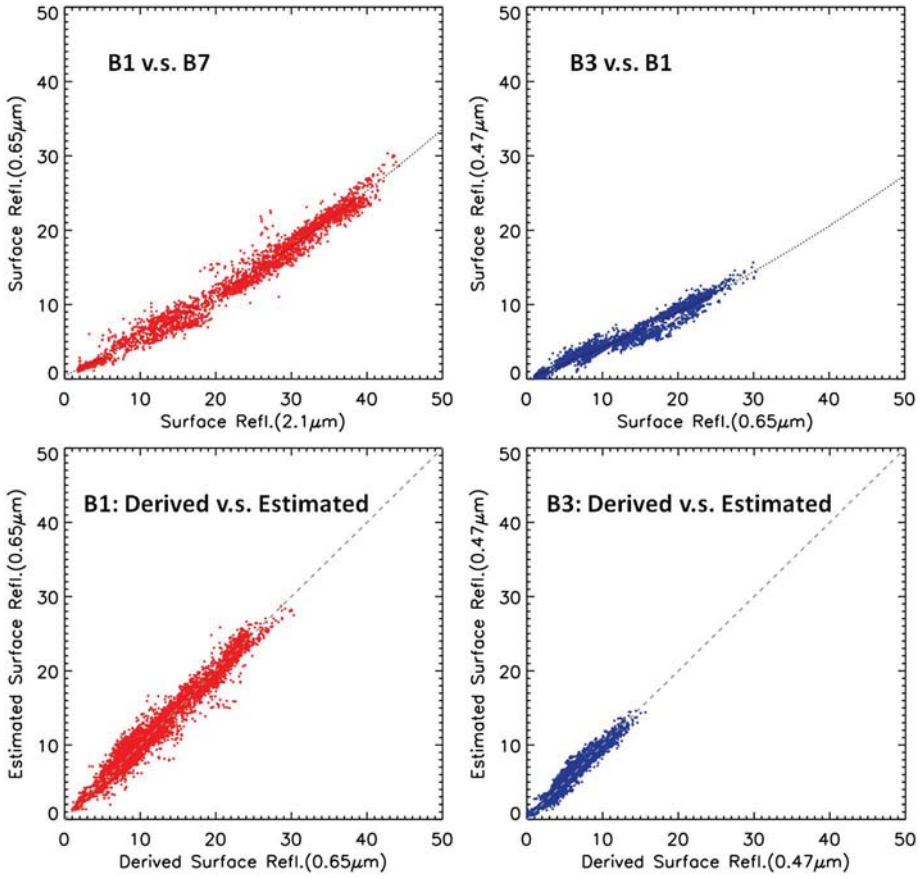

Figure 10. (top) The spectral relationship of (left) 0.65 versus 2.1 μm and (right) 0.47 versus 0.65 μm based upon benchmark surface reflectances from MODIS for naturally vegetated regions during March-April-May 2004. The dotted line represents the second-order least squares fit through the data points. (Bottom) Comparisons between the derived benchmark and estimated surface reflectance for (left) 0.65 and (right) 0.47 μm channels. The dashed line denotes the one-to-one line.

Table 1. Surface Reflectance Coefficients Over Naturally Vegetated Regions for MODIS 0.47 and 0.65 μm[a]

	R0.65/R2.1 (a, b, c)	R0.47/R0.65 (d, e)
DJF/MAM	0.5526, 0.4801, 0.0038	−0.3305, 0.4830
JJA	0.4413, 0.4606, 0.0045	−0.5841, 0.4961
SON	1.1749, 0.3560, 0.0067	0.0048, 0.4429

[a]These values inside each cell correspond to a, b, c, d, and e in equations (2) and (3).

$$\mathrm{NDVI}_{\mathrm{SWIR}} = (\mathrm{R1.24} - \mathrm{R2.1})/(\mathrm{R1.24} + \mathrm{R2.1})$$

We note that this approach is not applied to the urban/built-up zones, since the hybrid method is used in the enhanced Deep Blue algorithm over such regions.

[30] An example of the derivations of spectral surface reflectance relationships for naturally vegetated surfaces during the March-April-May season is provided in the upper panels of Figure 10. The values of the coefficients for estimating the surface reflectances in equations (2) and (3) are determined by a second-order polynomial least squares curve fit through the data points. The resulting coefficients a–e in equations (2) and (3) for each season are tabulated in Tables 1 and 2 for naturally vegetated regions and croplands, respectively. To validate the fit, comparisons between these estimated surface reflectances at 0.47 and 0.65 μm and the corresponding benchmark surface reflectances were performed, and these comparisons are presented in the lower panels of Figure 10. As shown in the figure, the estimated surface reflectances show reasonable agreement (root-mean-square error of 1.2% for 0.65 μm, 0.67% for 0.47 μm) with the benchmark surface reflectances.

[31] For SeaWiFS aerosol retrievals over vegetated regions, the enhanced Deep Blue algorithm utilizes the 0.49, 0.67, and 0.865 μm bands to derive surface reflectances due to lack of the SWIR bands for SeaWiFS. Figure 11 shows that, for all the collocated SeaWiFS/AERONET data acquired over the continental U.S. during spring 2004, the atmospherically corrected surface reflectances (i.e., benchmark surface reflectances) from SeaWiFS exhibit a linear relationship with the corresponding TOA reflectances at 0.865 μm (after the Rayleigh scattering contribution has been removed). Figure 11 also shows that this relationship is a function of NDVI. Based on these results, we developed an approach that estimates the surface reflectance at visible channels based upon the Rayleigh-corrected TOA reflectances at the near-infrared channel (i.e., 0.865 μm) and NDVI values using the following formulas:

$$\mathrm{ESR}_{0.67} = \mathrm{RCR}_{0.865}*(\mathrm{a}*\mathrm{NDVI'} + \mathrm{b}) + c \quad (4)$$

$$\mathrm{ESR}_{0.49} = \mathrm{RCR}_{0.865}*(\mathrm{d}*\mathrm{NDVI'} + \mathrm{e}) + \mathrm{f} \quad (5)$$

where ESR and RCR are the estimated surface reflectance for the 0.67 and 0.49 μm bands and Rayleigh-corrected reflectances at 0.865 μm, respectively; a, b, c, d, e, and f are coefficients determined by least squares fitting to the benchmark surface reflectances; and

$$\mathrm{NDVI'} = (\mathrm{RCR}_{0.865} - \mathrm{RCR}_{0.67})/(\mathrm{RCR}_{0.865} + \mathrm{RCR}_{0.67}) \quad (6)$$

The regression coefficients were derived seasonally and according to 3 NDVI' classes: $0.10 < \mathrm{NDVI'} <= 0.20$; $0.20 < \mathrm{NDVI'} <= 0.55$; $\mathrm{NDVI'} > 0.55$. In addition, aerosol retrievals using this approach are only performed for pixels with a surface reflectance < 0.23 and an $\mathrm{NDVI'} > 0.1$. The resulting coefficients for each NDVI' category and season are tabulated in Tables 3 and 4 for 0.67 and 0.49 μm SeaWiFS bands, respectively.

[32] Comparisons of the SeaWiFS estimated surface reflectance at 0.49 μm using this approach exhibit reasonable agreement for all four seasons with the corresponding benchmark surface reflectance regardless of the AOT values. Examples of these comparisons for spring (March-April-May) and fall (September-October-November) are shown in the upper panels of Figure 12. The corresponding AOT value for each pixel is indicated by the color of the symbol. The satellite-estimated surface reflectances at 0.67 μm are seen to also correlate well with the benchmark surface reflectance shown in the lower panels of Figure 12, except for high AOT cases. This is likely due to the fact that the slopes of surface reflectance from 0.865 to 0.67 μm are more sensitive to the NDVI' values than the 0.865 to 0.49 μm slopes shown in Figure 11. Therefore, bias in NDVI' due to the presence of aerosols has a stronger impact on retrieving the surface reflectance at 0.67 than it does for 0.49 μm using this approach.

[33] The dependence of the deviation between benchmark 0.49 and 0.67 μm surface reflectance and satellite-estimated values as a function of AOT at 0.49 μm from the AERONET data is further investigated and plotted in Figures 13a and 13b. We note that, while the surface reflectance bias at 0.49 μm appears to be independent of AERONET AOT, there is a clear correlation between the surface reflectance bias at 0.67 and AOT at 0.49 μm. To account for this effect, the estimated surface reflectance at 0.67 μm was readjusted by using satellite-retrieved AOT at 0.49 μm in conjunction with the linear regression line indicated in Figure 13b before it is used for aerosol retrievals at 0.67 μm.

[34] As a result, the surface reflectance determination schemes for MODIS and SeaWiFS described above are being applied to the naturally vegetated regions and cropland indicated by the areas with green color in Figure 5 for aerosol retrievals in the enhanced Deep Blue algorithm. For the urban/built-up and transitional zones, the surface reflectances at visible wavelengths do not have simple and well-behaved

Table 2. Surface Reflectance Coefficients Over Cropland for MODIS 0.47 and 0.65 μm[a]

	$\mathrm{NDVI}_{\mathrm{SWIR}} < 0.35$		$\mathrm{NDVI}_{\mathrm{SWIR}} >= 0.35$	
	R0.65/R2.1 (a, b, c)	R0.47/R0.65 (d, e)	R0.65/R2.1 (a, b, c)	R0.47/R0.65 (d, e)
DJF/MAM	6.2828, 0.1658, 0.0	2.6884, 0.2751	−0.9766, 0.6213, 0.0	0.9126, 0.3982
JJA	5.2395, 0.2077, 0.0	0.2451, 0.5442	−0.1187, 0.5036, 0.0	−0.0736, 0.5345
SON	−2.2642, 0.6781, 0.0	1.2493, 0.3576	−1.2799, 0.6161, 0.0	1.2724, 0.2039

[a]These values inside each cell correspond to a, b, c, d, and e in equations (2) and (3).

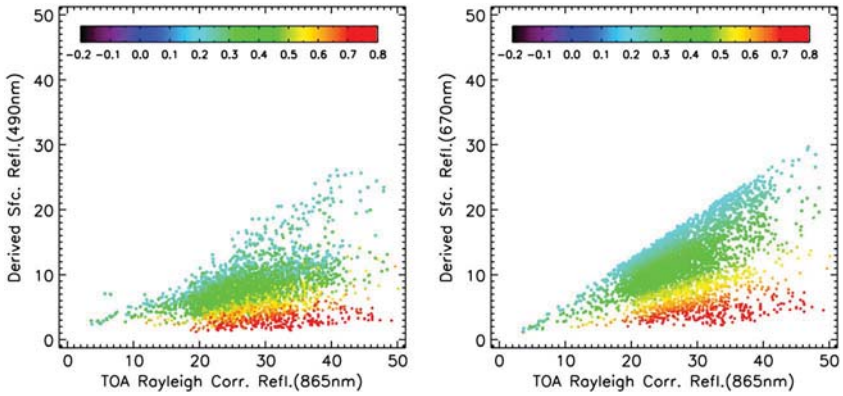

Figure 11. SeaWiFS derived surface reflectance using aerosol properties from AERONET measurements at (left) 0.49 and (right) 0.67 μm as function of Rayleigh-corrected reflectance at 0.865 μm at the top of the atmosphere and normalized difference vegetation index (NDVI) for the spring season. Color bar shows the values of NDVI for each point.

relationships with NDVI as those for the densely vegetated regions and thus a hybrid approach is developed for these types of land cover as described in the next subsection.

2.2.3. Hybrid Approach Over Urban/Built-Up and Transitional Regions

[35] The derivation of surface reflectances for aerosol retrievals over the urban/ built-up regions and cropland/transitional zones is highly challenging for a number of reasons. First, as shown in Figure 9, the relationships between the visible and 2.1 μm surface reflectances over these types of land surfaces exhibit more complex behavior and are not in line with those for naturally vegetated areas. Second, although their surface reflectances are not as bright, they are much more susceptible to seasonal changes of vegetation growing and dying phases as well as the effects of surface BRDF. Third, surface inhomogeneity is often a problem, particularly over large cities where vegetation resides close to buildings, resulting in high variability of surface brightness throughout the landscape. To address these issues, we developed a hybrid approach for determining surface reflectance by combining the Deep Blue surface database with the angular shapes of surface BRDF derived using AERONET measurements.

[36] To derive these BRDF angular shapes, collocated satellite/AERONET data sets were compiled using 8 years of MODIS data (2003–2010) and more than 10 years of SeaWiFS data (1998–2010) acquired within a distance of 0.1° radius from the AERONET sites over transitional and urban/ built-up regions. The satellite-estimated surface reflectances were then computed at 0.412, 0.47, and 0.65 μm for MODIS and 0.412, 0.49, and 0.67 μm for SeaWiFS using aerosol information from the AERONET measurements by applying the same atmospheric correction procedures mentioned in section 2.2.2. Once again, only pixels with AERONET AOT < 0.5 were included for such studies in order to minimize the uncertainty of aerosol contribution in determining surface reflectance. Also, to account for the effect of vegetation changes, the resulting surface reflectances were divided into three different groups according to their NDVI values: NDVI < = 0.19, 0.19 < NDVI < = 0.24, NDVI > 0.24. Regression lines were then computed as a function of scattering angle using a second-order polynomial fit for each NDVI group and each season to obtain the shapes of surface BRDF. One example of these procedures for Banizoumbou (13°N, 2°E) in the Sahel is shown in Figures 14 and 15 for 0.412 and 0.470 μm, respectively.

[37] It is apparent in these figures that the surface greenness at this location has a strong seasonal cycle, with more dense vegetation land cover (i.e., higher NDVI) in fall (September–November) and more dry land surfaces (i.e., lower NDVI) in spring (March–May). However, during the transitional time periods such as summer, the vegetation grows rapidly over a short period of time due to the arrival of rainfall in the region, leading to a large temporal gradient in the NDVI and thus the surface reflectance values. As shown in Figures 14 and 15, the resulting angular shapes of surface reflectances are derived by applying polynomial fits through the data points stratified by NDVI to characterize the surface properties based upon the state of vegetation. Finally, we combine these derived angular shapes with surface reflectance values from the Deep Blue surface database at 135° scattering angle described in section 2.2.1 to compute surface reflectance for aerosol retrievals over these urban/ built-up and transitional zones. This hybrid method has been applied to the regions of orange color indicated in Figure 5 for both SeaWiFS and MODIS data.

[38] In order to better track the performances of the three different approaches mentioned above, a new Scientific Data Set (SDS) named "Deep_Blue_Algorithm_Flag_Land" was

Table 3. Surface Reflectance Coefficients Over Vegetated Regions for SeaWiFS 0.67 μm[a]

	0.10 < NDVI' < =0.20	0.20 < NDVI' < =0.55	NDVI' > 0.55
MAM	−1.5184, 0.9797, −1.2189	−1.0948, 0.8639, −0.6745	−0.7002, 0.6672, −0.9535
JJA	−1.5077, 0.9695, −0.8751	−1.0772, 0.8724, −0.9543	−0.6919, 0.6721, −1.1697
SON	−1.5244, 0.9743, −1.1274	−1.0676, 0.8650, −0.9757	−0.6497, 0.6204, −0.3580
DJF	−1.6123, 0.9736, −0.7547	−1.0597, 0.8491, −0.5760	−0.7054, 0.6767, −0.6852

[a]The three values inside each cell are corresponding to a, b, and c in equation (4).

Table 4. Surface Reflectance Coefficients Over Vegetated Regions for SeaWiFS 0.49 μm[a]

	0.10 < NDVI' < =0.20	0.20 < NDVI' < =0.55	NDVI' > 0.55
MAM	−1.1617, 0.5278, 0.7483	−0.5822, 0.4222, 1.3564	−0.4264, 0.3903, 0.2547
JJA	−0.5839, 0.3888, 2.2656	−0.5500, 0.3699, 2.6355	−0.3990, 0.3881, −0.3469
SON	−0.9448, 0.4835, 0.9249	−0.5271, 0.3615, 1.9300	−0.3185, 0.3040, 0.3497
DJF	−1.3836, 0.4686, 3.2991	−0.6764, 0.4439, 1.4341	−0.4177, 0.4442, −1.2915

[a]The three values inside each cell correspond to d, e, and f in equation (5).

added into the MODIS C6 Deep Blue products, as shown in Table 5. One of three different values (i.e., Deep Blue surface database, vegetated land surfaces, or mixed) will be reported in this SDS to indicate which one of these three methods was used in the actual retrieval for the given cell.

2.3. Aerosol Model Selection

[39] The general scheme for selecting aerosol models used in C6 retrievals is similar to C5 [*Hsu et al*., 2004, 2006]. However, additional use of MODIS infrared channels has been employed in C6 to identify the presence of extremely absorbing mineral dust. According to the findings of *Hansell et al*. [2007], the use of the brightness temperature difference between 8.6 and 11 μm (BTD8–11) is robust in detecting strongly absorbing dust such as the silicates (e.g., quartz, clays, etc.), which have strong Restrahlen bands and often absorb infrared radiation more at 8.6 than at 11 μm. Since these types of mineral dust also exhibit strong absorption of visible light, in particular for blue wavelengths, nonidentification of such aerosols will lead to the underestimation of AOT in the Deep Blue retrieval algorithm.

[40] One example of such a case is shown in Figure 16 for 9 July 2007. On this day, extensive dust plumes were seen in the MODIS/Aqua true color image (Figure 16a) around the Bodele Depression and the region surrounding it (14°N–20°N, 10°E–20°E) as well as over the western part of the Sahara (15°N–30°N, 15°W–5°E, as indicated by the circle). In Figure 16b, the heavy dust loading near the Bodele Depression was reflected in the MODIS C5 AOT map; however, the dust plumes over the western part of the Sahara were not captured well by the C5 algorithm. In order to address this issue, we added a new heavy dust flag in the C6 algorithm,

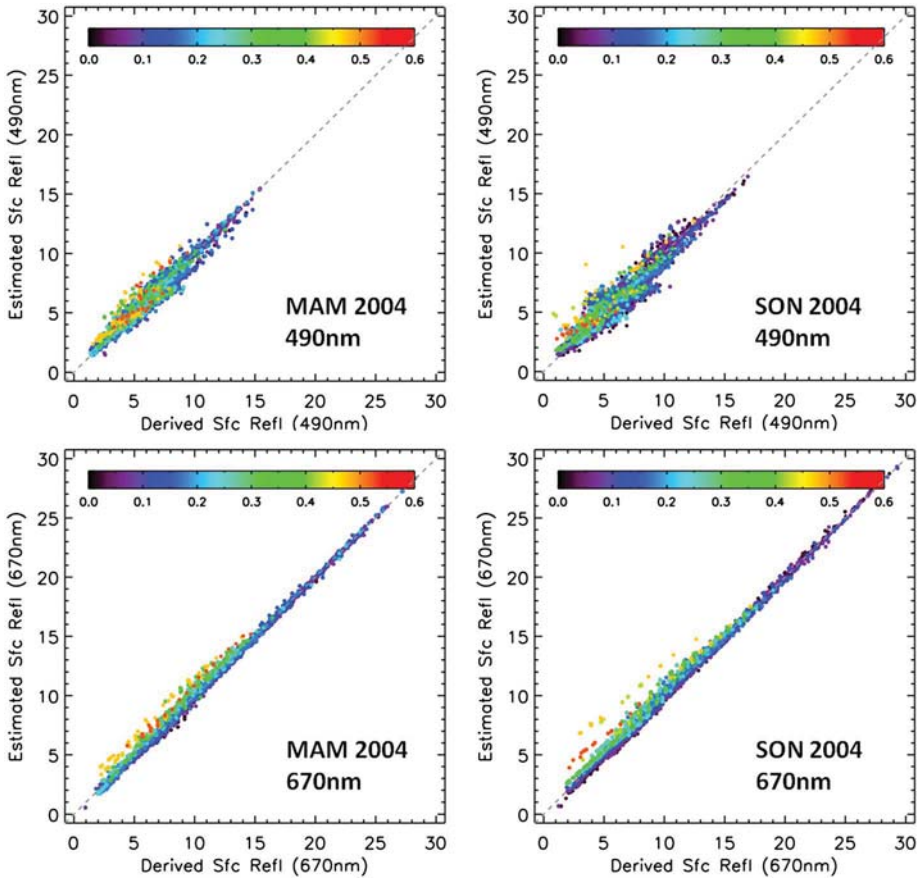

Figure 12. Comparisons of the estimated surface reflectance at (top) 0.49 and (bottom) 0.67 μm with the derived benchmark surface reflectance from SeaWiFS at the same wavelength after atmospheric corrections using AERONET AOT data for (left) March–May and (right) September–November. Color indicates AOT at 0.49 μm interpolated from AERONET AOTs using Ångström exponent.

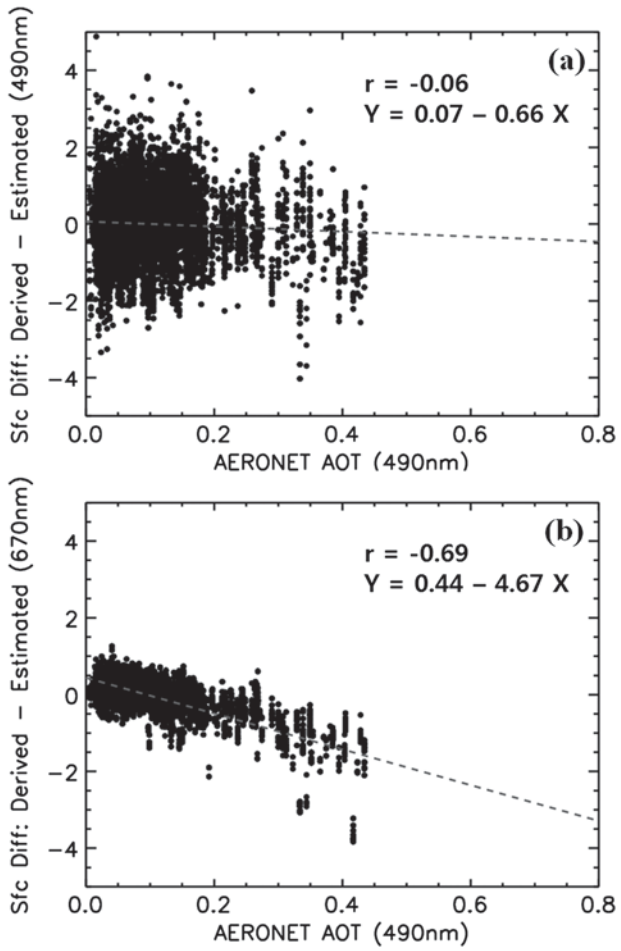

Figure 13. Differences between estimated and derived surface reflectance (units of percent reflectance) from SeaWiFS (a) at 0.49 and (b) at 0.67 μm as function of aerosol optical thickness (AOT) at 0.49 μm. Gray dashed lines stand for linear fitting lines. Correlation coefficient (r) and the linear fitting equations are presented in each plot.

which is based upon the D* value developed by *Hansell et al.* [2007]; D* is defined as

$$D^* = \exp\{[(BTD11 - 12) - A]/[(BTD8 - 11) - B)]\}$$

where parameters A and B are the thermal offsets for BTD11–12 and BTD8–11, respectively. In the C6 algorithm, the values of −0.05 and 10.0 are used for A and B for the D* calculation. When the condition $D^* > 1.1$ is detected, the retrieval algorithm will go directly to the three-wavelength (0.412, 0.47, and 0.65 μm) approach and bypass the two-wavelength (0.412 and 0.47 μm) method. As described in *Hsu et al.* [2004], an initial step of using the two-wavelength method is performed in the Deep Blue algorithm to determine if there is sufficient aerosol loading in the atmosphere for retrieving aerosols with the 0.65 μm channel over bright surfaces, where the surface contribution dominates the TOA reflectance under low to moderate aerosol loading conditions. If the criteria on aerosol loadings are met for a given pixel, the algorithm will conduct a three-wavelength retrieval, which is less susceptible to the presence of strongly blue-light-absorbing aerosols compared to the two-wavelength retrieval.

[41] As displayed in Figure 16c, the dust plumes in the problematic areas over the western part of the Sahara are well correlated with elevated values in D*, although other regions with high dust loadings that are apparent in the MODIS true color image do not stand out in the D* map. This is likely due to the combination of the different sensitivity of D* to different types of mineral dust as well as the effects of underlying surface emissivity on D*. By using this new heavy dust flag, the C6 Deep Blue algorithm is able to produce better results for retrieved AOT (Figure 16d) for strong blue light-absorbing dust as compared to the C5 AOT shown in Figure 16b. It is noted that only the AOT retrievals with a quality assurance flag (QA) of 2 or 3 were shown in the C5 and C6 AOT maps in Figure 16. Therefore, the gaps in the retrieved AOT near the middle of MODIS swath caused by the use of the scattering angles filter in the QA determination scheme (as described below) were only seen in the C5 map and not in the C6 one. Other differences in the retrieved AOT values between C5 and C6 primarily result from the changes made in the C6 surface reflectance determination scheme.

2.4. Data Quality Flag and Uncertainty Estimate

[42] As shown in Table 5, the values of the QA flag and estimated uncertainty assigned to each pixel are now added in C6 as part of the Deep Blue SDS product suite. Similar to the convention used in C5, the quality flags in C6 also have four different levels (i.e., QA = 0, 1, 2, 3 with 0 for no retrieval, 1 as the worst quality retrieval and 3 for the best data quality). However, there are several major changes in the QA flag selection procedures. For example, in C5 the QA flag was limited to 1 for scattering angles greater than 168° due to increasing surface reflectance at high scattering angles (i.e., BRDF hot spots) over many types of surfaces. This constraint is lifted in C6 due to improved statistics obtained by using more than 7 years of MODIS data over the high scattering angle range used in the analysis for constructing the Deep Blue surface database and the use of a hybrid approach to better characterize the angular shapes in C6.

[43] As a result of the improvements made in surface reflectance determination, the selections of *QA* flag in C6 only simply rely on the number (N) of retrieved AOT pixels at 0.550 μm (i.e., minimum $N = 40$ and 60 out of 100 for $QA = 2$ and 3, respectively) and their standard deviation (σ) within 10×10 pixels (i.e., maximum $\sigma = 0.18$ and 0.15 for $QA = 2$ and 3, respectively) and no longer depend on surface types as used in C5. Overall, the criteria for achieving higher *QA* is more relaxed in C6, leading to a higher number of retrieved pixels reaching $QA = 2$ or 3 as compared to C5. The estimated uncertainty of the retrieval for each cell is also reported in C6 based upon the corresponding viewing geometry and air mass factor. A detailed description of the estimated uncertainty calculation is included in *Sayer et al.* [2013]. It is important to note that since pixels with $QA = 1$ for the Deep Blue AOT product could potentially still have cloud contamination issues, a new SDS named "Deep_Blue_Aerosol_Optical_Depth_550_Land_Best_Estimate" was created in C6 to report good quality pixels with $QA = 2$ or 3; we highly recommend that this SDS be used by the general user community.

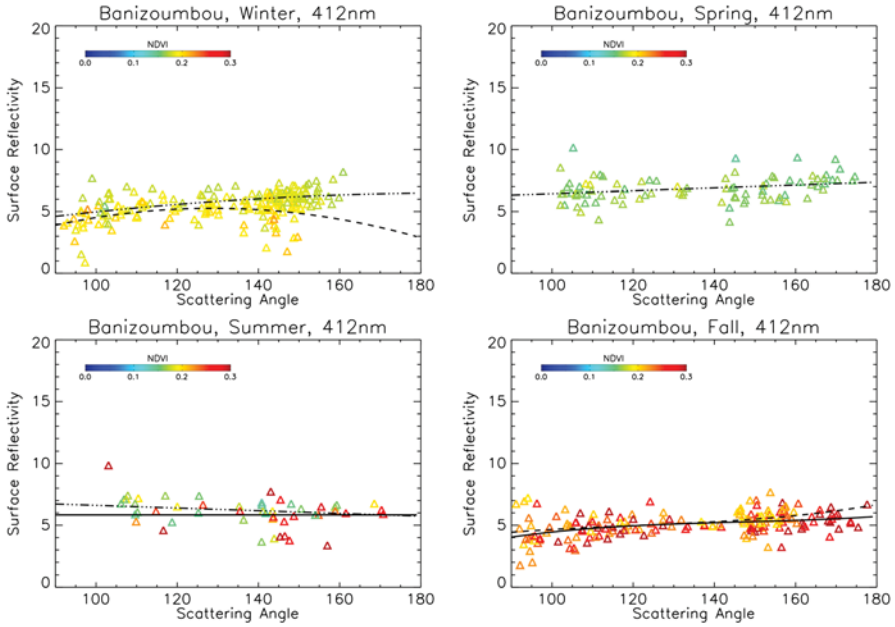

Figure 14. Atmospheric corrected surface reflectance at 0.412 µm for MODIS Aqua using AERONET aerosol measurements over Banizoumbou. The color of the symbol is associated with the NDVI value of the given pixel. The dash-dotted, dashed, and solid lines represent the line fit for each group of data with NDVI < 0.19, 0.19 < = NDVI <2.4, and NDVI > =2.4, respectively.

3. Results and Discussions

[44] We have used the C6 Deep Blue algorithm described above to process reflectance data from the Aqua MODIS instrument for 17–18 July 2004, to compare with data from the C5 algorithm. Figure 17 illustrates the advantage of the enhanced Deep Blue retrieval. As seen in the true color images (left column), smoke from large fires burning in Alaska and northwestern Canada traveled across the North American continent, impacting the Great Lakes region. The C5 Deep Blue aerosol retrieval, shown in the middle column, is limited to bright underlying surfaces. The resulting retrieval, therefore, covers very little of the mostly vegetated Great Lakes region. The enhanced Deep Blue algorithm extends the capability of Deep Blue to the vegetated, or darker, surface types. The right column of Figure 17 shows nearly complete AOT data, excluding only cloudy and water surfaces. The areas of high AOT in the enhanced Deep Blue images (right column, values in orange, red) appear to correspond well to the smoke plumes visible in the true color images; the 17

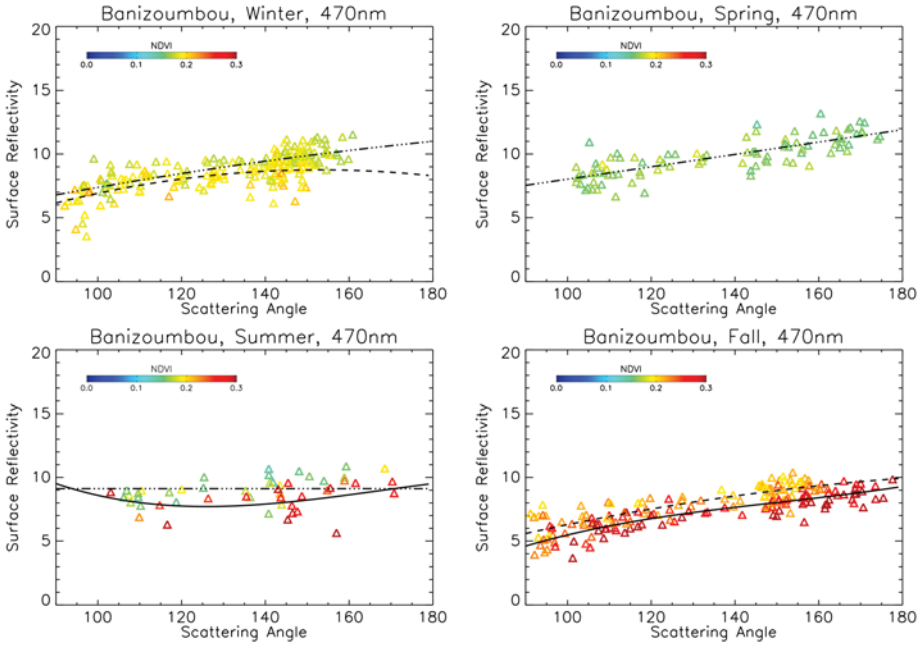

Figure 15. Same as Figure 14, except for 0.47 µm.

Table 5. List of SDS Names for MODIS Collection 6 Deep Blue Aerosol Products

Name	Dimensions[a]	Description
Deep_Blue_Angstrom_Exponent_Land	[Cell_Along_Swath, Cell_Across_Swath]	Angstrom Exponent Over Land.
Deep_Blue_Aerosol_Optical_Depth_550_ Land	[Cell_Along_Swath, Cell_Across_Swath]	Aerosol Optical Depth at 550 nm Over Land.
Deep_Blue_Aerosol_Optical_Depth_550_ Land_Best_Estimate	[Cell_Along_Swath, Cell_Across_Swath]	Aerosol Optical Depth at 550 nm Over Land Filtered by Quality ($QA = 2,3$ only).
Deep_Blue_Aerosol_Optical_Depth_550_ Land_STD	[Cell_Along_Swath, Cell_Across_Swath]	Standard Deviation of Individual Pixel-Level Aerosol Optical Depth at 550 nm per Cell.
Deep_Blue_Algorithm_Flag_Land	[Cell_Along_Swath, Cell_Across_Swath]	Flag Indicating the Path Taken Through the Algorithm.
Deep_Blue_Aerosol_Optical_Depth_550_ Land_QA_Flag	[Cell_Along_Swath, Cell_Across_Swath]	Quality Assurance Flag for Aerosol Optical Depth at 550 nm.
Deep_Blue_Aerosol_Optical_Depth_550_ Land_Estimated_Uncertainty	[Cell_Along_Swath, Cell_Across_Swath]	Estimated Uncertainty in Aerosol Optical Depth at 550 nm.
Deep_Blue_Cloud_Fraction_Land	[Cell_Along_Swath, Cell_Across_Swath]	Fraction of Pixels per Cell Where Retrieval was not Attempted.
Deep_Blue_Number_Pixels_Used_550_ Land	[Cell_Along_Swath, Cell_Across_Swath]	Number of Aerosol Property Retrievals Performed per Cell.
Deep_Blue_Spectral_Aerosol_Optical_ Depth_Land	[Num_DeepBlue_Wavelengths, Cell_Along_Swath, Cell_Across_Swath]	Retrieved Aerosol Optical Depth Over Land at 412, 470, and 650 nm.
Deep_Blue_Spectral_Single_Scattering_ Albedo_Land	[Num_DeepBlue_Wavelengths, Cell_Along_Swath, Cell_Across_Swath]	Single-Scattering Albedo Over Land at 412, 470, and 650 nm.
Deep_Blue_Spectral_Surface_Reflectance_Land	[Num_DeepBlue_Wavelengths, Cell_Along_Swath, Cell_Across_Swath]	Surface Reflectance Used in Aerosol Retrieval Over Land for 412, 470, and 650 nm.
Deep_Blue_Spectral_TOA_Reflectance_ Land	[Num_DeepBlue_Wavelengths, Cell_Along_Swath, Cell_Across_Swath]	Top-of-Atmosphere Reflectance at 412, 470, and 650 nm.

[a]Cell_Along_Swath = number of cells in the along-track direction. Cell_Across_Swath = number of cells across the swath. Num_DeepBlue_Wavelengths = number of bands reported by the Deep Blue products, currently has a value of 3 (412, 470, and 650 nm).

July image captures the heavy smoke west of the Great Lakes, while the 18 July image follows the plume eastward ahead of a cloud front.

[45] Figure 18 compares the monthly mean Deep Blue AOT (Figures 18a–18d) and Ångström exponent (AE, Figures 18e–18h) for July and October 2008 using MODIS Aqua data with $QA = 2$ or 3 from C5 (left panels) with C6 (right panels). These monthly means are the averages of daily mean data. The monthly AE shown were weighted by the AOT on each day, such that they are more representative of the typical nature of the aerosol in a given grid cell over a month. This figure clearly shows that the spatial coverage of retrieved AOT has increased substantially from C5 to C6, due to the improved surface reflectance determination scheme used in C6. Aerosol information retrieved over extensive vegetation-covered areas are now included in

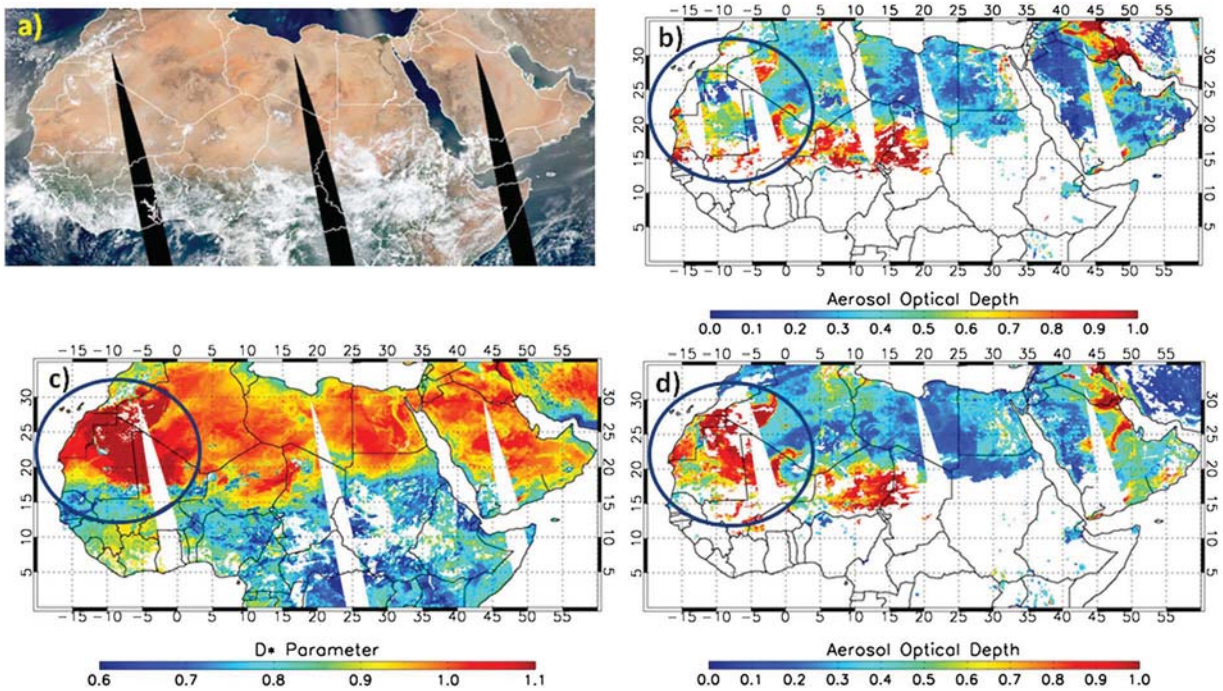

Figure 16. The effects of revised aerosol model selection scheme are shown by comparing the (b) MODIS Deep Blue C5 AOT with (d) MODIS Deep Blue C6 AOT for 9 July 2007. The circle indicates the area with most significant change in retrieved AOT as a result of this modification in C6 algorithm. The corresponding (a) MODIS Aqua true color image and (c) D* values are also displayed.

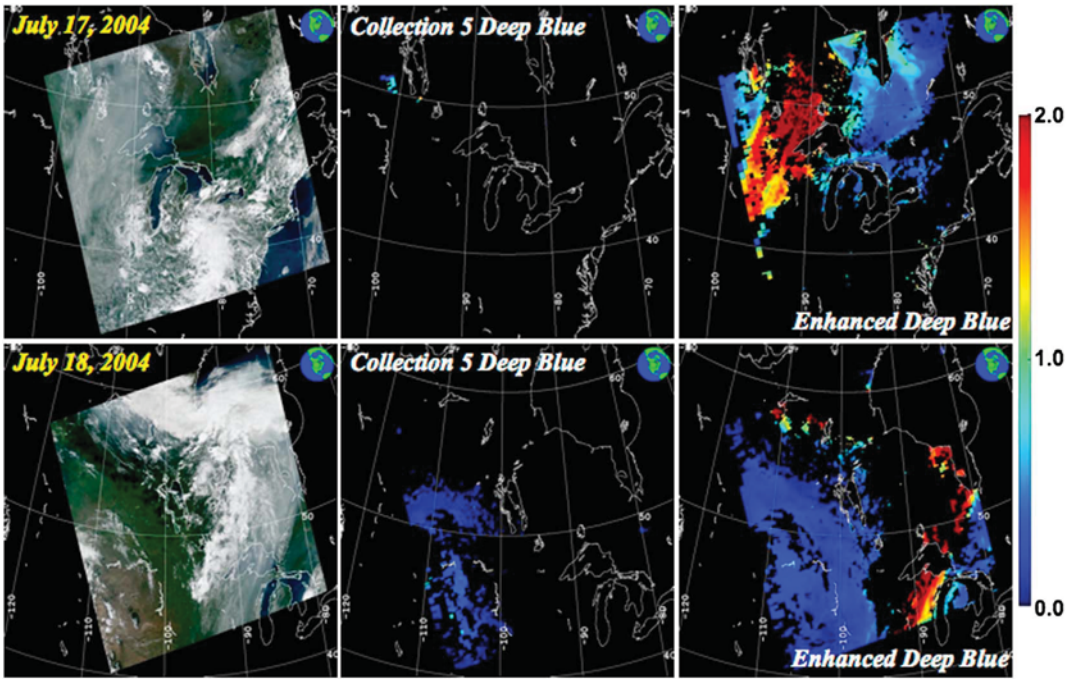

Figure 17. MODIS granule true color images (left column) and *Deep Blue* AOT at 0.550 μm from C5 (middle column) and C6 (enhanced *Deep Blue*) (right column) for smoke events over the Great Lakes area on 17–18 July 2004.

Deep Blue C6 data. For example, during July 2008, there were elevated AOT values observed in northern Canada. This was associated with biomass burning smoke generated from wildfires ignited by lightning under extreme dry heat and high wind conditions. At the same time, smoke plumes produced by forest fires in northeastern Russia spread over much of that region. Fine mode-dominated aerosol haze is also observed over eastern China. The AOT maps for October also reveal biomass burning activity in South America and central Africa, with high AOT values covering a large portion of these continents; this information could not have been obtained from the C5 Deep Blue data. These aerosol features are all associated with high AE values around 1.8.

[46] The spatial coverage of retrieval over urban/built-up and transitional zones is also much improved from C5 to C6. Since the previous C5 algorithm excluded any pixels with significant vegetation cover, and there are many large cities that have green vegetation inside the city zones, retrievals over such sites were scarce. By performing retrievals over both dark and bright surfaces inside the city limits, enough information is acquired to provide adequate quality for performing aerosol retrievals over these urban regions.

[47] The coverage over desert and semidesert regions is roughly the same between C5 and C6, as expected. However, due to the improved surface reflectance database and aerosol model selection scheme in C6, there are also significant differences in the monthly averaged AOT over these regions, such as higher AOT values in C6 than C5 over the western part of the Sahara and the southern part of Arabian Peninsula and lower values over Australia. Dust aerosols tend to have retrieved AE in the range 0–0.5. These dust, pollution, and biomass burning AE values are typical for aerosols of this type [e.g., *Eck et al*., 1999]; comparison with the C5 values again shows that C6 data are generally closer to expected values over much of the world.

[48] In order to study the effects of changes made in the C6 *QA* selection scheme, comparisons of the aerosol retrieval fraction (defined as ratio of number of days in the month with retrievals to total number of days in the month) with "all *QA*" and $QA = 3$ between C5 and C6 for the month of July 2008 are depicted in Figure 19. As expected, for all *QA*, the retrieval fractions are in general the same between C5 and C6 for desert regions but significantly improved from C5 to C6 over vegetated and urban/built-up regions. For $QA = 3$, the retrieval fractions are substantially improved from C5 to C6 almost everywhere, even over dry regions such as the Sahara/Sahel and the Arabian Peninsula, as a result of the *QA* selection changes in C6 described in section 2.4.

[49] Extensive comparisons of the new Deep Blue data sets with other satellite data will be the subject of future analyses, as the full MODIS C6 data set is not available at present. However, as a first view, Figure 20 presents comparisons between MODIS Deep Blue C6, SeaWiFS Deep Blue version 4, and MODIS Dark Target C5 [*Levy et al*., 2007] for the month of October 2008. Final C6 Dark Target data are not yet available at the time of writing; C5 Dark Target data are used instead as this data set's strengths and limitations are fairly well-known [*Levy et al*., 2010]. To mitigate the effects of aerosol spatiotemporal variability (although these cannot be removed entirely), data are collocated on a daily basis and the monthly composites in each case are created only from those days where both data sets in question provides data in a given grid cell. Thus, for example, the MODIS Deep Blue coverage in Figures 20a (comparison with SeaWiFS) and 20d (comparison with Dark Target) are different.

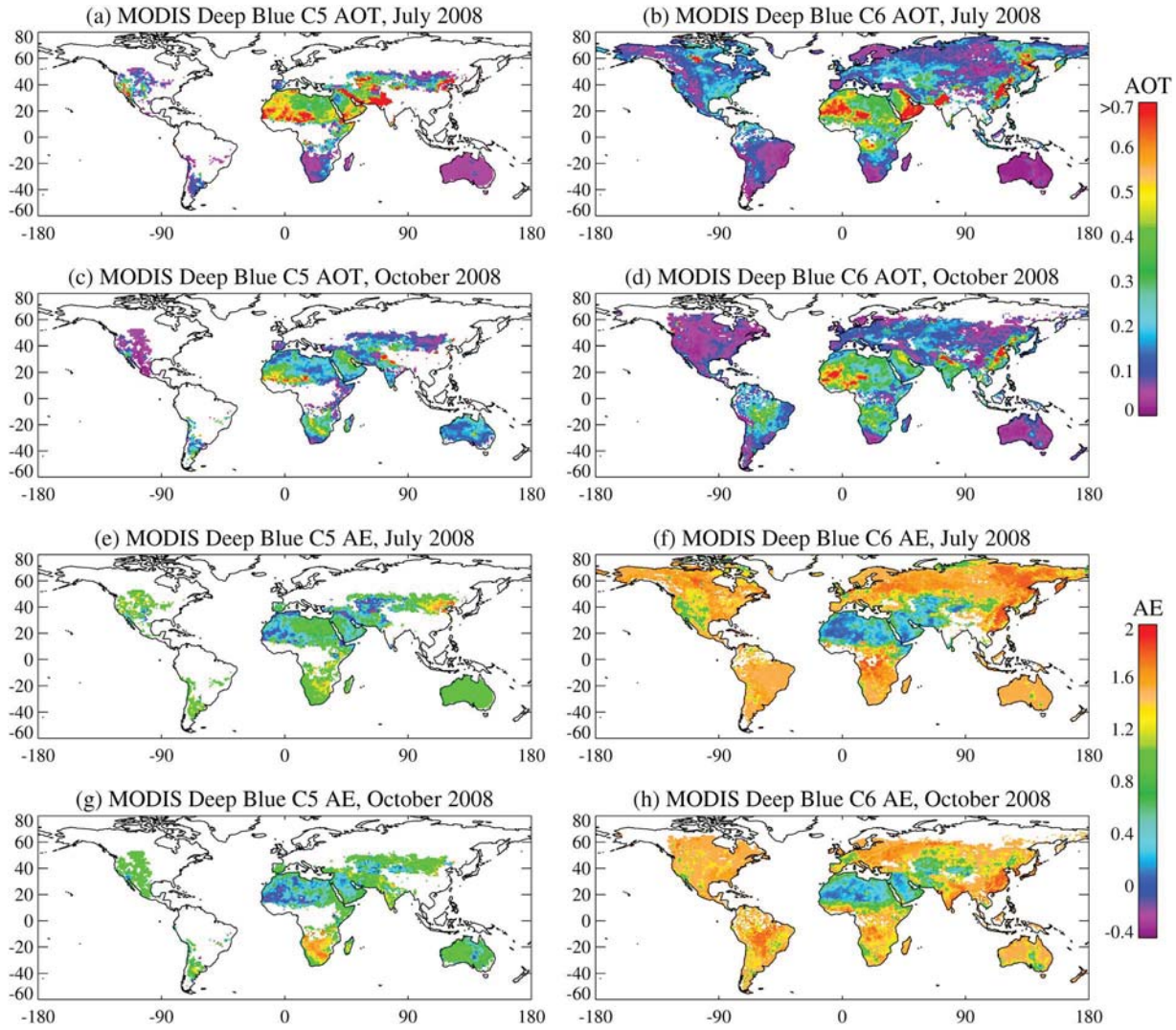

Figure 18. Comparisons of monthly averaged AOT at 0.55 μm and AE between MODIS Aqua C5 and C6 for July and October 2008. To alleviate the effect of sampling issue over the cloudy regions in the monthly mean, only data with better *QA* (2 or 3) flag are included in the analysis.

[50] Global AOT patterns are similar from all three data sets, and AOT differences in the monthly mean are in most cases smaller than 0.1. The two Deep Blue data sets retrieve lower AOT than Dark Target by 0.1–0.2 over many barren elevated regions (e.g., mountains in central Asia and the western Americas), although the Dark Target algorithm is known to be biased high in these areas [*Levy et al*., 2010]. MODIS Deep Blue is also lower than MODIS Dark Target in the Amazon; Dark Target is also known to be biased high here. Interestingly, the difference between SeaWiFS and MODIS Dark Target in the Amazon is smaller. The areas of largest difference between Deep Blue applied to MODIS and SeaWiFS in this month are in the eastern Arabian Peninsula, near the Pakistan/India border, and eastern Australasia (all dust cases over bright surfaces), and southern America (mixture of urban pollution and transported smoke). The MODIS data set is lower in all these cases. Combined with the aforementioned differences in the Amazon, this may suggest that SeaWiFS has a more limited ability to identify clouds in mixed cloud/smoke scenes, likely due to its more limited spatial resolution as well as wavelength coverage. These aspects will be assessed in more detail once the full Collection 6 data sets are available.

4. Preliminary Comparisons With AERONET AOT Measurements

[51] Extensive global and regional validation of the new SeaWiFS and MODIS Deep Blue aerosol data sets has been performed by *Sayer et al*. [2012a, 2013]. Here some brief results are shown for MODIS (Aqua) to illustrate the significant improvements of C6 over C5. This analysis uses data from 10 long-term AERONET sites at which both C5 and C6 provide retrievals (Agoufou, Banizoumbou, Beijing, Boulder, Fresno, Hamim, Kanpur, Mongu, Solar Village, Tinga Tingana); AERONET and MODIS data are spatiotemporally matched by averaging MODIS retrievals with $QA = 3$ within 25 km of each AERONET site and AERONET data (interpolated spectrally to 0.55 μm) within 30 min of the MODIS overpass [*Sayer et al*., 2013].

[52] Scatter density plots of the matched data are shown in Figure 21. Although a good level of agreement is found for

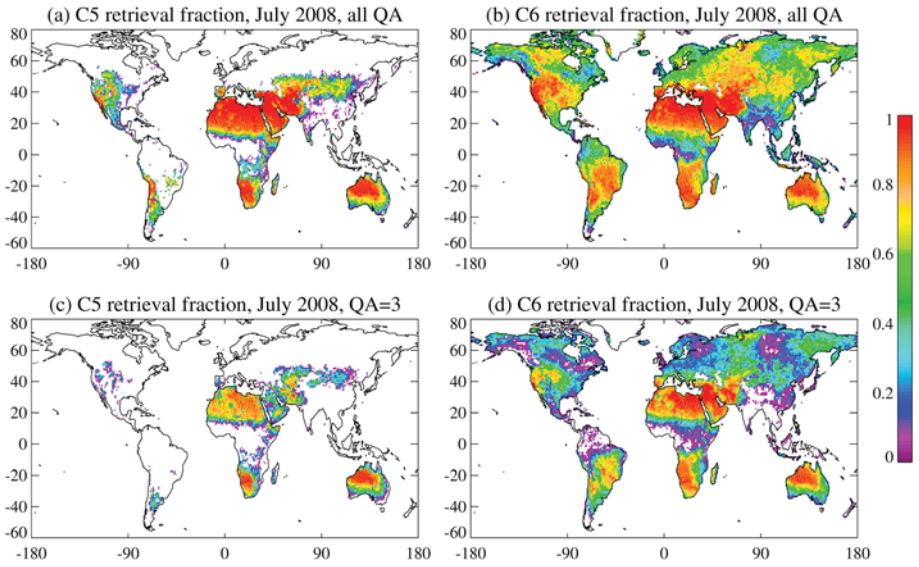

Figure 19. (a–d) Comparisons of monthly averaged aerosol retrieval fractions between MODIS Aqua C5 and C6 for July 2008 using data with all *QA* (top panel) and only *QA* = 3 (bottom panel). The white color represents region with zero retrieval fraction.

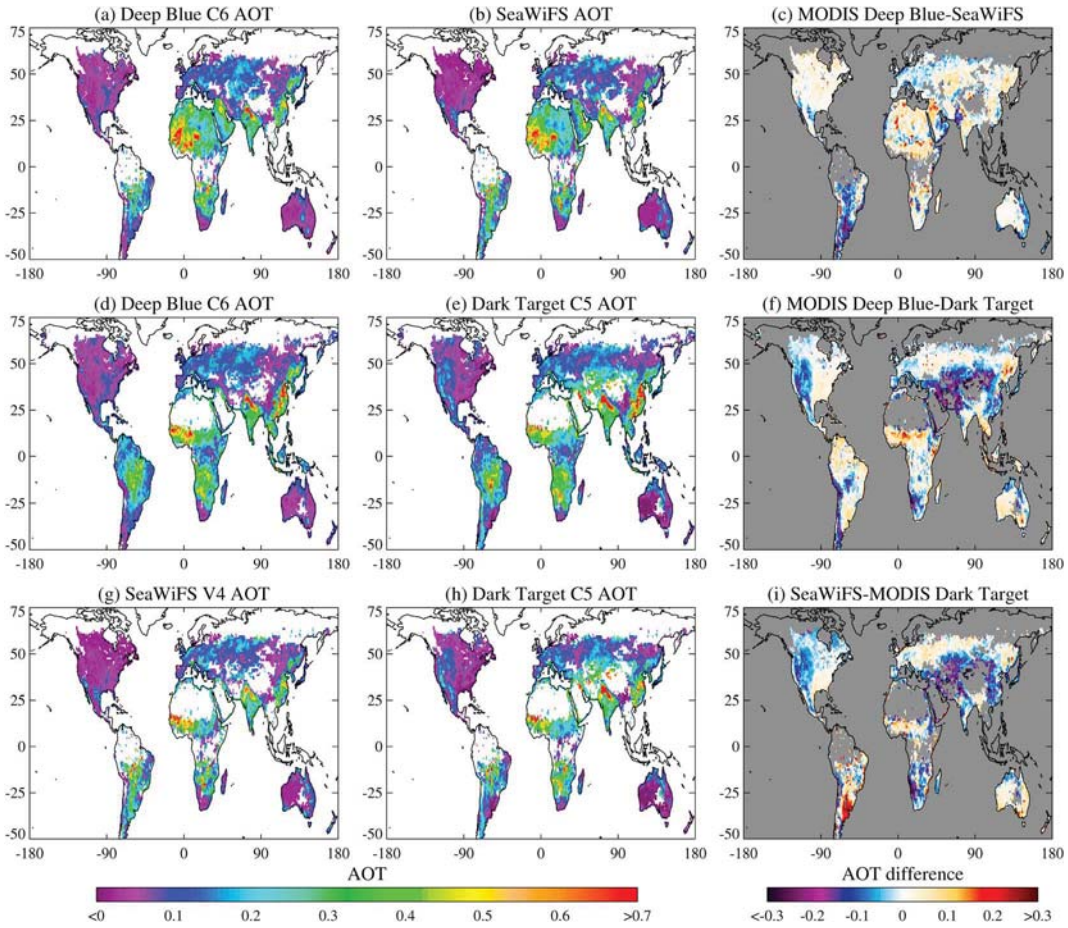

Figure 20. Comparison between monthly averaged AOT for (a, d) MODIS Deep Blue, (e, h) MODIS Dark Target, and (b, g) SeaWiFS Deep Blue data for October 2008. Each monthly composite is created by collocating the pair of data sets on a daily basis and then averaging. (c, f, i) Differences in the monthly means.

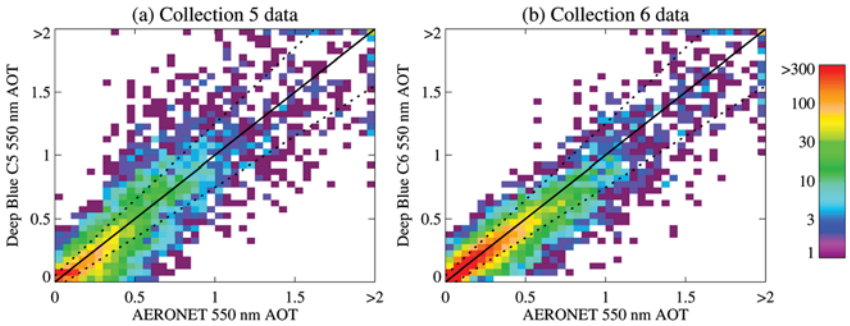

Figure 21. Scatter density plots of AERONET and MODIS Deep Blue AOT at 0.550 μm for (a) C5 and (b) C6, for 10 AERONET sites for which both Collections provide retrievals. The 1:1 line is shown in solid black; dotted lines indicate ± (0.05 + 20%) of the AERONET AOT.

both C5 and C6 data, performance is notably better for C6, with the number of extreme outliers reduced and a tighter clustering of points around the 1:1 line. Specifically, there are improvements in the correlation with AERONET (0.86 in C5, 0.93 in C6), median bias (−0.015 in C5, −0.008 in C6), root-mean-square error (0.22 in C5, 0.14 in C6), and proportion of retrievals agreeing within 0.05 + 20% of the AERONET AOT (62% in C5, 79% in C6). Additionally, the data volume for these 10 sites has nearly doubled (6335 matchups for C5, 11,234 for C6). These results show that the C6 data represent a large improvement on C5 both in terms of extent of coverage of $QA = 3$ retrievals, as well as the level of uncertainty of those retrievals. As C5 did not provide retrievals over vegetated surfaces, it is not possible to provide a comparative benchmark of this type in a more global sense; however, the analyses of *Sayer et al*. [2012a, 2013] show a similar high quality of performance of the Deep Blue algorithm over vegetated areas.

5. Conclusions

[53] A goal of the MODIS periodic reprocessing strategy is to provide self-consistent (i.e., no algorithmic discontinuities through the record) geophysical data sets, leveraging the increased understanding of the sensors and their calibration as well as the Earth's physical processes made between the reprocessings. The Deep Blue aerosol retrieval algorithm achieves this goal through the many modifications in MODIS C6 that are based on the latest knowledge of aerosol remote sensing. The most significant changes in C6 when compared to C5 include (1) an improved cloud screening scheme to maximize the aerosol retrieval frequency with minimal cloud contamination, (2) the use of a newly developed NDVI-dependent MODIS surface reflectance database to replace the previous static surface lookup tables, (3) a better dust aerosol model selection scheme using visible and thermal infrared bands simultaneously, and (4) revised quality flag selection procedures. In particular, the dynamic surface reflectance determination permits expansion of the spatial coverage of the Deep Blue aerosol products from only the bright-reflecting surfaces (such as deserts, semideserts, and nonvegetated urban areas) to all snow-free land surfaces, including vegetated areas. Consequently, the aerosol retrievals have been significantly improved in C6 over regions with mixed vegetated and nonvegetated surfaces such as urban areas, providing useful information for the study of air quality over large cities. In addition to MODIS C6, this enhanced algorithm has also been applied to SeaWiFS measurements, in combination with an over-ocean aerosol retrieval algorithm, to create a 13 year (1997–2010) data set of global aerosol products over land and ocean from that sensor; this data set is available from http://disc.gsfc.nasa.gov/dust.

[54] In this paper, we have demonstrated that the overall performance of the retrieved Deep Blue aerosol properties for MODIS C6 has improved when compared to C5. Based upon the preliminary validation of results from the enhanced Deep Blue algorithm using measurements from 10 selected long-term AERONET sites, the estimated error for the new C6 Deep Blue products is better than 0.05 + 20%, with 79% (compared to 62% in C5) of the best quality AOT ($QA = 3$) data falling within this range. The number of AOT retrievals with $QA = 3$ has also nearly doubled from C5 to C6. More extensive and detailed comparisons of the Deep Blue products with AERONET and other satellite products are provided for MODIS C6 and SeaWiFS V3 in *Sayer et al*. [2013] and *Sayer et al*. [2012a], respectively.

[55] Finally, in order to achieve a consistent long-term aerosol time series, this new enhanced Deep Blue algorithm has also recently been applied to the VIIRS sensor onboard the Suomi NPP satellite launched in October 2011. With the aging of the MODIS sensors, in particular Terra/MODIS, accurate radiometric calibration at the blue bands is becoming a challenging task. The use of a consistent satellite retrieval algorithm will make it easier to examine the effect of sensor calibration on the retrieved AOT by intercomparing aerosol products between MODIS, SeaWiFS, and VIIRS during their overlapping years; this, in turn, will result in a better quantitative determination of aerosol long-term trend on a global scale.

[56] **Acknowledgments.** This work was supported by the NASA EOS program, managed by Hal Maring. The authors gratefully acknowledge the MODIS Characterization Support Team for their extensive efforts in maintaining the high radiometric quality of MODIS level 1 data. Appreciations also extend to Jeremy Warner and Rebecca Limbacher for their supports on the construction of the Deep Blue surface database. We would also like to express our gratitude to several AERONET PIs in establishing and maintaining the long-term stations used in this investigation.

References

Bauer, S. E., and S. Menon (2012), Aerosol direct, indirect, semidirect, and surface albedo effects from sector contributions based on the IPCC AR5 emissions for preindustrial and present-day conditions, *J. Geophys. Res.*, *117*, D01206, doi:10.1029/2011JD016816.

Breitkreuz, H., M. Schroedter-Homscheidt, T. Holzer-Popp, and S. Dech (2009), Short-range direct and diffuse irradiance forecasts for solar energy applications based on aerosol chemical transport and numerical weather modeling, *J. Appl. Meteorol. Climatol.*, *48*, 1766–1779, doi:10.1175/2009JAMC2090.1.

Dave, J. V. (1972), Development of Programs for Computing Characteristics of Ultraviolet Radiation, *Tech. Rep.*, Vector Case, IBM Corp, Fed. Syst. Div, Gaithersburg, MD.

Deuzé, J. L., et al. (2001), Remote sensing of aerosols over land surfaces from POLDER-ADEOS-1 polarized measurements, *J. Geophys. Res.*, *106*(D5), 4913–4926, doi:10.1029/2000JD900364.

Eck, T. F., B. N. Holben, J. S. Reid, O. Dubovik, A. Smirnov, N. T. O'Neill, I. Slutsker, and S. Kinne (1999), Wavelength dependence of the optical depth of biomass burning, urban, and desert dust aerosols, *J. Geophys. Res.*, *104*(D24), 31,333–31,349, doi:10.1029/1999JD900923.

Franz, B. A., E. J. Kwiatkowska, G. Meister, and C. McClain (2008), Moderate Resolution Imaging Spectroradiometer on Terra: Limitations for ocean color applications, *J. Appl. Rem. Sens.*, *2*, 023525.

Friedl, M. A., et al. (2002), Global land cover mapping from MODIS: Algorithms and early results, *Remote Sens. Environ.*, *83*, 287–302.

Hall, D. K., G. A. Riggs, and V. V. Salomonson (1995), Development of methods for mapping global snow cover using Moderate Resolution Imaging Spectroradiometer (MODIS) data, *Remote Sens. Environ.*, *54*, 127–140.

Hansell, R. A., S. C. Ou, K. N. Liou, J. K. Roskovensky, S. C. Tsay, C. Hsu, and Q. Ji (2007), Simultaneous detection/separation of mineral dust and cirrus clouds using MODIS thermal infrared window data, *Geophys. Res. Lett.*, *34*, L11808, doi:10.1029/2007GL029388.

Hasekamp, O. P., and J. Landgraf (2007), Retrieval of aerosol properties over land surfaces: Capabilities of multi-viewing-angle intensity and polarization measurements, *Appl. Opt.*, *46*(16), 3332–3344, doi:10.1364/AO.46.003332.

Holben, B. N., et al. (1998), AERONET—A federated instrument network and data archive for aerosol characterization, *Remote Sens. Environ.*, *66*, 1–16.

Hsu, N. C., S. C. Tsay, M. D. King, and J. R. Herman (2004), Aerosol properties over bright-reflecting source regions, *IEEE Trans. Geosci. Remote Sens.*, *42*, 557–569.

Hsu, N. C., S. C. Tsay, M. D. King, and J. R. Herman (2006), Deep blue retrievals of Asian aerosol properties during ACE-Asia, *IEEE Trans. Geosci. Remote Sens*, *44*, 3180–3195.

Huang, J., N. C. Hsu, S.-C. Tsay, M.-J. Jeong, B. N. Holben, T. A. Berkoff, and E. J. Welton (2011), Susceptibility of aerosol optical thickness retrievals to cirrus contamination during the BASE-ASIA campaign, *J. Geophys. Res.*, *116*, D08214, doi:10.1029/2010JD014910.

IPCC (2007), Climate Change 2007: The Physical Science Basis, *Contribution of Working Group I to the Fourth Assessment Report of the Intergovernmental Panel on Climate Change*, edited by S. Solomon et al., Cambridge University Press, Cambridge, United Kingdom and New York, NY, USA.

Jeong, M.-J., Z. Li, D. A. Chu, and S.-C. Tsay (2005), Quality and compatibility analyses of global aerosol products derived from the advanced very high resolution radiometer and moderate resolution imaging spectroradiometer, *J. Geophys. Res.*, *110*, D10S09, doi:10.1029/2004JD004648.

Jeong, M.-J., N. C. Hsu, E. J. Kwiatkowska, B. A. Franz, and G. Meister (2011), Impacts of cross-platform vicarious calibration on the deep blue aerosol retrievals for Moderate Resolution Imaging Spectroradiometer aboard Terra, *IEEE Trans. Geosci. Remote Sens*, doi:10.1109/TGRS.2011.2153205.

Kaufman, Y. J., A. Wald, L. A. Remer, B. C. Gao, R. R. Li, and L. Flynn (1997), The MODIS 2.1-μm channel—Correlation with visible reflectance for use in remote sensing of aerosol, *IEEE. Trans. Geosci. Remote Sens.*, *35*(5), 1286–1298.

Knobelspiesse, K., B. Cairns, M. Mishchenko, J. Chowdhary, K. Tsigaridis, B. van Diedenhoven, W. Martin, M. Ottaviani, and M. Alexandrov (2012), Analysis of fine-mode aerosol retrieval capabilities by different passive remote sensing instrument designs, *Opt. Express*, *20*, 21,457–21,484, doi:10.1364/OE.20.021457.

Kwiatkowska, E. J., B. A. Franz, G. Meister, C. McClain, and X. Xiong (2008), Cross-calibration of ocean-color bands from Moderate Resolution Imaging Spectroradiometer on Terra platform, *Appl. Opt.*, *47*, 6796–6810.

Levy, R. C., L. A. Remer, S. Mattoo, E. F. Vermote, and Y. J. Kaufman (2007), Second-generation operational algorithm: Retrieval of aerosol properties over land from inversion of Moderate Resolution Imaging Spectroradiometer spectral reflectance, *J. Geophys. Res.*, *112*, D13211, doi:10.1029/2006JD007811.

Levy, R. C., L. A. Remer, R. G. Kleidman, S. Mattoo, C. Ichoku, R. Kahn, and T. F. Eck (2010), Global evaluation of the Collection 5 MODIS dark-target aerosol products over land, *Atmos. Chem. Phys.*, *10*, 10,399–10,420, doi:10.5194/acp-10-10399-2010.

Lohmann, U., and J. Feichter (2005), Global indirect aerosol effects: A review, *Atmos. Chem. Phys.*, *5*, 715–737, doi:10.5194/acp-5-715-2005.

Lyapustin, A., Y. Wang, I. Laszlo, R. Kahn, S. Korkin, L. Remer, R. Levy, and J. S. Reid (2011), Multiangle implementation of atmospheric correction (MAIAC): 2. Aerosol algorithm, *J. Geophys. Res.*, *116*, D03211, doi:10.1029/2010JD014986.

Martonchik, J. V., R. A. Kahn, and D. J. Diner (2009), Retrieval of aerosol properties over land using MISR observations, in *Aerosol Remote Sensing Over Land*, edited by A. Kokhanovsky and G. de Leeuw, pp. 267–293, Springer, Berlin.

Meister, G., E. J. Kwiatkowska, B. A. Franz, F. S. Patt, G. C. Feldman, and C. R. McClain (2005), Moderate-Resolution Imaging Spectroradiometer ocean color polarization correction, *Appl. Opt.*, *44*, 5,524–5,535.

Meskhidze, N., W. L. Chameides, and A. Nenes (2005), Dust and pollution: A recipe for enhanced ocean fertilization?, *J. Geophys. Res.*, *110*, D03301, doi:10.1029/2004JD005082.

Mi, W., Z. Li, X. Xia, B. Holben, R. Levy, F. Zhao, H. Chen, and M. Cribb (2007), Evaluation of the Moderate Resolution Imaging Spectroradiometer aerosol products at two aerosol robotic network stations in China, *J. Geophys. Res.*, *112*, D22S08, doi:10.1029/2007JD008474.

Mishchenko, M. I., A. A. Lacis, and L. D. Travis (1994), Errors induced by the neglect of polarization in radiance calculations for Rayleigh-scattering atmospheres, *J. Quant. Spectrosc. Radiat. Transfer*, *51*, 491–510.

Omar, A. H., et al. (2009), The CALIPSO Automated Aerosol Classification and Lidar Ratio Selection Algorithm, *J. Atmos. Oceanic Technol.*, *26*, 1994–2014, doi:10.1175/2009JTECHA1231.1.

Pope, C. A., III (2000), Epidemiology of fine particulate air pollution and human health: Biologic mechanisms and who's at risk?, *Environ. Health Perspect.*, *108*, 713–723.

Remer, L. A., et al. (2008), Global aerosol climatology from the MODIS satellite sensors, *J. Geophys. Res.*, *113*, D14S07, doi:10.1029/2007JD009661.

Sayer, A. M., N. C. Hsu, C. Bettenhausen, M.-J. Jeong, B. N. Holben, and J. Zhang (2012a), Global and regional evaluation of over-land spectral aerosol optical depth retrievals from SeaWiFS, *Atmos. Meas. Tech.*, *5*, 1761–1778, doi:10.5194/amt-5-1761-2012.

Sayer, A. M., G. E. Thomas, R. G. Grainger, E. Carboni, C. Poulsen, and R. Siddans (2012b), Use of MODIS-derived surface reflectance data in the ORAC-AATSR aerosol retrieval algorithm: Impact of differences between sensor spectral response functions, *Rem. Sens. Environ*, *116*, 177–188, doi:10.1016/j.rse.2011.02.029.

Sayer, A. M., N. C. Hsu, C. Bettenhausen, and M.-J. Jeong (2013), Validation and uncertainty estimates for MODIS Collection 6 "Deep Blue" aerosol data, *J. Geophys. Res. Atmos.*, *118*, 7864–7872, doi:10.1002/jgrd.50600.

Stevens, B., and G. Feingold (2009), Untangling aerosol effects on clouds and precipitation in a buffered system, *Nature*, *461*, 607–613, doi:10.1038/nature08281.

Wilcox, E. M. (2012), Direct and semi-direct radiative forcing of smoke aerosols over clouds, *Atmos. Chem. Phys.*, *12*, 139–149, doi:10.5194/acp-12-139-2012.

Enhanced Deep Blue Aerosol Retrieval Algorithm: the 2nd Generation

N. C. Hsu[1], M.-J. Jeong[2], C. Bettenhausen[1, 3], A. M. Sayer[1,4], R. Hansell[1, 5], C. S. Seftor[1, 3], J. Huang[5, 6], and S.-C. Tsay[1]

[1]NASA Goddard Space Flight Center, Greenbelt, MD, USA.
[2]Gangneung-Wonju National University, Gangneung City, Gangwong Province, Korea.
[3]Science Systems and Applications, Inc., Lanham, MD, USA.
[4]Goddard Earth Sciences Technology and Research (GESTAR), Universities Space Research Association, MD, USA
[5]Earth System Science Interdisciplinary Center, UMD, College Park, MD, USA
[6]NOAA NESDIS Center for Satellite Applications and Research, College Park, MD

*Corresponding author: N. C. Hsu, NASA Goddard Space Flight Center, Greenbelt, MD, USA. (Christina.Hsu@nasa.gov).

Abstract.

The aerosol products retrieved using the MODIS collection 5.1 Deep Blue algorithm have provided useful information about aerosol properties over bright-reflecting land surfaces, such as desert, semi-arid, and urban regions. However, many components of the C5.1 retrieval algorithm needed to be improved; for example, the use of a static surface database to estimate surface reflectances. This is particularly important over regions of mixed vegetated and non-vegetated surfaces, which may undergo strong seasonal changes in land cover. In order to address this issue, we develop a hybrid approach, which takes advantage of the combination of pre-calculated surface reflectance database and normalized difference vegetation index in determining the surface reflectance for aerosol retrievals. As a result, the spatial coverage of aerosol data generated by the enhanced Deep Blue algorithm has been extended from the arid and semi-arid regions to the entire land areas.

In this paper, the changes made in the enhanced Deep Blue algorithm regarding the surface reflectance estimation and other key schemes for producing the MODIS collection 6 aerosol products are discussed. A similar approach has also been applied to the algorithm that generates the SeaWiFS Deep Blue products. Based upon our preliminary results of comparing the enhanced Deep Blue aerosol products with the AERONET measurements, the expected error of the Deep Blue AOD is estimated to be better than 0.05 + 20%. Using 10 AERONET sites with long-term time series, 79% of the best-quality Deep Blue AOD values are found to fall within this expected error.

1. Introduction

The impact of natural and anthropogenic sources of air pollution has gained increasing attention from scientific communities in recent years. Indeed, tropospheric aerosols not only perturb the radiative energy balance by interacting with solar and terrestrial radiation, but also by changing cloud properties and lifetime. Houghton et al. (1990) showed that the aerosol forcing of climate is comparable in magnitude to the forcing caused by current anthropogenic greenhouse gases but opposite in sign. The Intergovernmental Panel on Climate Change (IPCC) estimated that the global-mean direct forcing due to anthropogenic aerosols is -0.5 ±0.4 Wm-2 (IPCC 2007), while Hansen and Lacis (1990) reported that the calculated forcing due to anthropogenic greenhouse gases is about 2.3±0.25 Wm-2. These results suggest that the aerosol cooling effect may have partially counteracted the warming contributed by greenhouse gas increases over the past few decades. In addition to radiative effects on climate, knowledge of the atmospheric aerosol burden is of interest for topics including effects on air quality and human health (Pope, 2000), mineral transportation and fertilization of distant ecosystems (Meskhidze et al., 2005), and effects on solar power yield (Breikreutz et al., 2009), among others.

The retrieval of aerosol properties from satellite measurements with sufficient accuracy for use in climate studies is a highly challenging task; it is an ill-posed problem where there are more unknowns about the microphysical and optical properties of aerosols than the information content that can be measured by current satellite sensors (e.g. Hasekamp and Landgraf, 2007; Knobelspiesse et al., 2012). For single-view satellite sensors such as the Advanced Very High Resolution Radiometer (AVHRR), Sea-viewing Wide Field-of-view Sensor (SeaWiFS), Moderate Resolution Imaging Spectrometer (MODIS), and Visible Infrared Imaging Radiometer Suite (VIIRS), the most important factors/components that could substantially impact the

71 performance of aerosol retrievals involve: 1) surface reflectance determination, including both
72 their spectral and angular dependencies; 2) aerosol microphysical model selection; 3) cloud
73 screening; and 4) identification of snow/ice-covered surfaces, particularly over seasons where
74 melting occurs. While the main driver of aerosol retrieval performance is largely determined by
75 adequate representation of aerosol microphysical properties in conditions of high aerosol loading
76 [Jeong et al., 2005], accurate characterization of surface reflectance is the main driver for low
77 aerosol loadings [Mi et al., 2007]. Since the aerosol loading ranges from low to moderate over
78 most of the world [e.g. Remer et al., 2008], surface reflectance determination remains one of the
79 most important inputs to aerosol remote sensing from space, especially over land.

80 Due to the brightness of land surfaces, aerosol retrieval over land is a much more intricate
81 task compared to retrieval over ocean. In particular, the top-of-atmosphere (TOA) reflectances
82 acquired by the satellite sensors at red and near-infrared wavelengths, available from most
83 heritage sensors, are overwhelmed by the surface contributions over desert and semi-desert
84 regions, making it difficult to separate the contribution of aerosols to the TOA signal from that of
85 the surface. As a result, previous satellite aerosol retrieval algorithms from these single view
86 sensors, such as the operational SeaWiFS, AVHRR, and MODIS ones that rely on the Dark-
87 Target approach [Kaufman et al., 1997; Levy et al., 2007], were unable to provide aerosol
88 properties over such bright-reflecting regions. It is worth noting that multi-angular, polarization,
89 or active (lidar) measurements provide extra constraints on the retrieval system and do enable
90 retrieval of aerosol properties over these bright surfaces with reasonable accuracy [e.g. Deuzé et
91 al, 2001, Martonchik et al., 2009, Omar et al., 2009, Lyapustin et al., 2011, Sayer et al., 2012b];
92 however, existing sensors and algorithms with these capabilities typically have comparatively

93 narrow swath widths, shorter data records, and/or require temporal compositing of data, thus
94 making them less suitable for some applications.

95 The development of the Deep Blue algorithm narrowed these gaps in SeaWiFS and
96 MODIS aerosol products by performing retrievals over these surfaces. The Deep Blue algorithm
97 utilizes blue-wavelength measurements from instruments such as SeaWiFS and MODIS, where
98 the surface reflectance over land is much lower than for longer wavelength channels, to infer the
99 properties of aerosols [Hsu et al., 2004, 2006]. Using MODIS reflectance data, the Deep Blue
100 technique successfully produced a suite of aerosol products, including aerosol optical thickness,
101 Ångström exponent, and dust absorption over desert and semi-desert areas and urban regions,
102 that are an integral part of the operational MODIS collection 5.1 (C5) MOD04 and MYD04
103 aerosol products for Terra and Aqua, respectively.

104 Although successful, many of the approximations and assumptions utilized in the first
105 generation of the Deep Blue algorithm needed to be refined and improved to yield better
106 retrievals. One of the most important issues is improving the surface reflectance determination
107 scheme in the retrieval. In the MODIS C5 algorithm, the use of static surface databases limited
108 the algorithm's capability to retrieve aerosols over regions with seasonal vegetation changes,
109 such as in the Sahel and many urban sites. Also, the retrievals were only performed over bright-
110 reflecting surfaces, leading to insufficient information content for retrievals over regions with
111 mixed vegetated and non-vegetated surfaces. Therefore, in order to optimize estimates of surface
112 reflectance, extensive efforts have been made to develop the 2nd generation of the Deep Blue
113 algorithm, which adopts a hybrid approach to take advantage of both the surface reflectance
114 database method and a dynamical surface reflectance method.

115 In this paper, we will describe the improvements made to the surface reflectance
116 determination and many other schemes in the enhanced Deep Blue algorithm used for processing
117 the MODIS data to create collection 6 (C6) of the Deep Blue products, as well as the SeaWiFS
118 Version 3 products. Section 2 illustrates the methodology of this new algorithm, and detailed
119 changes made in each key component compared to the previous C5 algorithm. Section 3
120 summarizes the results of the aerosol products generated from the new algorithm. Finally, we
121 show provisional validation of the new Deep Blue C6 products in Section 4, followed by some
122 conclusions in Section 5.

123 2. Description of the Algorithm

124 To retrieve aerosol properties over land, we employ a polarized radiative transfer model
125 [Dave, 1972] to compute the reflected intensity field, which is defined by

126 $$R(\mu, \mu_0, \phi) = \frac{\pi I(\mu, \mu_0, \phi)}{\mu_0 F_0} \quad (1)$$

127 where R is the normalized radiance (or apparent reflectance), F_0 is the extra-terrestrial solar flux,
128 I is the radiance at the top of the atmosphere, μ is the cosine of the view zenith angle, μ_0 is the
129 cosine of the solar zenith angle, and ϕ is the relative azimuth angle between the direction of
130 propagation of scattered radiation and the incident solar direction. This radiative transfer code
131 includes full multiple scattering and takes into account polarization; in the blue wavelength range
132 of 0.412 to 0.49 μm, which is vital for this study, Rayleigh scattering is relatively important
133 compared to the longer wavelengths, and neglect of polarization in the radiative transfer code
134 would lead to significant errors in the calculated reflectances [Mishchenko et al., 1994].

Since the retrieval of aerosol properties from space-borne sensors requires highly accurate and precise radiometric measurements, sensor calibration and characterization are extremely critical before high quality long-term satellite aerosol data can be achieved for climate study. This is particularly important for Terra/MODIS, which has suffered from aging of the optics and detectors since its launch in 1999. In fact, the characteristics of the detectors of certain bands, especially band 8 (0.412 μm), have changed significantly over time, leading to increased calibration uncertainty. In order to address this issue, we have utilized a cross-calibration method developed for characterizing the Terra/MODIS detectors by the NASA Ocean Biology Processing Group [Meister et al., 2005, Franz et al., 2008, Kwiatkowska et al., 2008]. Both response versus scan angle (RVS) and polarization sensitivity corrections have been applied to the MODIS Level 1 reflectances at these blue bands, which are vital to the Deep Blue algorithm. This calibration correction was performed to Terra/MODIS C5 and resulted in substantial improvements in the quality of Deep Blue aerosol retrievals (see Jeong et al. [2011] for details). Similar procedures have been also applied to Terra/MODIS C6.

After performing necessary calibration corrections to the Level 1 reflectances, multiple bands (i.e., 0.412, 0.47, 0.65, 0.86, 1.24, 1.38, 2.11, 11, and 12 μm for MODIS) are ingested by the Deep Blue algorithm as inputs for the Level 2 aerosol product retrievals. An overview of the enhanced Deep Blue algorithm over land is provided in the data flow diagram shown in Figure 1. The fundamental steps of the processing stream used to account for different types of land surfaces are described as follows:

1) Scenes are screened for the presence of clouds by examining the spatial variation of the reflectances from the 0.412 μm channel, the brightness temperatures from 11 and 12 μm, and the 1.38 μm MODIS reflectances. As in the C5 algorithm, pixels are first tested for the presence

158 of clouds as well as snow/ice surfaces before the aerosol retrieval processing begins. The
159 retrieval is not performed for cloud- or snow/ice-contaminated pixels.

160 2) For a given pixel, the surface reflectances are determined for the 0.412, 0.47, and 0.65
161 μm channels using one of three different methods: i) by a dynamic surface reflectance approach;
162 ii) based upon its geolocation using a pre-calculated surface reflectance database created from
163 the MODIS or SeaWiFS measurements; or iii) a combination of the first two approaches. The
164 selection of which method is used depends on the TOA reflectance at shortwave-infrared or near-
165 infrared wavelengths (i.e., 2.1 μm for MODIS and 0.865 μm for SeaWiFS) and the normalized
166 difference vegetation index (NDVI), which is defined as

167 $$NDVI = (R0.86 - R0.65) / (R0.86 - R0.65)$$

168 where R0.65 and R0.86 correspond to the TOA reflectance measured at 0.65 μm and 0.86 μm,
169 respectively.

170 3) The 0.412, 0.47, and 0.65 μm TOA reflectances are then compared to reflectances
171 contained in look-up tables with dimensions consisting of the solar zenith, satellite (viewing)
172 zenith, and relative azimuth angles, and the surface reflectance, aerosol optical thickness, and
173 single scattering albedo. A maximum likelihood method is used to match the appropriate values
174 of aerosol optical thickness and mixing ratio to the measured reflectances. Reflectance data from
175 the 0.65 μm channel is used when the aerosol cloud is thick. For details of the algorithm see Hsu
176 et al. [2004, 2006].

177 Except for extremely blue-light absorbing dust, the basic procedures used for aerosol
178 model generation and selection in the enhanced Deep Blue algorithm are similar to the MODIS
179 C5 version. However, both cloud screening and surface reflectance determination have been

substantially changed to improve the accuracy of the retrieved aerosol properties. Details of the cloud screening scheme (in particular for cirrus) are described below, while the calculation of surface reflectances is discussed in section 2.2.

2.1 Cloud and snow/ice screening

There are several improvements made in the MODIS C6 Deep Blue algorithm regarding flagging procedures in the presence of clouds and snow/ice. The flowchart of detailed steps used in the cloud screening scheme is depicted in Figure 2. Previously, the C5 algorithm used a simple conservative filter based on the variability of TOA reflectance at 0.412 μm (R0.412) within a 3 x 3 pixel area. However, in order to sufficiently filter out cloudy pixels, pixels over areas of highly variable surface reflectance sometimes also got flagged as cloud-contaminated. In C6, new checks on brightness temperature (BT) at 11 μm (BT11) and the BT difference (BTD) between 11 μm and 12 μm (BTD11-12) have been implemented in addition to the R0.412 variability filter. By combining the thermal infrared channels with the blue channel, the contrast between clouds and the underlying surface becomes much more discernible, particularly over regions with high surface inhomogeneity. This allows us to relax the criteria for the 0.412 μm variability filter previously used in C5, and more pixels are subsequently retained for aerosol retrievals while still maintaining minimum contamination from clouds.

In addition, significant efforts have been made toward the identification of thin cirrus in C6. In the C5 Deep Blue algorithm, the use of a single threshold method based upon MODIS band 26 (i.e., 1.38 μm), although proven to be robust in general [Huang et al, 2011], led to pixels that were sometimes over-screened for cirrus. This was particularly true over moisture-deprived desert regions such as the Sahara; since this MODIS band is strongly sensitive to water vapor

absorption, a very low amount of column water vapor in the atmosphere (i.e., less than 5 mm in total precipitable water) could result in elevated values of TOA reflectance at 1.38 μm (R1.38) and thus a false detection of cirrus. Together with the aforementioned spatial variability test, the C6 improvements were found by Sayer et al. (2013) to treble the data volume in C6 relative to C5 for some areas.

One such example (for March 7, 2006) is shown in Figure 3. On this day, a significant gap in the C5 Deep Blue retrieved AOT (Fig. 3b) is seen over the Sahara around 20° N - 25° N and 0^0 - 10^0 E; this gap is triggered by the cirrus flag due to high values of R1.38 over this region. The corresponding MODIS RGB image does not seem to indicate the presence of cirrus over this region and the gap in AOT is, therefore, most likely due to the over-screening of cirrus under very dry atmospheric conditions (Fig. 3d).

In order to alleviate this problem, we implemented a scheme to jointly use R1.38, BT11, BTD11-12 and the total precipitation water (TPW) obtained from the National Centers for Environmental Prediction (NCEP) as part of the ancillary data input into the C6 algorithm. The use of BTD11-12 has been shown to effectively identify the presence of cirrus cloud [Hansell et al., 2007]. As seen in Fig. 3e, the regions covered by clouds including cirrus are generally associated with positive BTD11-12 values, consistent with the simulation results of Hansell et al. [2007].

In order to account for the coarse resolution (1° latitude x 1° longitude) of the NCEP TPW data and the effects of underlying surfaces on BTD11-12 near the edge of thin cirrus, different steps and thresholds are selected to achieve optimal cirrus screening for different surface types according to the reflectances of underlying surfaces at 0.65 μm based upon the pre-

224 calculated surface reflectance database. These steps and thresholds are shown in Fig. 2. As
225 shown in Fig. 3g, this improved scheme results in a substantial increase in the number of aerosol
226 retrievals in C6 from those areas that were previously over-screened in C5.

227 As shown in Fig 4, we also improved the identification of underlying snow/ice surfaces
228 in C6 by adapting the method described by Hall et al. [1995]. The value of Normalized
229 Difference Snow/Ice Index (NDSI) used in the C6 algorithm is defined as

230 $$NDSI = (R0.555 - R2.1) / (R0.555 + R2.1)$$

231 where R0.555 and R2.1 correspond to the TOA reflectance measured by MODIS at 0.555 μm
232 and 2.1 μm, respectively. We use the reflectance from 2.1 μm instead of the 1.6 μm channel used
233 by Hall because of a detector issue associated with this channel on MODIS/Aqua. Since the
234 snow albedo decreases dramatically from visible wavelengths to near infrared and shortwave
235 infrared, the spectral shape of snow/ice surface is opposite to that of snow-free land surfaces,
236 which allows us to separate snow/ice surfaces from other types of land. To achieve optimal
237 screening of the snow/ice contaminated pixels, the resulting NDSI values are also employed in
238 conjunction with R0.86 and R0.555 as well as BT11 to check their surface temperature and
239 reflectance for potential water and aerosol-laden pixels. In our C6 algorithm testing, this
240 snow/ice identification scheme was found to be particularly important in filtering out erroneous
241 pixels for aerosol retrievals at high latitudes in the Northern Hemisphere during the spring
242 snow/ice melting season.

243 2.2 Surface reflectance determination

244 To obtain high quality aerosol retrievals, an accurate determination of the underlying
245 surface reflectance is imperative. The surface reflectance used for aerosol retrievals in the

246 previous C5 algorithm was based upon a static pre-calculated database that was a function of
247 season. This approach provided reasonable performance over desert and semi-desert regions,
248 where the surface reflectances are relatively invariant with time and the effects of the surface
249 bidirectional reflectance distribution function (BRDF) are weaker than those over vegetated
250 areas. However, the surface reflectance database approach was sometimes found to be
251 unsuccessful over vegetated surfaces, especially where seasonal and inter-annual changes are
252 significant. To improve the estimate of surface reflectance in such cases, it is necessary to
253 instantaneously account for dynamic changes amongst diverse types of vegetation.

254 In order to address this issue, extensive efforts have been made in the enhanced Deep
255 Blue algorithm to improve the calculation of surface reflectance. As a result, three different
256 surface reflectance schemes, as depicted in Figure 1, have been adopted in MODIS C6 Deep
257 Blue to optimize retrievals of aerosol properties based upon different surface types. Specifically,
258 we use the MODIS Land Cover and Land Cover Dynamics product (MCD12C1) (Friedl et al.,
259 2002) to separate pixels into three categories: 1) arid and semi-arid regions, 2) general
260 vegetation, and 3) urban/built-up and transitional regions. The map of regions where these three
261 surface reflectance schemes have been applied is depicted in Figure 5. We also note that,
262 although different wavelength pairs are used for MODIS (0.412, 0.47, 0.65, and 2.1 μm) and for
263 SeaWiFS (0.412, 0.49, 0.67, and 0.87 μm), similar approaches have been applied for calculating
264 surface reflectances to both MODIS C6 and SeaWiFS version 3 (and later) Deep Blue products.
265 The details of surface reflectance calculation for each land category are described below.

266

267

268 2.2.1 Deep Blue surface database

269 For arid and semi-arid regions, the surface database method continues to be used in
270 MODIS C6 for determining the surface reflectance. However, several major changes were made
271 in constructing the database. Similar to what was used in C5, the C6 surface database was
272 compiled based upon the minimum reflectivity method at the resolution of 0.1° latitude x 0.1°
273 longitude for each season using MODIS TOA reflectances at 0.412, 0.47 and 0.65 μm (*cf.* Hsu et
274 al [2004] for details). In C6, better sample statistics have been achieved by increasing MODIS
275 TOA reflectance input data from the two years (2005-2006) previously used in C5 to more than
276 seven years (2002-2009). Additionally, in order to account for potential changes in land cover
277 type within the given season over the same location, the C6 surface database is not only a
278 function of season as in C5, but also of NDVI. The details of construction of the C6 surface
279 database are as follows.

280 First, to ensure only clear pixels are included in the analysis, the TOA reflectance pixels
281 at the three MODIS bands in the database were tested for clouds, as well as cloud edges and
282 thick aerosol plumes, by employing a conservative screening scheme based upon the standard
283 deviations of 0.412 μm TOA reflectances within a 3x3 pixel area centered on the pixel in
284 question. Also, to account for seasonal/transient inland water bodies, water pixels were filtered
285 out if the computed NDVI was negative. Reflectance values that pass these tests are corrected for
286 the contribution from molecular (Rayleigh) scattering, and averaged into a daily mean for the
287 given grid.

288 Next, these grid cells were divided into 4 separate groups according to their NDVI:
289 NDVI < 0.18, 0.18 <= NDVI < 0.24, NDVI >= 0.24, and an 'all NDVI' group. To further

alleviate the problem of outliers due to any remnant presence of cloud shadow or solar eclipse, one additional check was performed to screen out any pixels that lay outside the range of twice the standard deviation from the mean of the samples over every 10° angular bin collected for the given grid cell. Finally, the surface reflectance values in the C6 database are calculated by a 2nd order polynomial fit through the lowest 15 percentile of grid cell samples against the scattering angles over the given location. The scattering angle (Φ) is defined as:

$$\Phi = \cos^{-1}(- \cos\theta_0 \cos\theta + \sin\theta_0 \sin\theta \cos\phi)$$

where θ_0, θ, and ϕ are the solar zenith, sensor view zenith, and relative azimuth angles, respectively. These angular curve fittings of surface reflectance are performed for each NDVI group collected over the given grid cell, provided that a sufficient sample size (50 or more points) is acquired. The derived surface reflectance database therefore depends upon the scattering angle, NDVI, and season. One example of the procedure is provided in Figure 6 using MODIS data over Tinga Tingana, Australia (29° S, 140° E) for the fall season. It is apparent that, for this dry region, the derived surface reflectance at 0.65 μm (Fig. 6c) is not only substantially brighter than that at 0.412 μm (Fig. 6a), but its corresponding anisotropy is much larger (shown in the slope of resulting surface reflectance as a function of scattering angle). This is consistent with the expected characteristics of desert surfaces. We note that similar procedures have also been applied to the SeaWiFS data at 0.412, 0.49, and 0.67 μm for constructing the surface reflectance database at these wavelengths.

Figures 7 and 8 show the C6 global maps of surface reflectances at 0.412 and 0.65 μm constructed from our surface database, based upon more than seven years of MODIS Aqua data, for each season using the above approach for the 'all NDVI' group. In general, the surface

312 reflectance at 0.65 μm is higher than at 0.412 μm, particularly over dry regions, and exhibits a
313 much more discernible contrast between vegetation and desert areas. We note that there are still
314 gaps in the derived surface reflectance database due to the frequent presence of clouds or
315 snow/ice over certain parts of the world, such as the Amazon and equatorial Africa. As a result,
316 the sample size of data passing our conservative cloud screening scheme were insufficient for
317 computing surface reflectance polynomial fitting with rigorous statistics over such regions.
318 However, these regions are associated with vegetated land areas, which will not require the use
319 of this surface database to determine the surface reflectance in the C6 algorithm.

320 2.2.2 Vegetated land surfaces

321 Over vegetated land surfaces, we retrieve aerosol properties by taking advantage of the
322 spectral relationship in surface reflectance between visible and longer wavelengths (i.e., 0.87 μm
323 for SeaWiFS and 2.1 μm for MODIS) to account for the effect of the ever-changing dynamics of
324 vegetation phenology on the surface reflectance. However, in order to better determine the
325 spectral surface reflectance relationship, contributions from the atmosphere need to be removed
326 from the satellite-measured signals. This task was accomplished by collocating satellite
327 measurements from MODIS and SeaWiFS with ground-based Aerosol Robotic Network
328 (AERONET; Holben et al., [1998]) data. The satellite derived surface reflectances at visible
329 wavelengths (i.e., 0.47 and 0.65 μm for MODIS and 0.49 and 0.67 μm for SeaWiFS) were then
330 obtained using AERONET AOT and single scattering albedo information to perform an
331 atmospheric correction. Hereinafter, such derived surface reflectances based on the explicit
332 atmospheric corrections performed using collocated satellite measurements and AERONET data
333 will be referred to as “benchmark” surface reflectances. Since the uncertainty of deriving surface
334 reflectance increases significantly as aerosol loading becomes larger, we only include samples

335 for analysis when the AERONET AOT at 0.5 μm < 0.5. The correction procedure is described
336 below.

337 For MODIS data, our approach estimates the surface reflectances at visible channels
338 based upon the TOA reflectances at 2.1 μm (R2.1) and land cover type using the following
339 formulas:

340 $$ESR_{0.65} = a + b * R2.1 + c * (R2.1)^2 \quad (2)$$

341 $$ESR_{0.47} = d + e * ESR_{0.65} \quad (3)$$

342 where ESR is the estimated surface reflectance and a, b, c, d, and e are coefficients determined
343 by a least-squares fitting to the derived benchmark surface reflectance data over the AERONET
344 sites. The spectral surface reflectance relationships given by the above formulae can vary
345 depending upon the land cover type and season.

346 These spectral relationships for different surface types, based upon 2004 springtime
347 MODIS data over the United States, are depicted in Figure 9. It is apparent that the spectral
348 surface reflectance relationships for most naturally vegetated surfaces can be collapsed into a
349 single relationship, while the relationships for cropland (grey color) or for urban and built-up
350 regions (light blue color) deviate distinctively from those for naturally-vegetated surfaces. Based
351 on these findings, we derive the surface reflectance relationship separately for each land cover
352 type (i.e., naturally vegetated area and cropland) and seasons, with a consideration of the changes
353 of surface property for cropland by establishing sub-groups depending on the values of
354 $NDVI_{SWIR}$, which is defined as

355 $$NDVI_{SWIR} = (R1.24 - R2.1) / (R1.24 - R2.1)$$

We note that this approach is not applied to the urban/built-up zones, since the hybrid method is used in the enhanced Deep Blue algorithm over such regions.

An example of the derivations of spectral surface reflectance relationships for naturally vegetated surfaces during the March-April-May season is provided in the upper panels of Figure 10. The values of the coefficients for estimating the surface reflectances in equations 2 and 3 are determined by a 2^{nd} order polynomial least square curve fit through the data points. The resulting coefficients a – e in Eq. 2 and 3 for each season are tabulated in Tables 2 and 3 for naturally vegetated regions and croplands, respectively. To validate the fit, comparisons between these estimated surface reflectances at 0.47 and 0.65 μm and the corresponding benchmark surface reflectances were performed, and these comparisons are presented in the lower panels of Fig. 10. As shown in the figure, the estimated surface reflectances show reasonable agreement (root-mean-square error of 1.2% for 0.65 μm, 0.67% for 0.47 μm) with the benchmark surface reflectances.

For SeaWiFS aerosol retrievals over vegetated regions, the enhanced Deep Blue algorithm utilizes the 0.49, 0.67, and 0.865 μm bands to derive surface reflectances due to lack of the SWIR bands for SeaWiFS. Figure 11 shows that, for all the collocated SeaWiFS/AERONET data acquired over the continental US during spring 2004, the atmospherically corrected surface reflectances (i.e., benchmark surface reflectances) from SeaWiFS exhibit a linear relationship with the corresponding TOA reflectances at 0.865 μm (after the Rayleigh scattering contribution has been removed). Figure 11 also shows that this relationship is a function of NDVI. Based on these results, we developed an approach that estimates the surface reflectance at visible channels based upon the Rayleigh-corrected TOA reflectances at the NIR channel (i.e., 0.865 μm) and NDVI values using the following formulas:

$$ESR_{0.67} = RCR_{0.865} * (a*NDVI' + b) + c \quad (4)$$

$$ESR_{0.49} = RCR_{0.865} * (d*NDVI' + e) + f \quad (5)$$

where ESR and RCR are the estimated surface reflectance for the 0.67 and 0.49 μm bands and Rayleigh-corrected reflectances at 0.865 μm, respectively; a, b, c, d, e, and f are coefficients determined by least-squares fitting to the benchmark surface reflectances; and

$$NDVI' = (RCR_{0.865} - RCR_{0.67}) / (RCR_{0.865} + RCR_{0.67}) \quad (6)$$

The regression coefficients were derived seasonally and according to 3 NDVI' classes: 0.10 < NDVI' <= 0.20; 0.20 <NDVI' <= 0.55; NDVI' > 0.55. In addition, aerosol retrievals using this approach are only performed for pixels with a surface reflectance < 0.23 and an NDVI' > 0.1. The resulting coefficients for each NDVI' category and season are tabulated in Tables 4 and 5 for 0.67 and 0.49 μm SeaWiFS bands, respectively.

Comparisons of the SeaWiFS estimated surface reflectance at 0.49 μm using this approach exhibit reasonable agreement for all four seasons with the corresponding "benchmark" surface reflectance regardless of the AOT values. Examples of these comparisons for spring (March-April-May) and fall (September-October-November) are shown in the upper panels of Figure 12. The corresponding AOT value for each pixel is indicated by the color of the symbol. The satellite-estimated surface reflectances at 0.67 μm are seen to also correlate well with the benchmark surface reflectance shown in the lower panels of Figure 12, except for high AOT cases. This is likely due to the fact that the slopes of surface reflectance from 0.865 to 0.67 μm are more sensitive to the NDVI' values than the 0.865-to-0.49μm slopes shown in Fig. 11.

399 Therefore, bias in NDVI' due to the presence of aerosols has a stronger impact on retrieving the
400 surface reflectance at 0.67 μm than it does for 0.49 μm using this approach.

401 The dependence of the deviation between benchmark 0.49 and 0.67 μm surface
402 reflectance and satellite estimated values as a function of AOT at 0.49 μm from the AERONET
403 data is further investigated and plotted in Figures 13 a and b. We note that, while the surface
404 reflectance bias at 0.49 μm appears to be independent of AERONET AOT, there is a clear
405 correlation between the surface reflectance bias at 0.67 μm and AOT at 0.49 μm. To account for
406 this effect, the estimated surface reflectance at 0.67 μm was re-adjusted by using satellite
407 retrieved AOT at 0.49 μm in conjunction with the linear regression line indicated in Figure 13b
408 before it is used for aerosol retrievals at 0.67 μm.

409 As a result, the surface reflectance determination schemes for MODIS and SeaWiFS
410 described above are being applied to the naturally vegetated regions and cropland indicated by
411 the areas with green color in Fig. 5 for aerosol retrievals in the enhanced Deep Blue algorithm.
412 For the urban/built-up and transitional zones, the surface reflectances at visible wavelengths do
413 not have simple and well-behaved relationships with NDVI as those for the densely vegetated
414 regions and thus a hybrid approach is developed for these types of land cover as described in the
415 next sub-section.

416 2.2.3 Hybrid approach over urban/ built-up and transitional regions

417 The derivation of surface reflectances for aerosol retrievals over the urban/ built-up
418 regions and cropland/transitional zones is highly challenging for a number of reasons. First, as
419 shown in Fig. 9, the relationship between the visible and 2.1 μm surface reflectances over these
420 types of land surfaces exhibit more complex behavior and are not in line with those for naturally

421 vegetated areas. Second, although their surface reflectances are not as bright, they are much
422 more susceptible to seasonal changes of vegetation growing and dying phases as well as the
423 effects of surface BRDF. Third, surface inhomogeneity is often a problem, particularly over large
424 cities where vegetation resides close to buildings, resulting in high variability of surface
425 brightness throughout the landscape. To address these issues, we developed a hybrid approach
426 for determining surface reflectance by combining the Deep Blue surface database with the
427 angular shapes of surface BRDF derived using AERONET measurements.

428 To derive these BRDF angular shapes, collocated satellite/AERONET data sets were
429 compiled using eight years of MODIS data (2003-2010) and more than ten years of SeaWiFS
430 data (1998-2010) acquired within a distance of 0.1° radius from the AERONET sites over
431 transitional and urban/ built-up regions. The satellite estimated surface reflectances were then
432 computed at 0.412, 0.47, and 0.65 μm for MODIS and 0.412, 0.49, and 0.67 μm for SeaWiFS
433 using aerosol information from the AERONET measurements by applying the same atmospheric
434 correction procedures mentioned in section 2.2.2. Once again, only pixels with AERONET AOT
435 < 0.5 were included for such studies in order to minimize the uncertainty of aerosol contribution
436 in determining surface reflectance. Also, to account for the effect of vegetation changes, the
437 resulting surface reflectances were divided into 3 different groups according to their NDVI
438 values: NDVI <= 0.19; 0.19 < NDVI <= 0.24; NDVI > 0.24. Regression lines were then
439 computed as a function of scattering angle using a 2^{nd} order polynomial fit for each NDVI group
440 and each season to obtain the shapes of surface BRDF. One example of these procedures for
441 Banizoumbou (13°N, 2°E) in the Sahel is shown in Figures 14 and 15 for 0.412 and 0.470 μm,
442 respectively.

443 It is apparent in these figures that the surface greenness at this location has a strong
444 seasonal cycle, with more dense vegetation land cover (i.e., higher NDVI) in fall (September -
445 November) and more dry land surfaces (i.e., lower NDVI) in spring (March - May). However,
446 during the transitional time periods such as summer, the vegetation grows rapidly over a short
447 period of time due to the arrival of rainfall in the region, leading to a large temporal gradient in
448 the NDVI and thus the surface reflectance values. As shown in Figure 14 and 15, the resulting
449 angular shapes of surface reflectances are derived by applying polynomial fits through the data
450 points stratified by NDVI to characterize the surface properties based upon the state of
451 vegetation. Finally, we combine these derived angular shapes with surface reflectance values
452 from the Deep Blue surface database at 135° scattering angle described in section 2.2.1 to
453 compute surface reflectance for aerosol retrievals over these urban/built-up and transitional
454 zones. This hybrid method has been applied to the regions of orange color indicated in Fig. 5 for
455 both SeaWiFS and MODIS data.

456 In order to better track the performances of the three different approaches mentioned
457 above, a new SDS named “Deep_Blue_Algorithm_Flag_Land” was added into the MODIS C6
458 DB products, as shown in Table 1. One of three different values (i.e., Deep Blue surface
459 database, vegetated land surfaces, or mixed) will be reported in this SDS to indicate which one of
460 these three methods was used in the actual retrieval for the given cell.

461 2.3 Aerosol model selection

462 The general scheme for selecting aerosol models used in C6 retrievals is similar to C5
463 [Hsu et al., 2004, 2006]. However, additional use of MODIS infrared channels has been
464 employed in C6 to identify the presence of extremely absorbing mineral dust. According to the

findings of Hansell et al. [2007], the use of the brightness temperature difference between 8.6 and 11 μm (BTD8-11) is robust in detecting strongly-absorbing dust such as the silicates (e.g., quartz, clays, etc.), which have strong Restrahlen bands and often absorb infrared radiation more at 8.6 μm than at 11 μm. Since these types of mineral dust also exhibit strong absorption of visible light, in particular for blue wavelengths, non-identification of such aerosols will lead to the underestimation of AOT in the Deep Blue retrieval algorithm.

One example of such a case is shown in Figure 16 for July 9, 2007. On this day, extensive dust plumes were seen in the MODIS/Aqua RGB image (Fig. 16a) around the Bodele Depression and the region surrounding it (14ºN-20ºN, 10ºE-20ºE) as well as over the western part of the Sahara (15ºN-30ºN, 15ºW-5ºE, as indicated by the circle). In Fig. 16b, the heavy dust loading near the Bodele Depression was reflected in the MODIS C5 AOT map; however, the dust plumes over the western part of the Sahara were not captured well by the C5 algorithm. In order to address this issue, we added a new heavy dust flag in the C6 algorithm, which is based upon the D* value developed by Hansell et al. [2007]; D* is defined as

$$D^* = exp\{[(BTD11\text{-}12) - A] / [(BTD8\text{-}11) - B)]\}$$

where parameters A and B are the thermal offsets for BTD11-12 and BTD8-11, respectively. In the C6 algorithm, the values of -0.05 and 10.0 are used for A and B for the D* calculation. When the condition $D^* > 1.1$ is detected, the retrieval algorithm will go directly to the three wavelength (0.412, 0.47, and 0.65 μm) approach and bypass the two wavelength (0.412 and 0.47 μm) method. As described in Hsu et al. [2004], an initial step of using the two wavelength method is performed in the Deep Blue algorithm to determine if there is sufficient aerosol loading in the atmosphere for retrieving aerosols with the 0.65 μm channel over bright surfaces, where the

surface contribution dominates the TOA reflectance under low to moderate aerosol loading conditions. If the criteria on aerosol loadings are met for a given pixel, the algorithm will conduct a three-wavelength retrieval, which is less susceptible to the presence of strongly blue light absorbing aerosols compared to the two-wavelength retrieval.

As displayed in Fig. 16(c), the dust plumes in the problematic areas over the western part of the Sahara are well correlated with elevated values in D*, although other regions with high dust loadings that are apparent in the MODIS RGB image do not stand out in the D* map. This is likely due to the combination of the different sensitivity of D* to different types of mineral dust as well as the effects of underlying surface emissivity on D*. By using this new heavy dust flag, the C6 Deep Blue algorithm is able to produce better results for retrieved AOT (Fig. 16 (d)) for strong blue light absorbing dust as compared to the C5 AOT shown in Fig. 16(b). It is noted that only the AOT retrievals with a quality assurance flag (QA) of 2 or 3 were shown in the C5 and C6 AOT maps in Fig. 16. Therefore, the gaps in the retrieved AOT near the middle of MODIS swath caused by the use of the scattering angles filter in the QA determination scheme (as described below) were only seen in the C5 map and not in the C6 one. Other differences in the retrieved AOT values between C5 and C6 primarily result from the changes made in the C6 surface reflectance determination scheme.

2.4 Data quality flag and uncertainty estimate

As shown in Table 1, the values of the QA flag and estimated uncertainty assigned to each pixel are now added in C6 as part of the Deep Blue SDS product suite. Similar to the convention used in C5, the quality flags in C6 also have 4 different levels (i.e., QA=0, 1, 2, 3 with 0 for no retrieval, 1 as the worst quality retrieval, and 3 for the best data quality). However,

509 there are several major changes in the QA flag selection procedures. For example, in C5 the QA
510 flag was limited to 1 for scattering angles greater than 168º due to increasing surface reflectance
511 at high scattering angles (i.e. BRDF hot spots) over many types of surfaces. This constraint is
512 lifted in C6 due to improved statistics obtained by using eight years of MODIS data over the
513 high scattering angle range used in the analysis for constructing the Deep Blue surface database,
514 and the use of a hybrid approach to better characterize the angular shapes in C6.

515 As a result of the improvements made in surface reflectance determination, the selections
516 of QA flag in C6 only simply rely on the number (N) of retrieved AOT pixels at 0.550 μm (i.e.,
517 minimum N = 40 and 60 out of 100 for QA = 2 and 3, respectively) and their standard deviation
518 (σ) within 10 x 10 pixels (i.e., maximum σ = 0.18 and 0.15 for QA = 2 and 3, respectively), and
519 no longer depend on surface types as used in C5. Overall, the criteria for achieving higher QA is
520 more relaxed in C6, leading to a higher number of retrieved pixels reaching QA=2 or 3 as
521 compared to C5. The estimated uncertainty of the retrieval for each cell is also reported in C6
522 based upon the corresponding viewing geometry and air mass factor. A detailed description of
523 the estimated uncertainty calculation is included in Sayer et al. [2013]. It is important to note that
524 since pixels with QA=1 for the DB AOT product could potentially still have cloud contamination
525 issues, a new SDS named "Deep_Blue_Aerosol_Optical_Depth_550_Land_Best_Estimate" was
526 created in C6 to report good quality pixels with AQ=2 or 3; we highly recommend that this SDS
527 be used by the general user community.

528 3. Results and Comparisons between C5 and C6 products

529 We have used the C6 DB algorithm described above to process reflectance data from the
530 Aqua MODIS instrument for July 17-18, 2004, to compare with data from the C5 algorithm.

Figure 17 illustrates the advantage of the enhanced Deep Blue retrieval. As seen in the RGB images (left column), smoke from large fires burning in Alaska and Northwestern Canada traveled across the North American continent, impacting the Great Lakes region. The C5 Deep Blue aerosol retrieval, shown in the middle column, is limited to bright underlying surfaces. The resulting retrieval, therefore, covers very little of the mostly vegetated Great Lakes region. The enhanced Deep Blue algorithm extends the capability of Deep Blue to the vegetated, or darker, surface types. The right column of Figure 17 shows nearly complete AOT data, excluding only cloudy and water surfaces. The areas of high AOT in the enhanced Deep Blue images (right column, values in orange, red) appear to correspond well to the smoke plumes visible in the RGB images; The July 17 image captures the heavy smoke west of the Great Lakes, while the July 18 image follows the plume eastward ahead of a cloud front.

We have also compared the monthly mean AOT for July and September 2012 using the MODIS Aqua data with QA=2 or 3 from C5 (left panel) with C6 (right panel) in Figure 18. This figure clearly shows that the spatial coverage of retrieved AOT has increased substantially from C5 to C6 due to the improved surface reflectance determination scheme used in C6. Aerosol information retrieved over extensive vegetation-covered areas are now included in Deep Blue C6 data. For example, during July 2012, there were elevated AOT values observed in northern Alberta and Saskatchewan, Canada. This was associated with biomass burning smoke generated from wildfires ignited by lightning under extreme dry heat and high wind conditions. At the same time, smoke plumes produced by forest fires in Russia traveled thousands of miles, leading to the elevated AOT observed over a large area at high latitudes in the Northern Hemisphere. The AOT maps for September also reveal high biomass burning activity in South America with

553 high AOT values covering a large portion of the continent; this information could not have been
554 obtained from the C5 Deep Blue data.

555 The spatial coverage of retrieval over urban/built-up and transitional zones is also much
556 improved from C5 to C6. Since the previous C5 algorithm excluded any pixels with significant
557 vegetation cover, and there are many large cities that have green vegetation inside the city zones,
558 retrievals over such sites were scarce. By performing retrievals over both dark and bright
559 surfaces inside the city limits, enough information was acquired to provide adequate quality for
560 performing aerosol retrievals over these urban regions.

561 The coverage over desert and semi-desert regions is roughly the same between C5 and
562 C6, as expected. However, due to the improved surface reflectance database and aerosol model
563 selection scheme in C6, there are also significant differences in the monthly averaged AOT over
564 these regions, such as higher AOT values in C6 than C5 over the western part of the Sahara and
565 the southern part of Arabian Peninsula and lower values over Australia.

566 In order to study the effects of changes made in the C6 QA selection scheme,
567 comparisons of the fractions of aerosol retrievals (defined as ratio of number of retrievals to total
568 number of observations) with 'all QA' and QA=3 between C5 and C6 for the month of July 2012
569 are depicted in Figure 19. As expected, for 'all QA' the retrieval fractions are in general the same
570 between C5 and C6 for desert regions, but significantly improved from C5 to C6 over vegetated
571 and urban/built-up regions. For QA=3, the retrieval fractions are substantially improved from C5
572 to C6 almost everywhere, even over dry regions such the Sahara/Sahel and the Arabian
573 Peninsula, as a result of the QA selection changes in C6 described in section 2.4.

574

4. Preliminary comparisons with AERONET AOT measurements

Extensive validation of the new SeaWIFS and MODIS Deep Blue aerosol datasets has been performed by Sayer et al. [2012a, 2013]. Here, some brief results are shown for MODIS (Aqua) to illustrate the significant improvements of C6 over C5. This analysis uses data from 10 long-term AERONET sites at which both C5 and C6 provide retrievals (Agoufou, Banizoumbou, Beijing, Boulder, Fresno, Hamim, Kanpur, Mongu, Solar Village, Tinga Tingana); AERONET and MODIS data are spatiotemporally matched by averaging MODIS retrievals with QA=3 within 25 km of each AERONET site, and AERONET data (interpolated spectrally to 550 nm) within 30 minutes of the MODIS overpass [Sayer et al., 2013].

Scatter density plots of the matched data are shown in Figure 20. Although a good level of agreement is found for both C5 and C6 data, performance is notably better for C6, with the number of extreme outliers reduced and a tighter clustering of points around the 1:1 line. Specifically, there are improvements in the correlation with AERONET (0.86 in C5, 0.93 in C6), median bias (-0.015 in C5, -0.008 in C6), root mean square error (0.22 in C5, 0.14 in C6), and proportion of retrievals agreeing within 0.05+20% of the AERONET AOT (62% in C5, 79% in C6). Additionally, the data volume for these 10 sites has nearly doubled (6,335 matchups for C5, 11,234 for C6). These results show that the C6 data represents a large improvement on C5 both in terms of extent of coverage of QA=3 retrievals, as well as the level of uncertainty of those retrievals. As C5 did not provide retrievals over vegetated surfaces, it is not possible to provide a comparative benchmark of this type in a more global sense; however, the analyses of Sayer et al. [2012a, 2013] show a similar high quality of performance of the DB algorithm over vegetated areas.

5. Conclusions

A goal of the MODIS periodic reprocessing strategy is to provide self-consistent (i.e. no algorithmic discontinuities through the record) geophysical datasets, leveraging developments in understanding made between these reprocessings. In order to achieve this goal of continual improvement, the Deep Blue aerosol retrieval algorithm has undergone many modifications in C6 based on the latest knowledge of aerosol remote sensing. As compared to C5, the most significant changes include (1) improved cloud screening scheme to maximize the aerosol retrieval frequency with minimal cloud contamination; (2) the use of a newly-developed NDVI-dependent MODIS surface reflectance database to replace the previous static surface look-up tables; (3) a better dust aerosol model selection scheme using visible and thermal infrared bands simultaneously; and (4) revised quality flag selection procedures. In particular, the dynamic surface reflectance determination permits expansion of the spatial coverage of the Deep Blue aerosol products from only the bright-reflecting surfaces (such as deserts, semi-deserts, and non-vegetated urban areas) to all snow-free land surfaces, including vegetated areas. Consequently, the aerosol retrievals have been significantly improved in C6 over regions with mixed vegetated and non-vegetated surfaces such as urban areas, providing useful information for the study of air quality over large cities.

Besides the substantial increase in spatial coverage as the results of enhanced surface reflectance determination and cloud screening schemes, the overall performance of the retrieved aerosol properties for MODIS C6 has also been improved as compared to C5. Based upon the preliminary validation results of the enhanced Deep Blue algorithm using measurements from selected ten long-term AERONET sites, the estimated error for the new C6 Deep Blue products is better than 0.05+20%, with 79% of best quality AOT (QA=3) data that fall within this range,

620 as compared to the 62% in C5. The number of the AOT retrieval with QA=3 has also nearly
621 doubled from C5 to C6.

622 Finally, in order to achieve consistency in continuous long-term aerosol time series from
623 the EOS-era sensors such as SeaWiFS and MODIS to VIIRS onboard the Suomi NPP satellite,
624 the new enhanced Deep Blue algorithm, which has been used in generating MODIS C6 as well
625 as SeaWiFS version 3 aerosol products, will also be applied to VIIRS to extend the consistent
626 long-term satellite aerosol data record for climate studies.

627

628

629 **Acknowledgements**

630 This work was supported by the NASA EOS program, managed by Hal Maring. The authors
631 gratefully acknowledge the MODIS Characterization Support Team for their extensive efforts in
632 maintaining the high radiometric quality of MODIS level 1 data. We would also like to express
633 our gratitude to several AERONET PIs in establishing and maintaining the long-term stations
634 used in this investigation.

635 References

636 Breitkreuz, H., M. Schroedter-Homscheidt, T. Holzer-Popp, and S. Dech (2009), Short-Range
637 Direct and Diffuse Irradiance Forecasts for Solar Energy Applications Based on Aerosol
638 Chemical Transport and Numerical Weather Modeling. J. Appl. Meteor. Climatol., 48,
639 1766–1779, doi:10.1175/2009JAMC2090.1.

640 Dave, J. V. (1972), Development of programs for computing characteristics of ultraviolet
641 radiation, technical report, Vector Case, IBM Corp., Fed. Syst. Div., Gaithersburg, MD.

642 Deuzé, J. L., et al. (2001), Remote sensing of aerosols over land surfaces from POLDER-
643 ADEOS-1 polarized measurements, J. Geophys. Res., 106(D5), 4913–4926, doi:10.1029/
644 2000JD900364.

645 Franz, B. A., E. J. Kwiatkowska, G. Meister, and C. McClain (2008), Moderate Resolution
646 Imaging Spectroradiometer on Terra: limitations for ocean color applications, J. Appl.
647 Rem. Sens., vol. 2, 023525.

648 Kwiatkowska, E. J., B. A. Franz, G. Meister, C. McClain, and X. Xiong (2008), Cross-
649 calibration of ocean-color bands from Moderate Resolution Imaging Spectroradiometer on
650 Terra platform, Appl. Opt., vol. 47, pp. 6796-6810.

651 Friedl, M.A., D. K. McIver, J. C. F. Hodges, X. Y. Zhang, D. Muchoney, A. H. Strahler, C. E.
652 Woodcock, S. Gopal, A. Schneider, A. Cooper, A. Baccini, F. Gao, C. Schaaf (2002),
653 Global land cover mapping from MODIS: algorithms and early results, Remote Sensing of
654 Environment, 83, 287-302.

655 Gao, B.-C., P. Yang, W. Han, R.-R. Li, W. J. Wiscombe (2002), An algorithm using visible and
656 1.38-μm channels to retrieve cirrus cloud reflectances from aircraft and satellite data, IEEE
657 Trans. Geosci. Remote Sens., 40, 1659-1668.

658 Hall, D. K., G. A. Riggs, and V. V. Salomonson (1995), Development of methods for mapping
659 global snow cover using Moderate Resolution Imaging Spectroradiometer (MODIS) data,
660 Remote Sensing of Environment, 54, 127– 140.

661 Hansell, R. A., S. C. Ou, K. N. Liou, J. K. Roskovensky, S. C. Tsay, C. Hsu, and Q. Ji (2007),
662 Simultaneous detection/separation of mineral dust and cirrus clouds using MODIS thermal
663 infrared window data, Geophys. Res. Lett., 34, L11808, doi:10.1029/2007GL029388.

664 Hasekamp, O. P., and J. Landgraf (2007), Retrieval of aerosol properties over land surfaces:
665 capabilities of multi-viewingangle intensity and polarization measurements, Appl. Opt.,
666 46(16), 3332-3344, doi:10.1364/AO.46.003332.
667 Holben, B. N., et al. (1998), AERONET- a federated instrument network and data archive for
668 aerosol characterization, Remote Sens. Environ., 66, 1-16.
669 Hsu, N. C., S. C. Tsay, M. D. King, and J. R. Herman (2004), Aerosol properties over bright-
670 reflecting source regions, IEEE Trans. Geosci. Remote Sens., 42, 557-569.
671 Hsu, N. C., S. C. Tsay, M. D. King, and J. R. Herman (2006), Deep Blue Retrievals of Asian
672 Aerosol Properties During ACE-Asia, IEEE Trans. Geosci. Remote Sens, 44, 3180-3195.
673 Huang, J., N. C. Hsu, S.-C. Tsay, M.-J. Jeong, B. N. Holben, T. A. Berkoff, and E. J. Welton
674 (2011), Susceptibility of aerosol optical thickness retrievals to cirrus contamination during
675 the BASE-ASIA campaign, J. Geophys. Res., 116, D08214, doi:10.1029/2010JD014910.
676 Jeong, M.-J., Z. Li, D.A. Chu, and S.-C. Tsay (2005), Quality and compatibility analyses of
677 global aerosol products derived from the advanced very high resolution radiometer and
678 moderate resolution imaging spectroradiometer, J. Geophys. Res., 110, D10S09,
679 doi:10.1029/ 2004JD004648.
680 Jeong, M.-J., N. C. Hsu, E. J. Kwiatkowska, B. A. Franz, G. Meister (2011), Impacts of cross-
681 platform vicarious calibration on the Deep Blue aerosol retrievals for Moderate Resolution
682 Imaging Spectroradiometer aboard Terra, IEEE Trans. Geosci. Remote Sens, doi: 10.1109/
683 TGRS.2011.2153205.
684 Kaufman, Y. J., A. Wald, L. A. Remer, B. C. Gao, R. R. Li, and L. Flynn (1997), The MODIS
685 2.1-μm channel - Correlation with visible reflectance for use in remote sensing of aerosol,
686 IEEE. Trans. Geosci. Remote Sens., 35(5), 1286-1298.
687 Knobelspiesse, K., B. Cairns, M. Mishchenko, J. Chowdhary, K. Tsigaridis, B. van
688 Diedenhoven, W. Martin, M. Ottaviani, and M. Alexandrov (2012), Analysis of fine-mode
689 aerosol retrieval capabilities by different passive remote sensing instrument designs. Opt.
690 Express, 20, 21457-21484, doi:10.1364/OE.20.021457.
691 Levy, R. C., L. A. Remer, S. Mattoo, E. F. Vermote, and Y. J. Kaufman (2007), Second-
692 generation operational algorithm: Retrieval of aerosol properties over land from inversion
693 of Moder-ate Resolution Imaging Spectroradiometer spectral reflectance, J. Geophys. Res.,
694 112, D13211, doi:10.1029/2006JD007811.

695 Lyapustin, A., Y. Wang, I. Laszlo, R. Kahn, S. Korkin, L. Remer, R. Levy, and J. S. Reid (2011),
696 Multiangle implementation of atmospheric correction (MAIAC): 2. Aerosol algorithm, J.
697 Geophys. Res., 116, D03211, doi:10.1029/2010JD014986.
698 Martonchik, J. V., R. A. Kahn, and D. J. Diner (2009), Retrieval of aerosol properties over land
699 using MISR observations, in Aerosol Remote Sensing Over Land, edited by A.
700 Kokhanovsky and G. deLeeuw, pp. 267–293, Springer, Berlin.
701 Meister, G., E. J. Kwiatkowska, B. A. Franz, F. S. Patt, G. C. Feldman, and C. R. McClain
702 (2005), Moderate-Resolution Imaging Spectroradiometer ocean color polarization
703 correction, Appl. Opt., vol. 44, pp. 5524-5535.
704 Meskhidze, N., W. L. Chameides, and A. Nenes (2005), Dust and pollution: A recipe for
705 enhanced ocean fertilization?, J. Geophys. Res., 110, D03301, doi:10.1029/2004JD005082.
706 Mi, W., Z. Li, X. Xia, B. Holben, R. Levy, F. Zhao, H. Chen, and M. Cribb (2007), Evaluation of
707 the Moderate Resolution Imaging Spectroradiometer aerosol products at two Aerosol
708 Robotic Network stations in China, J. Geophys. Res., 112, D22S08, doi:10.1029/
709 2007JD008474.
710 Mishchenko, M. I., A. A. Lacis, and L. D. Travis (1994), Errors introduced by the neglect of
711 polarization in radiance calculations for Rayleigh scattering atmospheres, J. Quant.
712 Spectrosc. Radiat. Transfer, vol. 51, pp. 491-510.
713 Omar, A. H., et al. (2009), The CALIPSO automated aerosol classification and lidar ratio
714 selection algorithm, J. Atmos. Oceanic Technol., 26, 1994–2014, doi:10.1175/
715 2009JTECHA1231.1.
716 Pope, C. A. III (2000), Epidemiology of fine particulate air pollution and human health: biologic
717 mechanisms and who's at risk?, Environ. Health Perspect., 108, 713-723.
718 Remer, L. A., et al. (2008), Global aerosol climatology from the MODIS satellite sensors, J.
719 Geophys. Res., 113, D14S07, doi:10.1029/2007JD009661.
720 Sayer, A. M., N. C. Hsu, C. Bettenhausen, M.-J. Jeong, B. N. Holben, and J. Zhang (2012a),
721 Global and regional evaluation of over-land spectral aerosol optical depth retrievals from
722 SeaWiFS, Atmos. Meas. Tech., 5, 1761-1778, doi:10.5194/amt-5-1761-2012.
723 Sayer, A. M., G. E. Thomas, R. G. Grainger, E. Carboni, C. Poulsen, and R. Siddans (2012b),
724 Use of MODIS-derived surface reflectance data in the ORAC-AATSR aerosol retrieval

algorithm: Impact of differences between sensor spectral response functions Rem. Sens. Environ, 116, 177-188, doi:10.1016/j.rse.2011.02.029.

Sayer, A. M., N. C. Hsu, C. Bettenhausen, B. N. Holben (2013), Providing uncertainty estimates for MODIS Collection 6 Deep Blue aerosol data through validation with AERONET, J. Geophys. Res., submitted.

731 Table 1. List of SDS names for MODIS collection 6 Deep Blue aerosol products

Name	Dimensions	Description
Deep_Blue_Angstrom_Exponent_Land	[Cell_Along_Swath, Cell_Across_Swath]	Angstrom exponent over land.
Deep_Blue_Aerosol_Optical_Depth_550_Land	[Cell_Along_Swath, Cell_Across_Swath]	Aerosol optical depth at 550nm over land.
Deep_Blue_Aerosol_Optical_Depth_550_Land_Best_Estimate	[Cell_Along_Swath, Cell_Across_Swath]	Aerosol optical depth at 550nm over land filtered by quality (QA=2,3 only).
Deep_Blue_Aerosol_Optical_Depth_550_Land_STD	[Cell_Along_Swath, Cell_Across_Swath]	Standard deviation of individual pixel-level aerosol optical depth at 550nm per cell.
Deep_Blue_Algorithm_Flag_Land	[Cell_Along_Swath, Cell_Across_Swath]	Flag indicating the path taken through the algorithm.
Deep_Blue_Aerosol_Optical_Depth_550_Land_QA_Flag	[Cell_Along_Swath, Cell_Across_Swath]	Quality assurance flag for aerosol optical depth at 550nm.
Deep_Blue_Aerosol_Optical_Depth_550_Land_Estimated_Uncertainty	[Cell_Along_Swath, Cell_Across_Swath]	Estimated uncertainty in aerosol optical depth at 550nm.
Deep_Blue_Cloud_Fraction_Land	[Cell_Along_Swath, Cell_Across_Swath]	Fraction of pixels per cell where retrieval was not attempted.
Deep_Blue_Number_Pixels_Used_550_Land	[Cell_Along_Swath, Cell_Across_Swath]	Number of aerosol property retrievals performed per cell.
Deep_Blue_Spectral_Aerosol_Optical_Depth_Land	[Num_DeepBlue_Wavelengths, Cell_Along_Swath, Cell_Across_Swath]	Retrieved aerosol optical depth over land at 412 nm, 470 nm, and 650 nm.
Deep_Blue_Spectral_Single_Scattering_Albedo_Land	[Num_DeepBlue_Wavelengths, Cell_Along_Swath, Cell_Across_Swath]	Single scattering albedo over land at 412 nm, 470 nm, and 650 nm.
Deep_Blue_Spectral_Surface_Reflectance_Land	[Num_DeepBlue_Wavelengths, Cell_Along_Swath, Cell_Across_Swath]	Surface reflectance used in aerosol retrieval over land for 412 nm, 470 nm, and 650 nm.
Deep_Blue_Spectral_TOA_Reflectance_Land	[Num_DeepBlue_Wavelengths, Cell_Along_Swath, Cell_Across_Swath]	Top-of-atmosphere reflectance at 412 nm, 470 nm, and 650 nm.

732

733 Cell_Along_Swath = number of cells in the along-track direction.
734 Cell_Across_Swath = number of cells across the swath.
735 Num_DeepBlue_Wavelengths = number of bands reported by the Deep Blue products, currently has
736 a value of 3 (412nm, 470nm, and 650nm).

737

738 Table 2. Surface reflectance coefficients over naturally vegetated regions for MODIS 0.47 and
739 0.65 μm

	R0.65/R2.1 (a, b, c)	R0.47/R0.65 (d, e)
DJF/MAM	0.5526, 0.4801, 0.0038	-0.3305, 0.4830
JJA	0.4413, 0.4606, 0.0045	-0.5841, 0.4961
SON	1.1749, 0.3560, 0.0067	0.0048, 0.4429

740 Note. These values inside each cell are corresponding to a, b, c, d, and e in equations 2 and 3.
741

742

743 Table 3. Surface reflectance coefficients over cropland for MODIS 0.47 and 0.65 μm

	$NDVI_{SWIR} < 0.35$		$NDVI_{SWIR} >= 0.35$	
	R0.65/R2.1 (a, b, c)	R0.47/R0.65 (d, e)	R0.65/R2.1 (a, b, c)	R0.47/R0.65 (d, e)
DJF/MAM	6.2828, 0.1658, 0.0	2.6884, 0.2751	-0.9766, 0.6213, 0.0	0.9126, 0.3982
JJA	5.2395, 0.2077, 0.0	0.2451, 0.5442	-0.1187 , 0.5036, 0.0	-0.0736, 0.5345
SON	-2.2642, 0.6781, 0.0	1.2493, 0.3576	-1.2799, 0.6161, 0.0	1.2724, 0.2039

744 Note. These values inside each cell are corresponding to a, b, c, d, and e in equations 2 and 3.
745

746

747 Table 4. Surface reflectance coefficients over vegetated regions for SeaWiFS 0.67 μm

	0.10< NDVI' <=0.20	0.20< NDVI' <=0.55	NDVI' >0.55
MAM	-1.5184, 0.9797, -1.2189	-1.0948, 0.8639, -0.6745	-0.7002, 0.6672, -0.9535
JJA	-1.5077, 0.9695, -0.8751	-1.0772, 0.8724, -0.9543	-0.6919, 0.6721, -1.1697
SON	-1.5244, 0.9743, -1.1274	-1.0676, 0.8650, -0.9757	-0.6497, 0.6204, -0.3580
DJF	-1.6123, 0.9736, -0.7547	-1.0597, 0.8491, -0.5760	-0.7054, 0.6767, -0.6852

748 Note. The three values inside each cell are corresponding to a, b, and c in equation 4.
749

750 Table 5. Surface reflectance coefficients over vegetated regions for SeaWiFS 0.49 μm

	0.10< NDVI' <=0.20	0.20< NDVI' <=0.55	NDVI' >0.55
MAM	-1.1617, 0.5278, 0.7483	-0.5822, 0.4222, 1.3564	-0.4264, 0.3903, 0.2547
JJA	-0.5839, 0.3888, 2.2656	-0.5500, 0.3699, 2.6355	-0.3990, 0.3881, -0.3469
SON	-0.9448, 0.4835, 0.9249	-0.5271, 0.3615, 1.9300	-0.3185, 0.3040, 0.3497
DJF	-1.3836, 0.4686, 3.2991	-0.6764, 0.4439, 1.4341	-0.4177, 0.4442, -1.2915

751 Note. The three values inside each cell are corresponding to d, e, and f in equation 5.
752
753

754

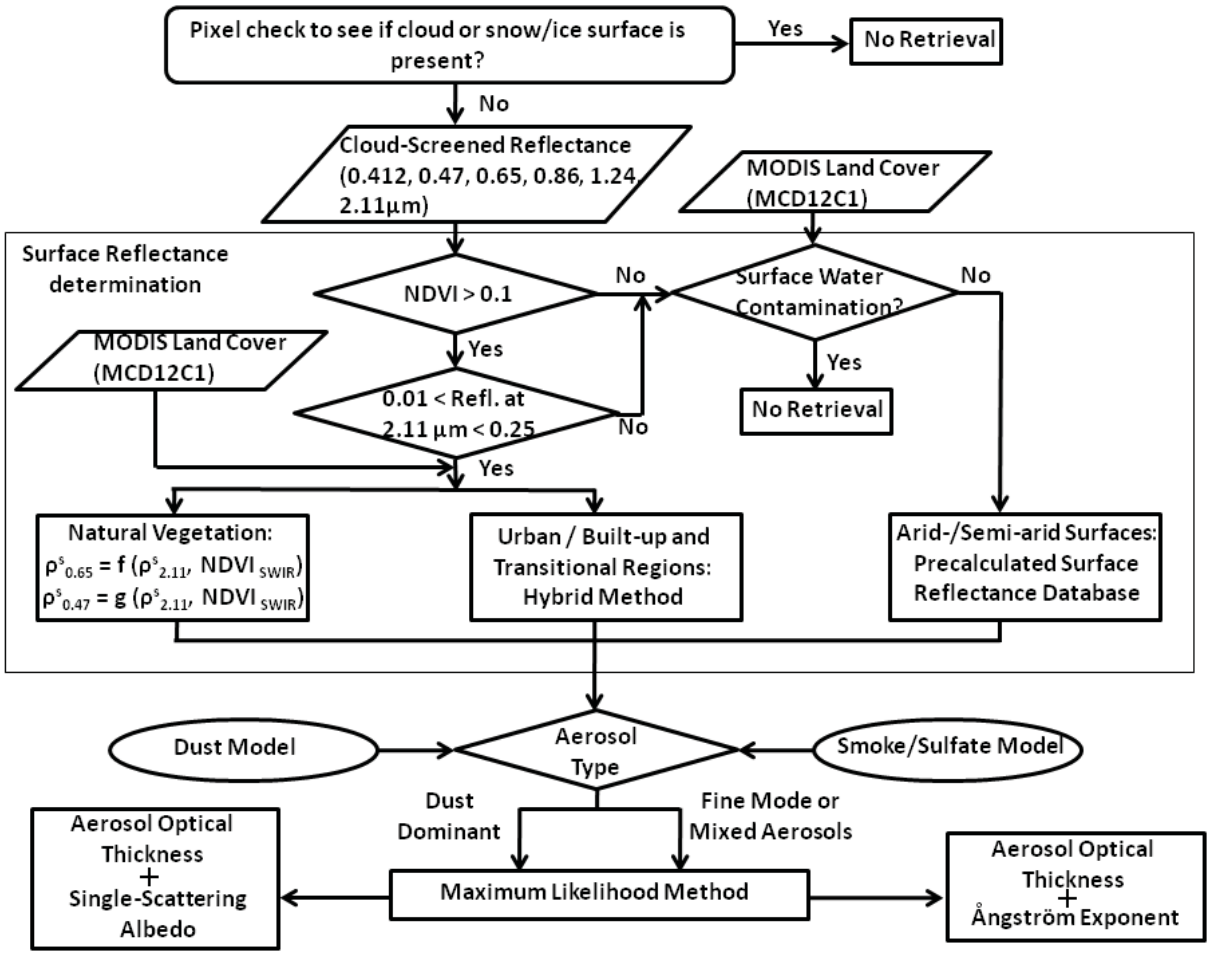

Figure 1. Flowchart of the enhanced MODIS Deep Blue algorithm

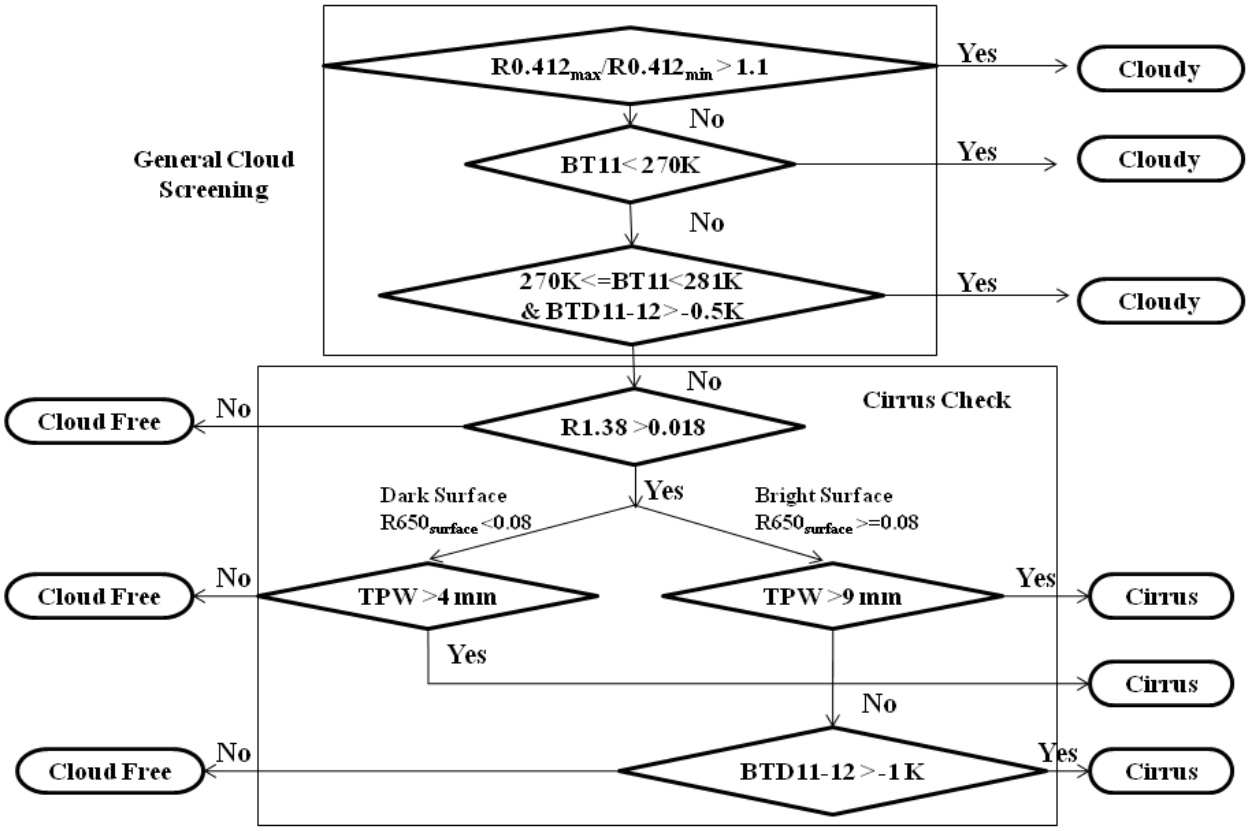

760

761 Figure 2. Flowchart of cloud screening used in MODIS C6 Deep Blue algorithm

762

763

764

765

766

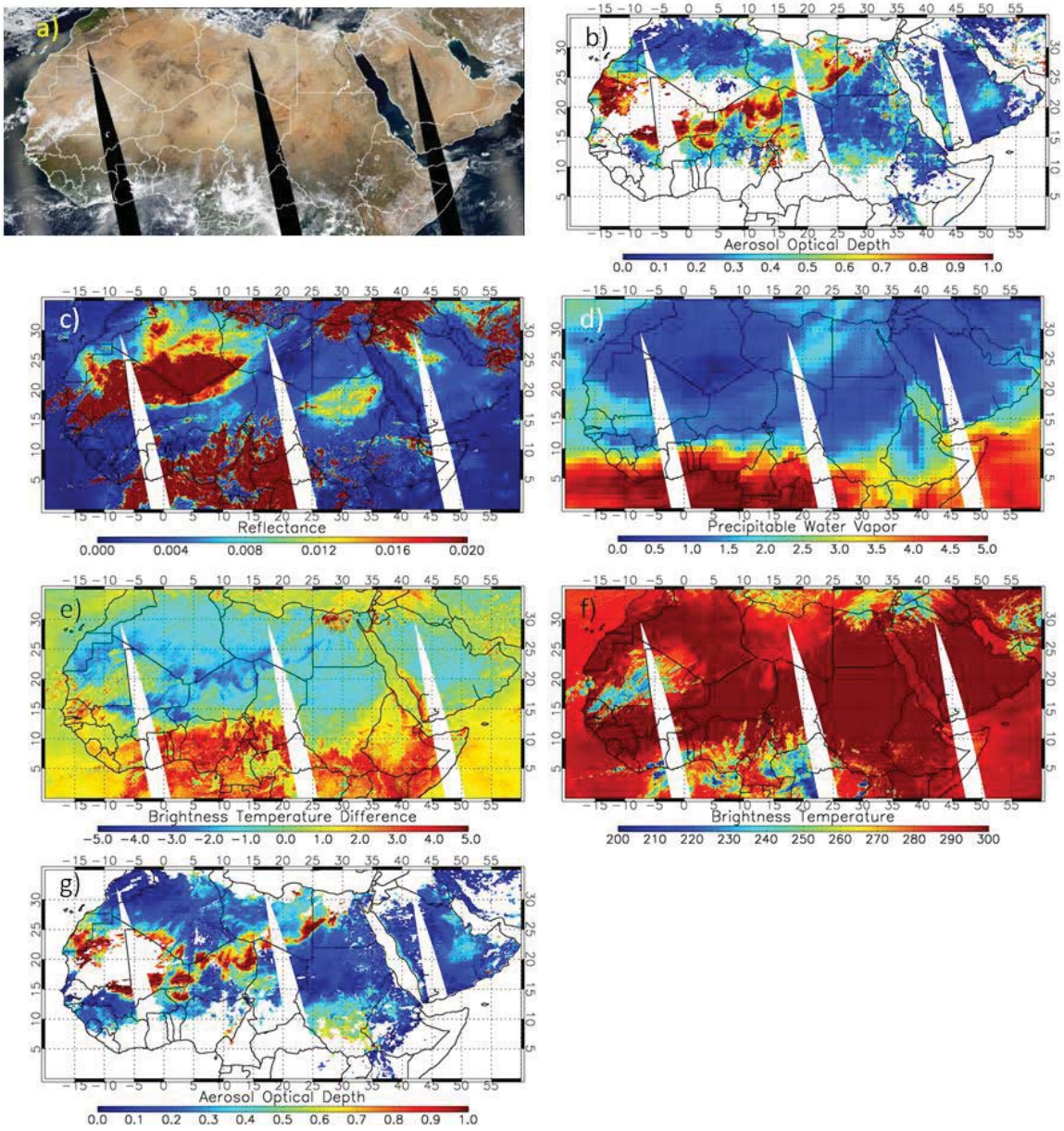

Figure 3. A Thin Cirrus Over-Screening Case over Sahara on March 7, 2006. The impacts of improved cirrus screening on the spatial coverage of AOT retrievals are seen when comparing the C5 AOT map in Fig. 3b with the C6 in Fig. 3g. The corresponding values of TOA reflectance at 1.38 μm, total precipitable water, brightness temperature difference (BTD11-12), brightness temperature (BT11) used for cirrus screening are depicted in Fig. 3c, 3d, 3e, and 3f, respectively. The MODIS RGB image is also included in Fig. 3a.

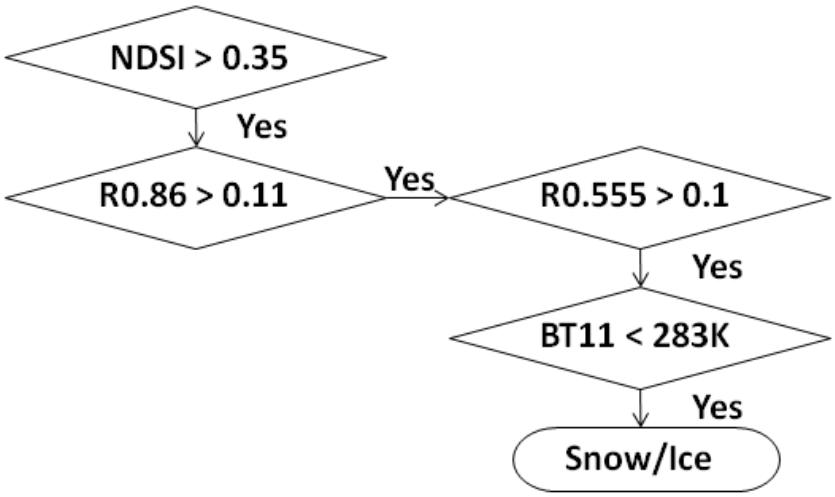

776

777 Figure 4. Flowchart of screening for snow/ice surfaces in MODIS C6

778

779

780

781

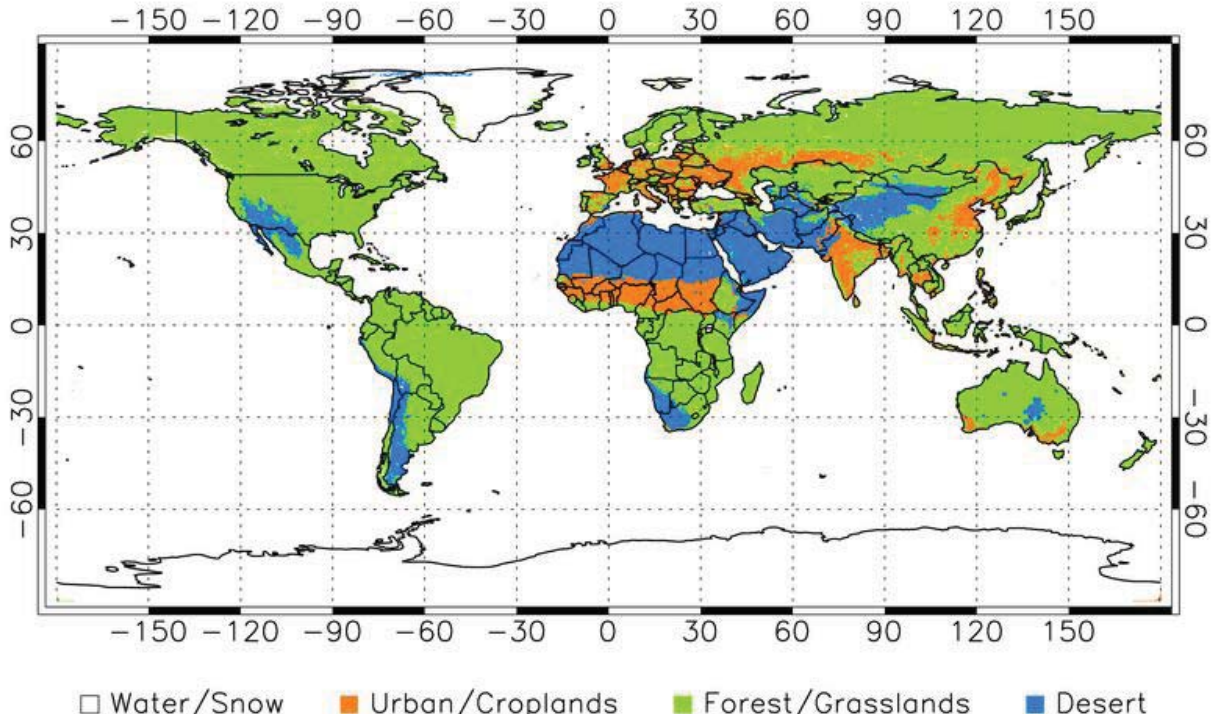

Figure 5. Geographic regions where the three surface reflectance schemes are used in the enhanced Deep Blue algorithm of (1) deserts and semi-deserts (blue color), (2) general vegetation (green color), and (3) urban/built-up and transitional zones (orange color). The regions with white colors are associated with either water or snow/ice surfaces and thus no over-land aerosol retrieval algorithm is applied over these regions.

796

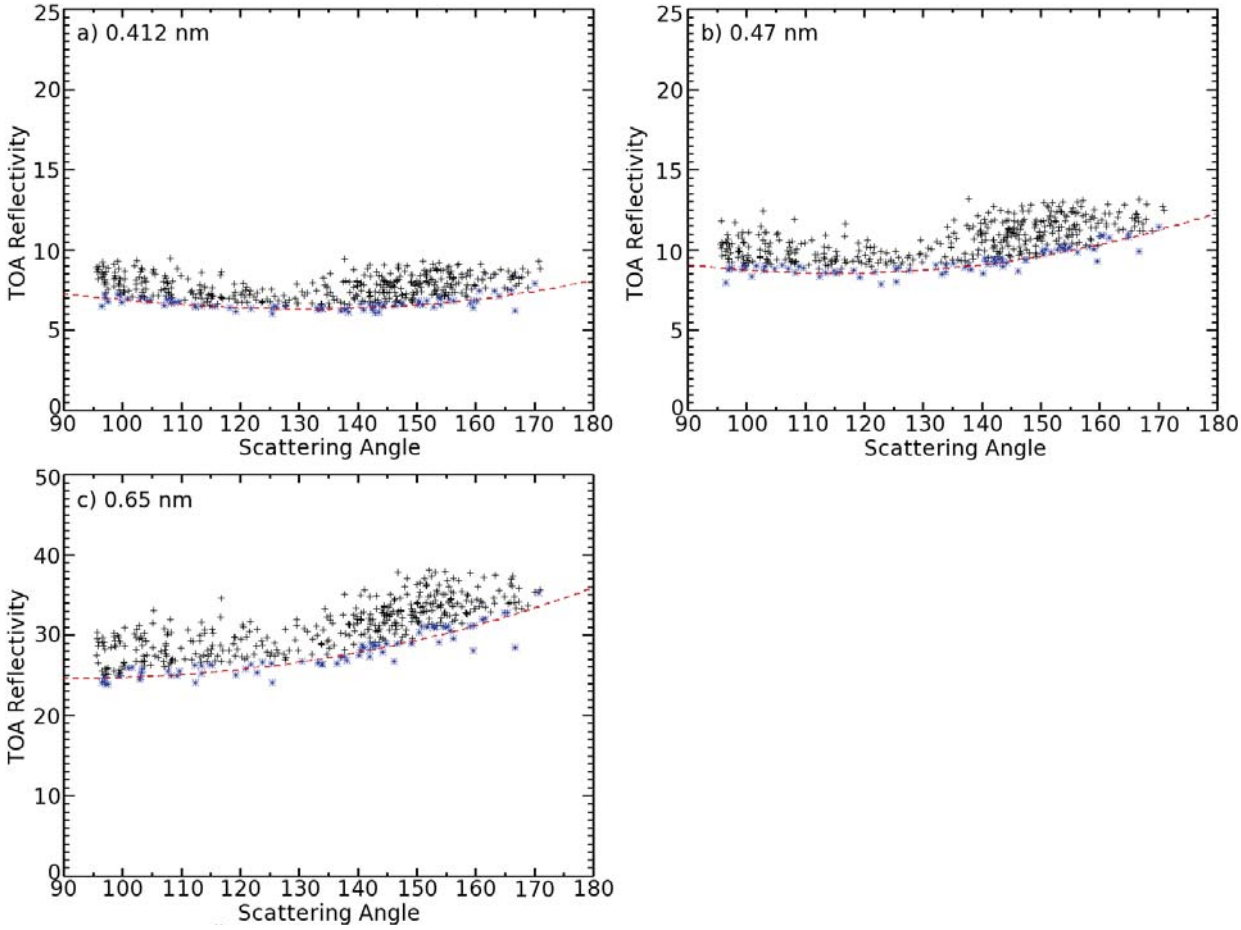

797

798 Figure 6. Example of constructing the Deep Blue surface database over Tinga Tingana,
799 Australia for the fall season as a function of scattering angle using MODIS reflectivity (%) at (a)
800 0.412, (b) 0.47, and (c) 0.65 μm. Blue symbols denote the lowest 15 percentile and the red curve
801 is the polynomial fit through the blue symbols.

802

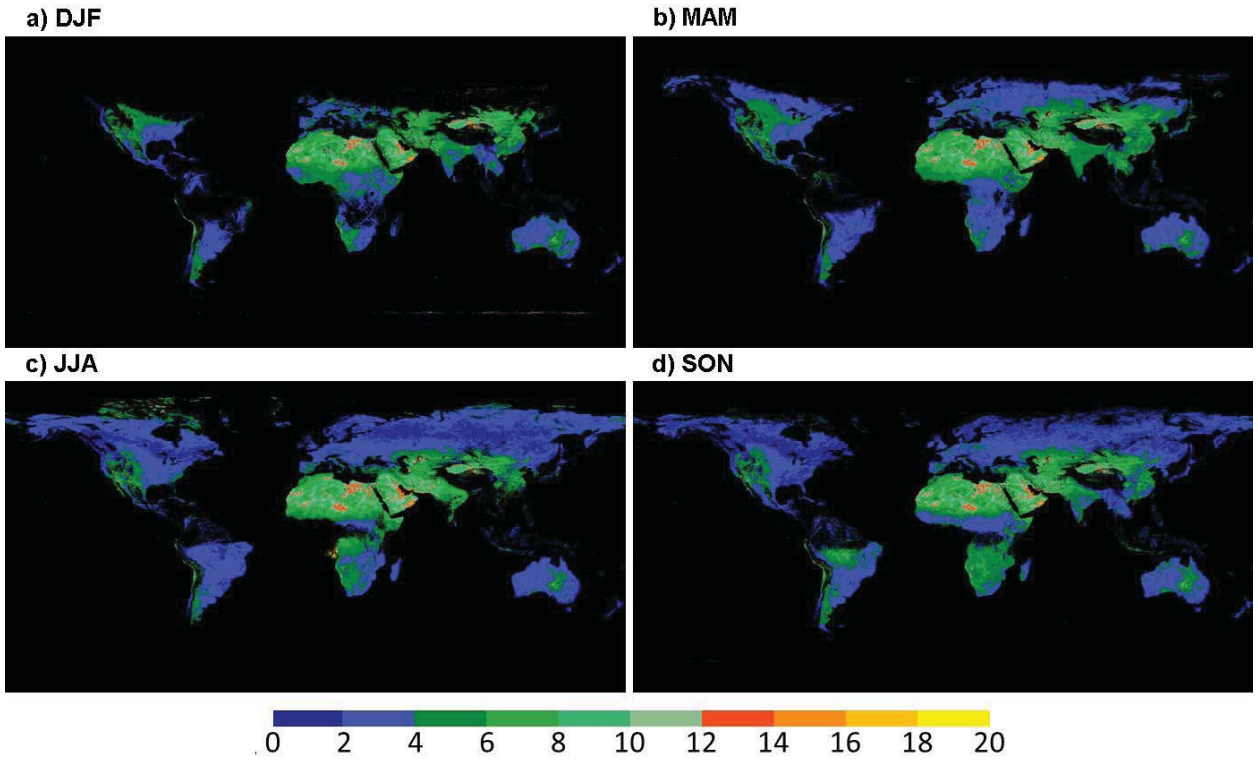

Figure 7. Seasonal maps of surface reflectance database at 0.412 μm used in the Deep Blue algorithm. The black color regions are associated with water body, snow/ice surface, or the frequent presences of clouds.

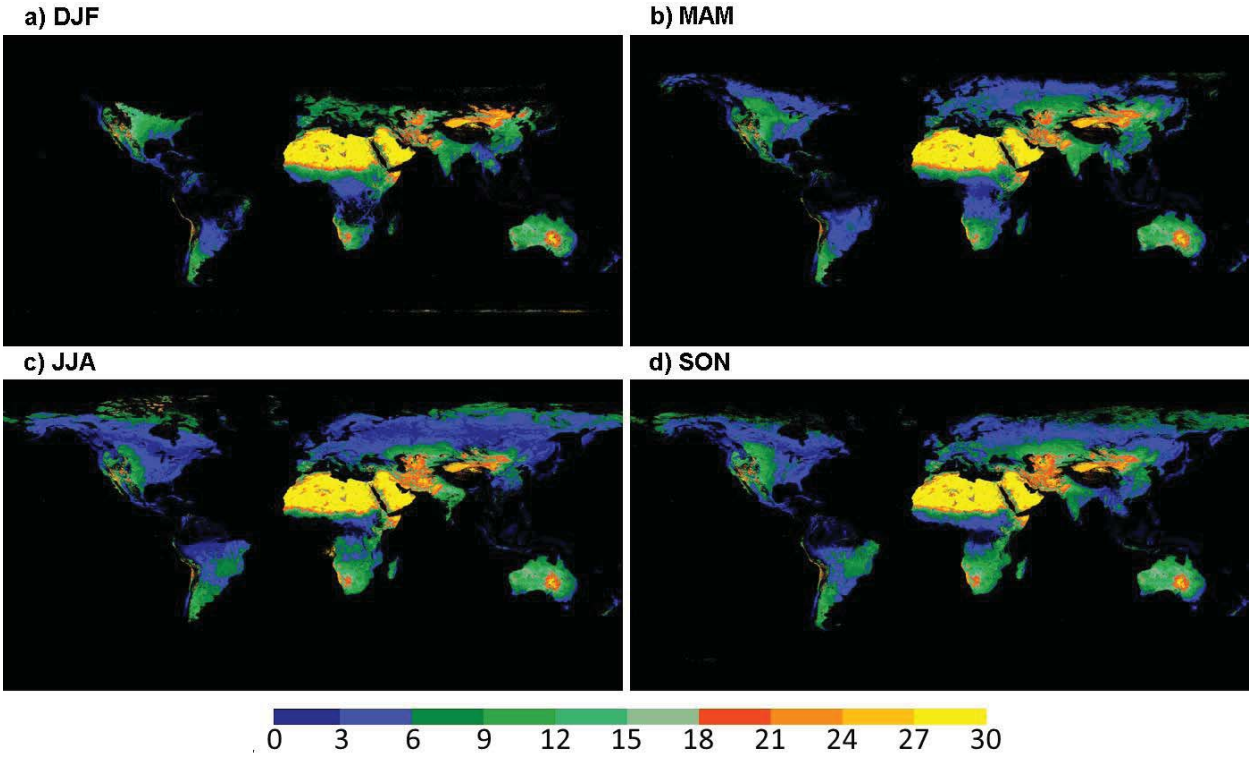

Figure 8. Same as Figure 7, except for 0.65 μm.

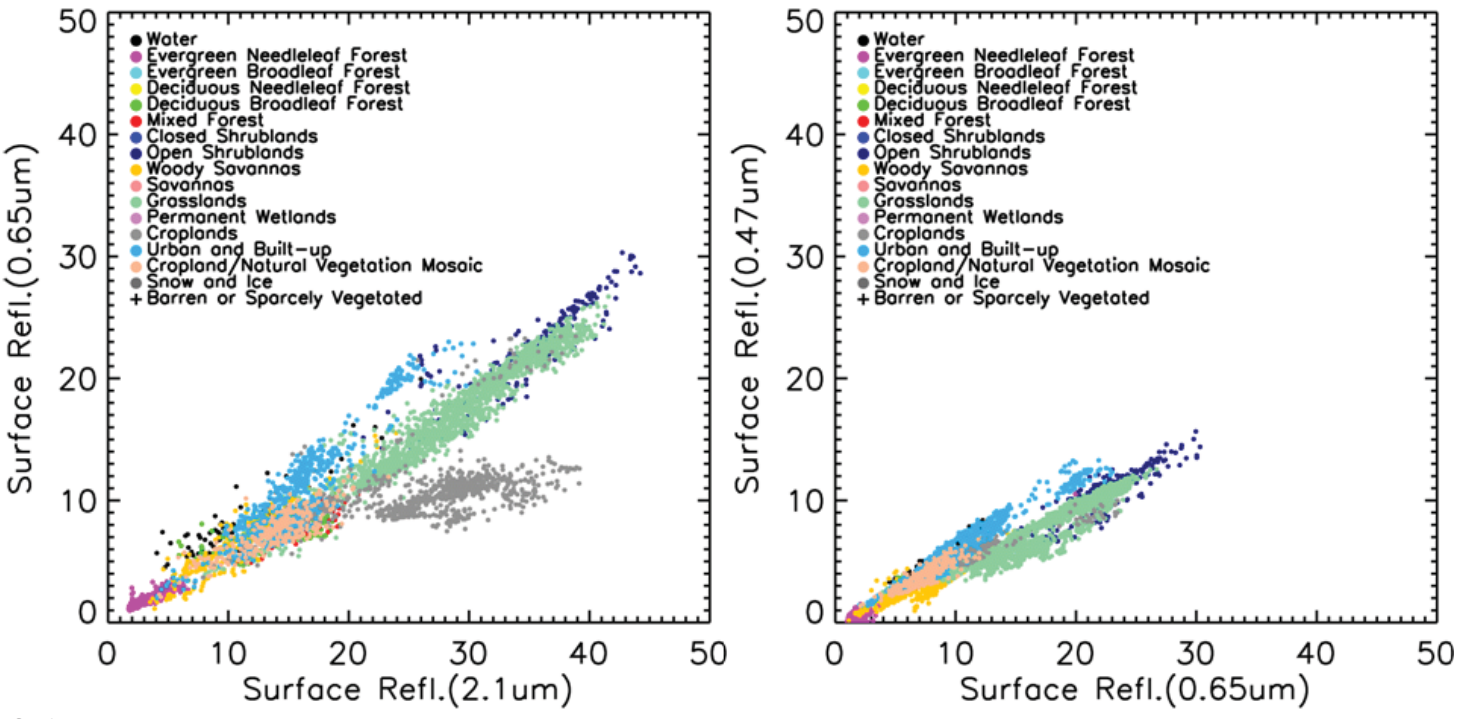

815 Figure 9. (Left) Spectral surface reflectance relationship (0.65 μm versus 2.11 μm) during
816 March-April-May, 2004, as a function of IGBP land cover from MODIS (MCD12C1). (Right)
817 The relationship in surface reflectance between 0.47 μm and 0.65 μm during March-April-May,
818 2004, as a function of IGBP land cover from MODIS (MCD12C1).

819

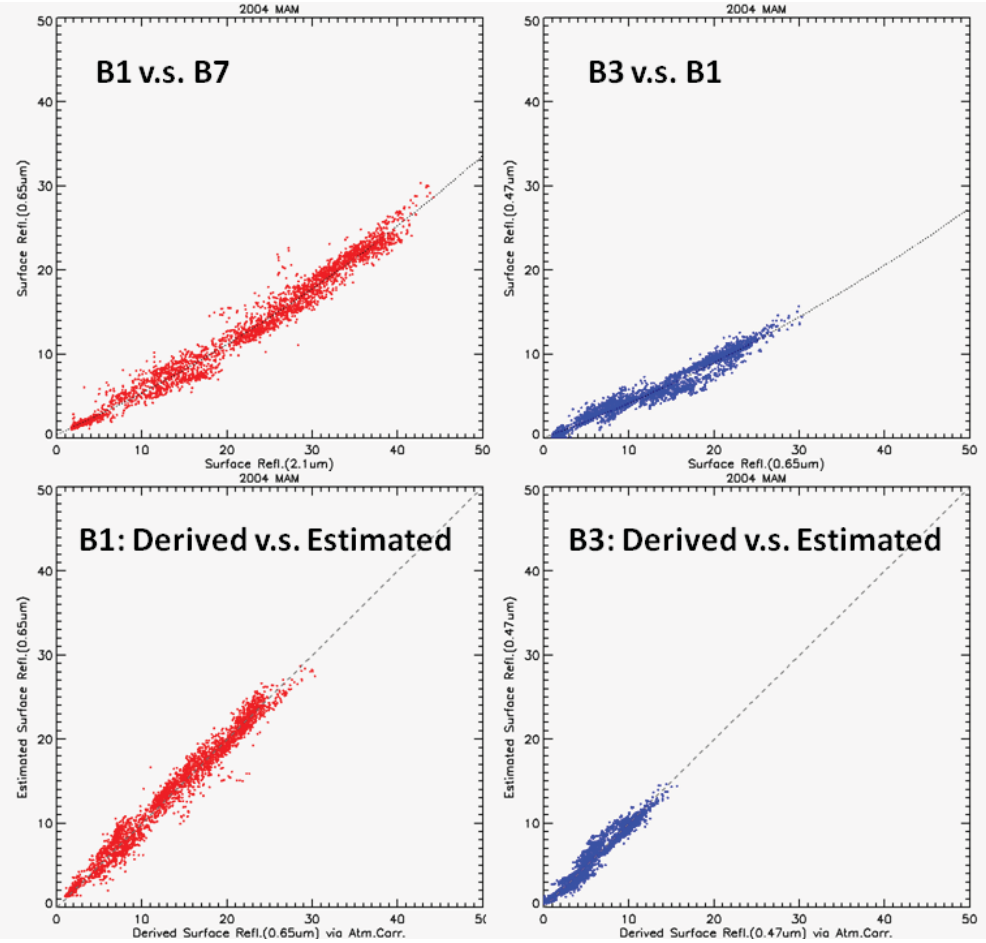

820

821 Figure 10. (Top) The spectral relationship of 0.65 vs. 2.1 μm (left) and 0.47 vs. 0.65 μm (right)
822 based upon benchmark surface reflectances for naturally vegetated regions during March-April-
823 May, 2004. The dotted line represents the 2nd order least square fit through the data points.
824 (Bottom) Comparisons between the derived benchmark and estimated surface reflectance for
825 0.65 μm (left) and 0.47 μm (right) channels. The dashed line denotes the one-to-one line.

826

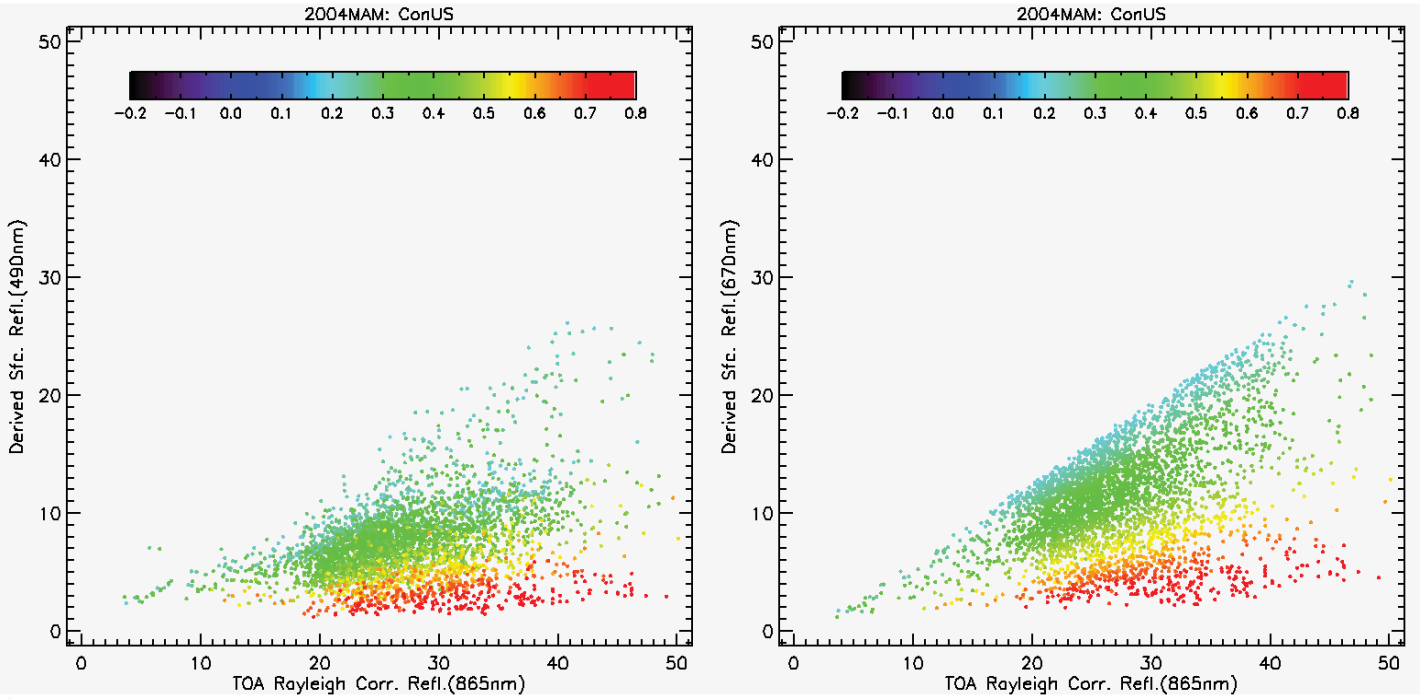

Figure 11. Derived surface reflectance using aerosol properties from AERONET measurements at 0.49 μm (left) and 0.67 μm (right) as function of Rayleigh-corrected reflectance at 0.865 μm at the top of the atmosphere and normalized difference vegetation index (NDVI) for the spring season. Color bar shows the values of NDVI for each point.

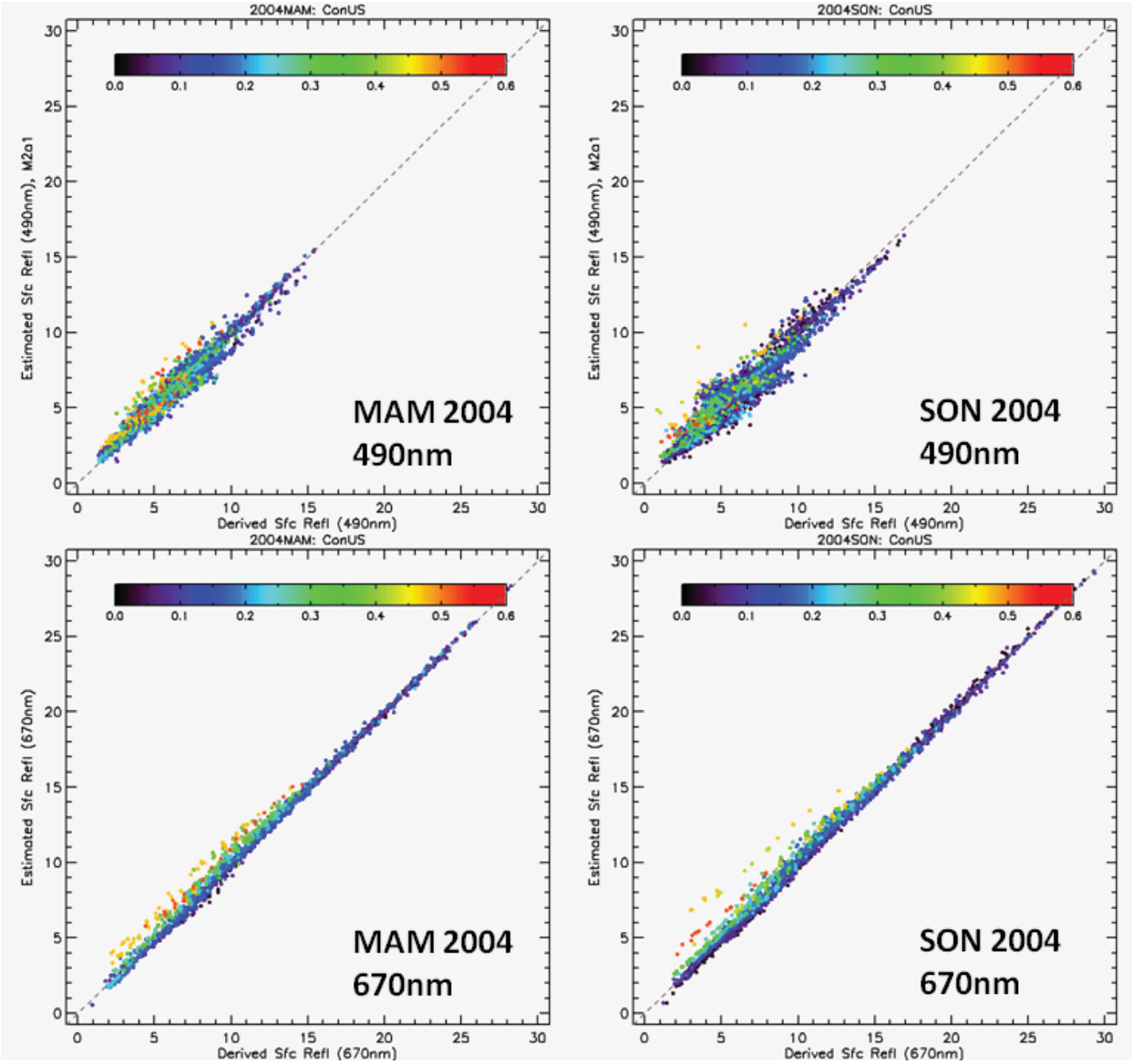

841

842 Figure 12. Comparisons of the estimated surface reflectance at 0.49 μm (top) and 0.67 μm
843 (bottom) with the derived benchmark surface reflectance at the same wavelength after
844 atmospheric corrections using AERONET AOT data for March-May (left) and September-
845 November (right). Color indicates AOT at 0.49 μm interpolated from AERONET AOTs using
846 Angstrom exponent.

847

848

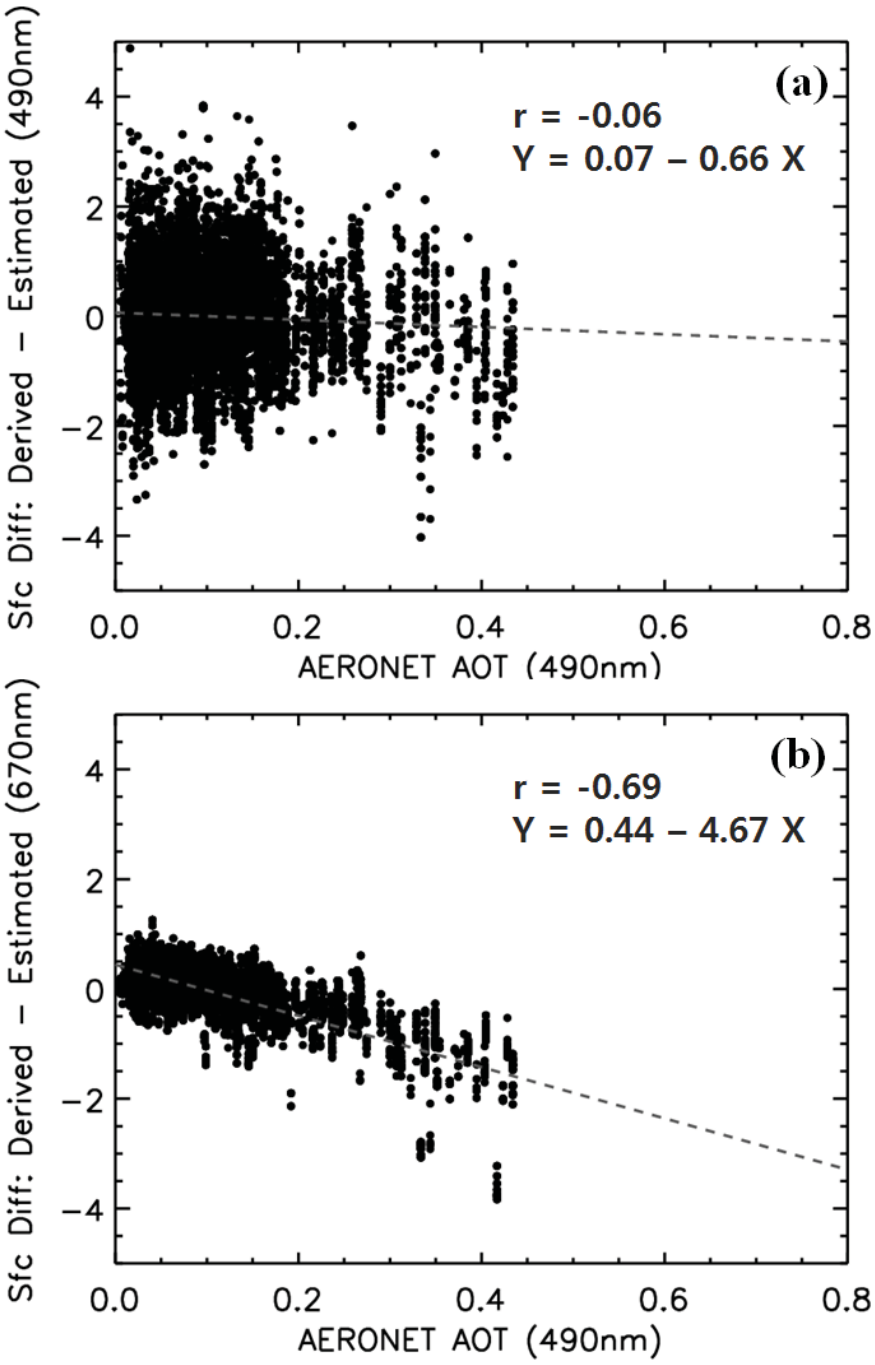

849

850 Figure 13. Differences between estimated and derived and surface reflectances (a) at 0.49 μm
851 and (b) at 0.67 μm as function of aerosol optical thickness (AOT) at 0.49 μm. Gray dashed lines
852 stand for linear fitting lines. Correlation coefficient (r) and the linear fitting equations are
853 presented in each plot.

854

855

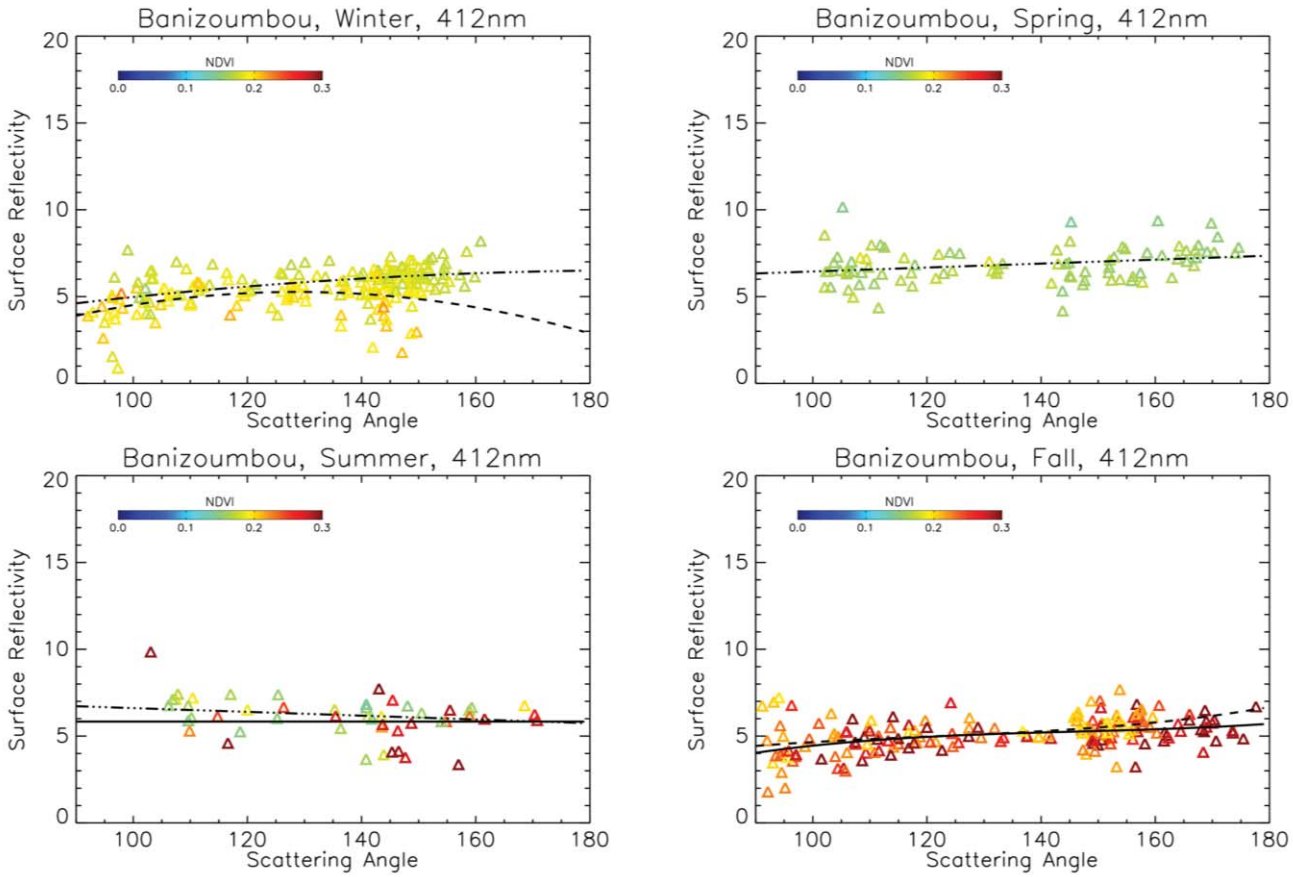

85

857 Figure 14. Atmospheric corrected surface reflectance at 0.412 μm for MODIS Aqua using
858 AERONET aerosol measurements over Banizoumbou. The color of the symbol is associated
859 with the NDVI value of the given pixel. The dash-dot, dashed, and solid lines represent the line
860 fit for each group of data with NDVI < 0.19, 0.19<= NDVI <2.4, and NDVI >=2.4, respectively.

861

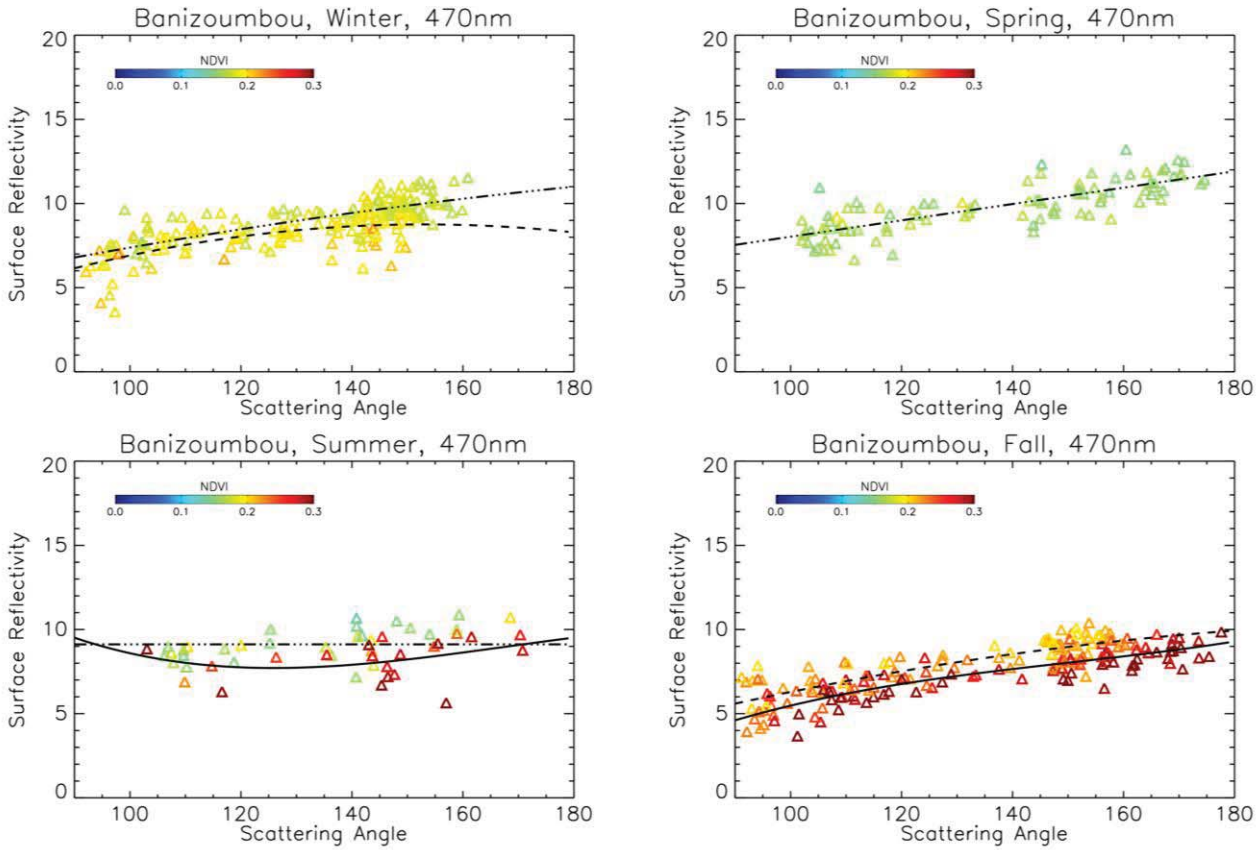

862

863 Figure 15. Same as Figure 14, except for 0.47 μm.

864

865

866

867

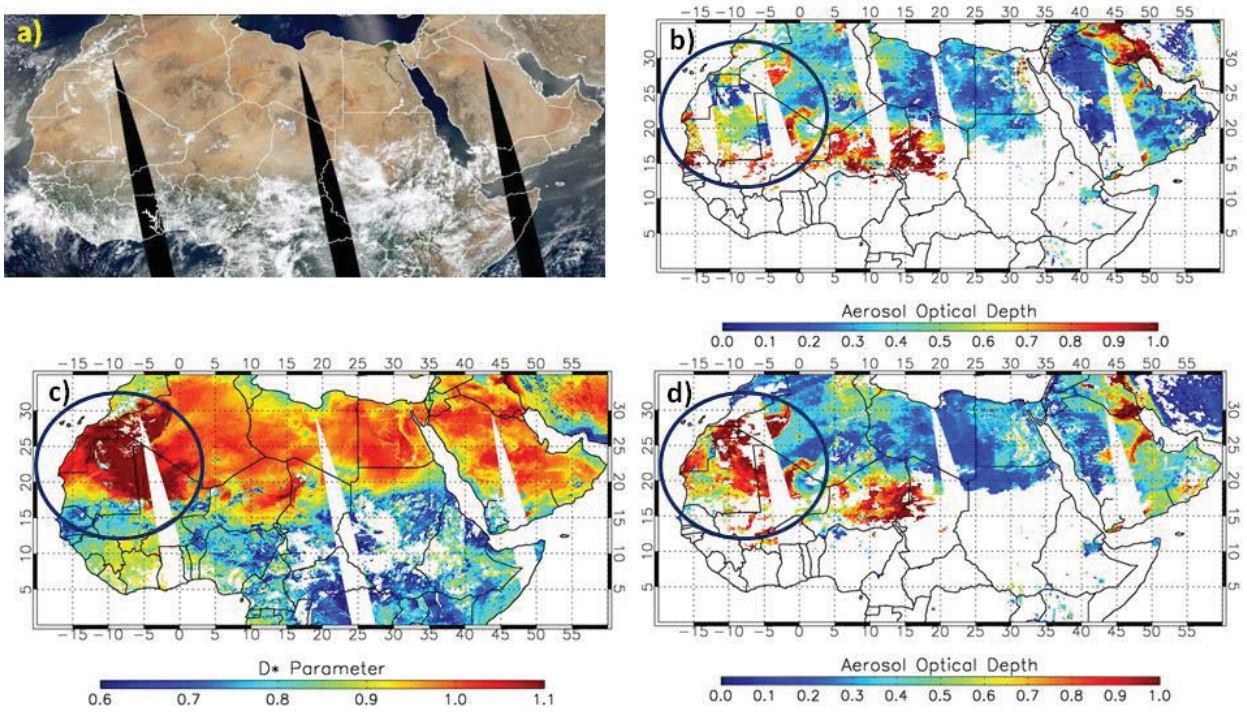

Figure 16. The effects of revised aerosol model selection scheme are shown by comparing the (b) MODIS Deep Blue C5 AOT with (d) MODIS Deep Blue C6 AOT for July 9, 2007. The circle indicates the area with most significant change in retrieved AOT as a result of this modification in C6 algorithm. The corresponding MODIS Aqua RGB image and D* values are also displayed in (a) and (c), respectively.

876

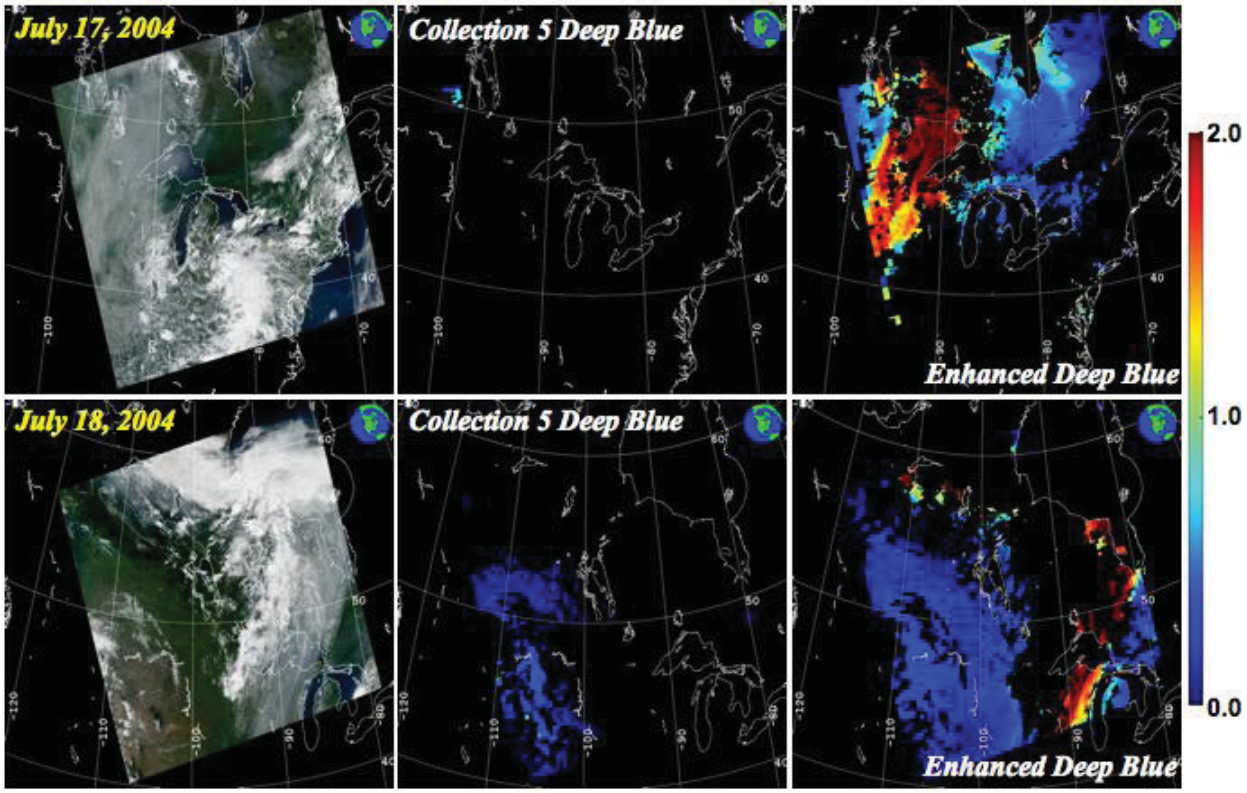

877

878 Figure 17. MODIS granule RGB images (left column) and *Deep Blue* AOT at 0.550 μm from
879 C5 (middle column) and C6 (enhanced *Deep Blue)* (right column) for smoke events over the
880 Great Lakes area on 17-18 July 2004.

881

882

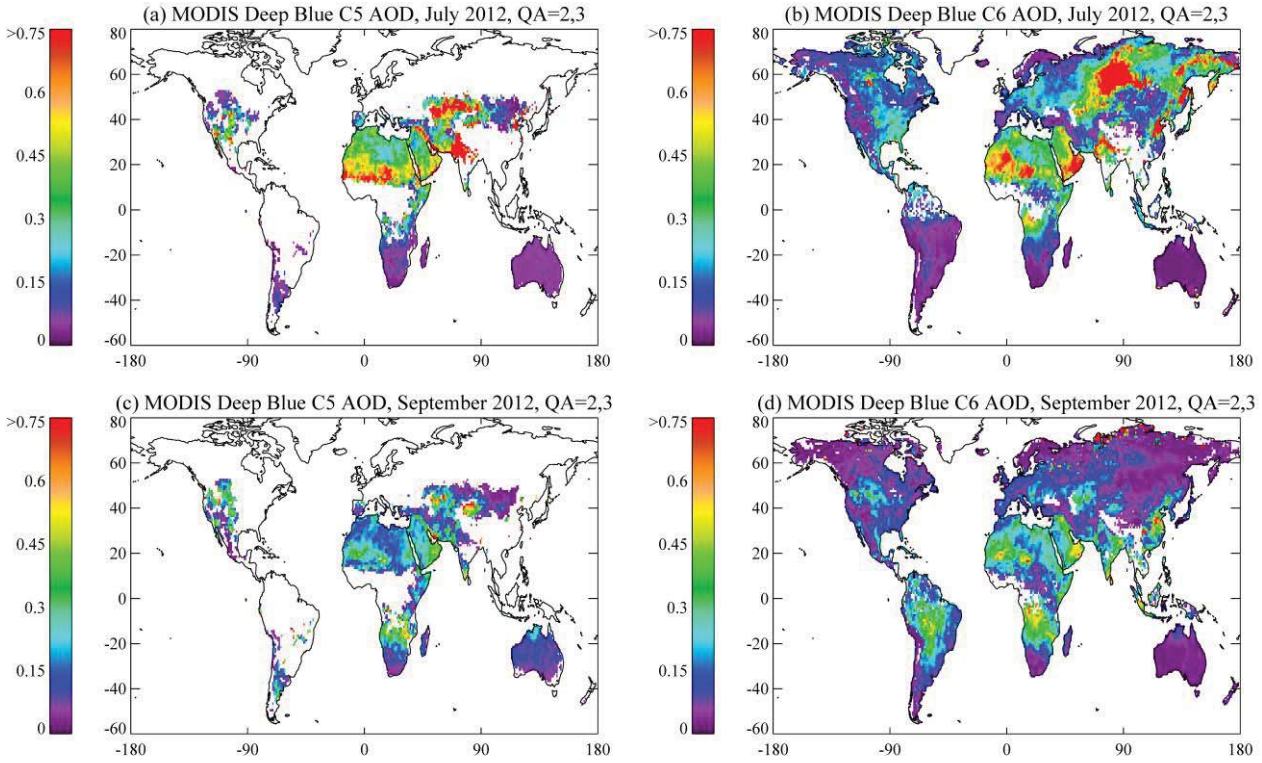

883

884 Figure 18. Comparisons of monthly averaged AOT at 0.55 μm between MODIS Aqua C5 and
885 C6 for July and September 2012. To alleviate the effect of sampling issues over the cloudy
886 regions in the monthly mean, only data with better QA (2 or 3) flag are included in the analysis.

887

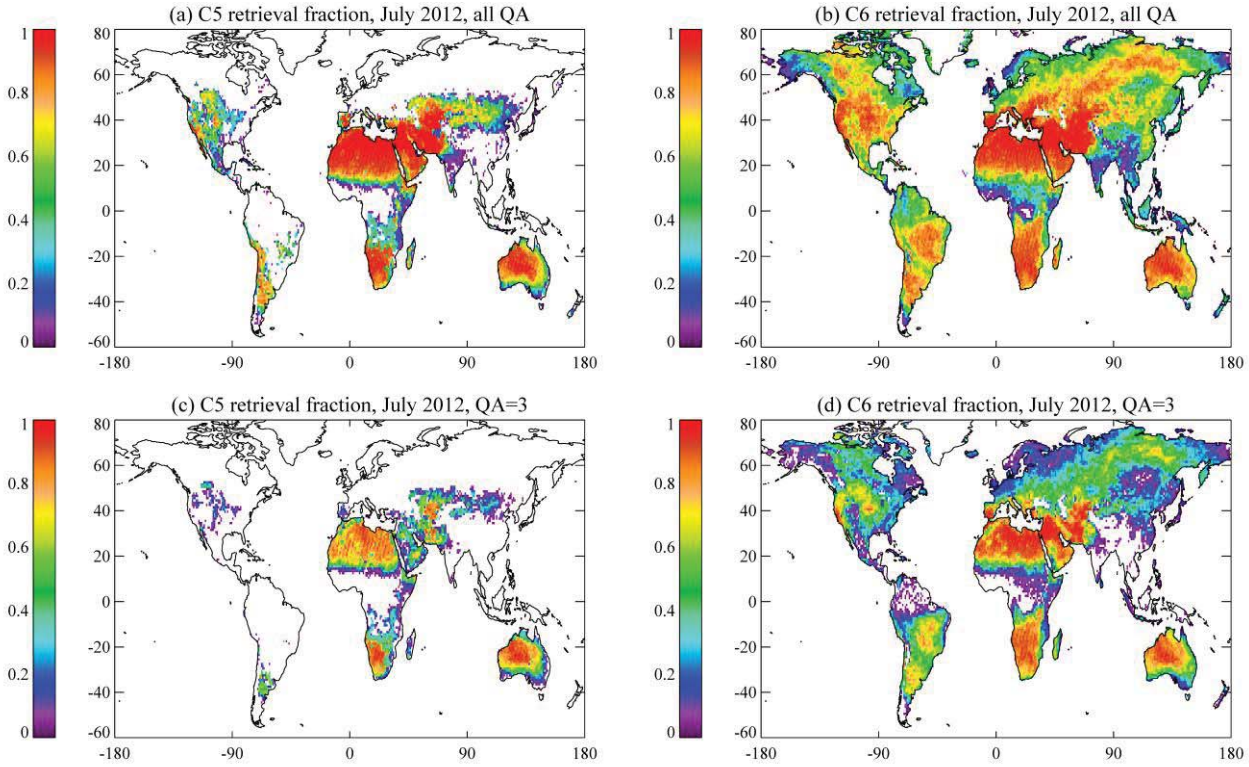

888

889 Figure 19. Comparisons of monthly averaged aerosol retrieval fractions between MODIS Aqua
890 C5 and C6 for July 2012 using data with all QA (top panel) and only QA=3 (bottom panel). The
891 white color represents regions with zero retrieval fraction.

892

893

894

895

896

897

898

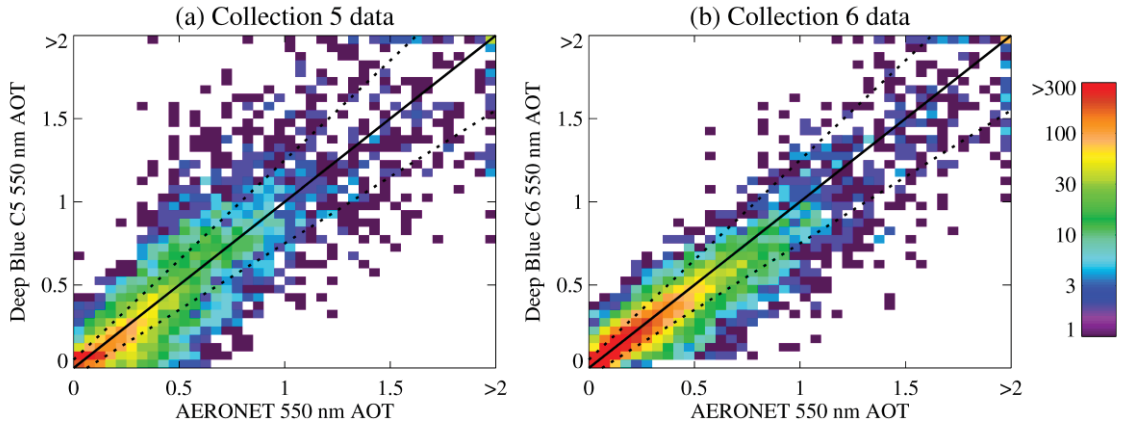

Figure 20. Scatter density plots of AERONET and MODIS Deep Blue AOT at 0.550 μm for (a) C5 and (b) C6, for 10 AERONET sites for which both Collections provide retrievals. The 1:1 line is shown in solid black; dotted lines indicate +/- 0.05+20% of the AERONET AOT.